Tampere University

Agata Szczodra

NOVEL OXYFLUORIDE BIOPHOTONIC GLASS-CERAMICS

ABSTRACT

Agata Szczodra: Novel oxyfluoride biophotonic glass-ceramics
Master's Thesis
Tampere University
Materials Science & Engineering
09.2019

Phosphate glasses are very interesting due to several properties, such as good thermal and mechanical stabilities, high transparency, low refractive index, low melting temperature and high gain density (Wa,03; Pr,08; Hr,13; Do,15). Most importantly, they exhibit higher solubility for RE ions, without clustering effect, compared to silica based glasses (Sh,05). Phosphate glasses are used for optical fibers and laser gain media applications (Mi,91; Su,15) and also for medical applications (Ne,08).

Second paragraph Oxyfluoride glasses combine advantages of fluoride and oxide glasses. Fluoride glasses have lower phonon energy but oxide glasses usually have much better chemical durability, thermal stability and mechanical strength than the fluoride glasses (Cu,16). As reported by (Cu,16) novel oxyfluoride phosphate glasses combining all these advantages are promising materials for bioactive and optical applications.

These glasses can be made with addition of rare-earth ions which are used for a wide range of applications such as telecommunications, light detection and ranging (LIDAR), solar panels, spectroscopy, and bio-imaging (De,98). In this thesis, Er^{3+} ions which show characteristic 1530 nm wavelength emission, have been used. Moreover, dopants like TiO_2, MgO and ZnO which affect thermal, structural and luminescence properties are often added to phosphate based glasses (Po,06; Cu,16).

To obtain better thermal and mechanical properties, glass-ceramic can be produced from glasses. This is done by using heat treatment process which allows one to achieve controlled crystallization of glass.

PeL properties of glass and glass-ceramic can be utilized in biophotonic PeL phosphate glasses. Such glasses can be used as bone implant, the mineralization of which can be tracked in-vivo. As reported by (Zh,16), PeL glass-ceramics can be produced using direct doping method in which PeL microparticles are added to the glass melt.

Finally, the feasibility of patterning microstructured 2D gratings at the surface of phosphate glass is investigated. The ability to carry out glass micropatterning in a cost- and time-effective fashion is crucial for producing devices and structures based on these materials for the mentioned applications. A potential use of the fabricated 2D gratings for monitoring phosphate glass degradation in wet environments through optical diffraction measurements is also introduced.

In the first and second chapter, the basic knowledge about glasses and materials and methods are described, respectively. In the results and discussion part, the impact of the glass composition on the glass is first investigated. Then, the effect of the heat treatment on produced glass-ceramic is described. Finally, the work on PeL oxyfluoride biophotonic glass-ceramics and patterning is presented. The impact of melting parameters and PeL microparticles concentration on luminescence properties is discussed. Conclusions and next steps are summarized in the last chapter.

Keywords: Glass, Glass-ceramic, Luminescence, Fluorine, Erbium, Etching

The originality of this thesis has been checked using the Turnitin OriginalityCheck service.

Acknowledgment

First and foremost, I would like to express the wholehearted gratitude to my mum. Thank you for the endless support and patience. You gave me love and understanding whenever I needed it. Secondly, my sincere appreciation goes to Abba Usman Saleh for being great inspiration and source of strength. You always mobilize me to reach my full potential. I wouldn't be where I'm if it wasn't for these two most important people in my life. Thank You for believing in me.

My gratitude also goes to my advisor Assoc. Prof. Laeticia Petit for guidance. Your help and support exceeded my expectations. I would also like to express my appreciation to Assoc. Prof. Carlos Angulo Barrios and Dr. Manuel Abuín for their supervision and assistance during my stay in Spain.

TABLE OF CONTENTS

1 Introduction

1.1 Glasses

Human started to produce silica based glasses thousands of years ago (Sh,05). Soda-lime glass is the most common manufactured glass today. It was also the first glass to be made. Its composition is around 70% SiO_2, 15% Na_2O, 9% CaO (mol%) and very small amounts of various other compounds (So,18). All that was needed to produce this glass was sand, commonly used as the source of SiO_2, combined and heated together with sodium carbonate Na_2CO_3 and limestone $CaCO_3$. Seashells were the sources of limestone and soda ash was obtained from dry lake bottoms in Egypt.

Nowadays, glasses applications are very wide ranging from art, chemical glassware, mirrors, windows, packaging, tableware, electric bulbs to more advanced applications in medical technology, optics, fiber optic communication, renewable energy, electronics and lasers (An,95; Be,14). Once described as 'the deepest and most interesting unsolved problem in solid state theory', glass nature is still a long standing mystery (An,95; Be,14).

1.1.1 Glass definition

Glass is a material which possesses a glass transition temperature at which it solidifies into an amorphous solid. Amorphous means that a glass has no long order range or periodic atomic arrangement. As shown in the Figure 1, when a material in liquid form is cooled down from high temperature, the molecular motion slows down and below the melting temperature T_m it can crystallize.
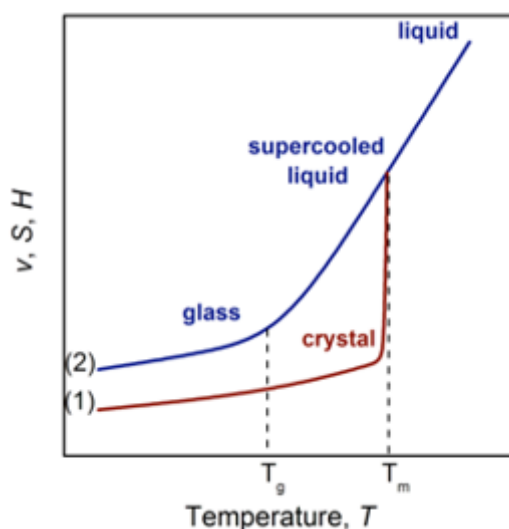
Figure 1. Temperature dependence of a liquid's volume (v), entropy (S) or enthalpy (H) (Ka,12)

Crystalline material is made of particles that are arranged in periodical order and unit cells that are primary building blocks. However, if the liquid is rapidly cooled down, it can also transform into supercooled liquid. During rapid cooling, the growing viscosity of material leads to the atomic ordering into crystalline structure. When the temperature decreases below the glass transition temperature T_g, the liquid solidifies into an amorphous material called glass.

Glasses are considered to be ceramic materials. Depending on their composition, the glasses can have wide variety of properties. However, glasses are hard, brittle, transparent to visible light, chemically and biologically inert, relatively resistant to high temperature and harsh environments, electrically insulative and recyclable (Ca,00). These properties are due to strong covalent and ionic bonds and amorphous structure of glasses.

1.1.2 Phosphate glasses

Phosphate glasses and glass-ceramic (GCs) are based on phosphorus pentoxide (P_2O_5) tetrahedral units as presented in the Figure 2. In the middle of tetrahedral, the outer electron of sp^3 hybrid orbitals of the P ($3s^23p^3$) is promoted to a 3d orbital. The 3d orbital form p-bonding molecular orbitals with oxygen 2p electrons (Cr,61). These tetrahedral units link through covalent bridging oxygens to form various phosphate anions. As seen in the Figure 2, tetrahedral units are classified using Q^i terminology, where *i* means the number of

2

bridging oxygens per tetrahedron. Usually, phosphate glasses are used for optical fibers and laser gain media applications (Mi,91; Su,15) and also for medical applications (Ne,08).
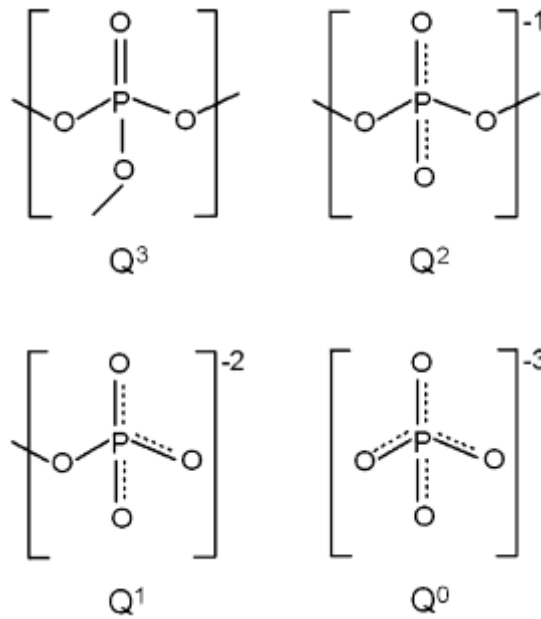
Figure 2. Schematic representation of Q^i phosphate tetrahedral units in phosphate glasses (Ko,10)

Depending on the ratio of oxygen and phosphate in the glass composition, phosphate glasses can be made with a range of structures: cross-linked network of Q^3 tetrahedra (vitreous P_2O_5), polymer-like metaphosphate chains of Q^2 tetrahedra or glasses based on small pyro- (Q^1) and orthophosphate (Q^0) anions.

Phosphate glasses in comparison with most common silicate glasses are easier to fabricate. They possess good chemical durability and show excellent optical properties and ion exchangeability. Most importantly, they exhibit higher solubility for RE ions, without clustering effect, compared to silica based glasses (Sh,05). It is because they have more open and distorted network that silica glass. Indeed, silica glass is made from $[SiO_4^{4-}]$ tetrahedral units in which silicon locates in the center surrounded by four oxygens as illustrated in the Figure 3. Each oxygen is shared between two silicon atoms. These tetrahedral can link together at all four corners to form continuous, 3D network (Sh,05).

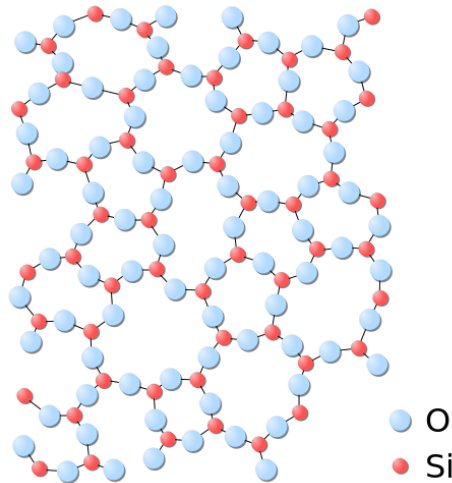Figure 3. The amorphous structure of silica glass (Sc,09)

The main limitation of phosphate glasses is their mechanical and thermal stresses resistance (Mu,13). Their relatively poor mechanical properties is caused by the double bond between phosphate and oxygen in tetrahedral unit which is asymmetrically centered (Br,00). Moreover, their poor chemical durability may also be an issue (Br,00). To improve the physical properties and chemical stability of the phosphate glasses, many network modifiers and intermediates can be added to the glass composition. To increase the stability during melting, alkali metal oxides e.g. Li_2O, Na_2O, K_2O, Rb_2O and Cs_2O can be added. Addition of alkali-earth oxides e.g. MgO, CaO, SrO and BaO in the glass is important to prevent devitrification and to improve the chemical durability. Network intermediates e.g. B_2O_3 and Al_2O_3 can improve the chemical durability and thus, decrease the solubility in water (Mu,13). TiO_2 is known to create cross-linking bonds such as and Ti-O-P (Sh,16), respectively, while ZnO is considered as a modifier and is responsible for the depolymerization of the glass network (Mo,12).

1.2 Biophotonic glasses

1.2.1 Bioactive glasses

Glasses are investigated towards application in bone implants and tissue engineering. This is because they are not toxic and have good mechanical properties. Moreover they show bioactivity. Bioactive material show behaviour between resorbable and bioinert. It create environment allowing osteogenesis (bone growth) achieved by the mineralizing interface (e.g. layer of carbonated hydroxyapatite) which acts as a bonding between tissue and

4

implant. These materials stimulate regeneration of bone when implanted in-vivo. The most well-known composition of 45% SiO, 24.5% Na_2O, 24.5% CaO and 6% P_2O_5, in weight percent is called 45S5 Bioglass[@] (Ca,96). There are other bioactive glass-ceramic such as Ceravital[@] and dense calcium phosphate ceramic such as synthetic hydroxyapatite (HA) (Ca,96). Phosphate glasses are biocompatible and thus suitable for biomedical purposes (Cl,99). Unfortunately, phosphate glasses are also known to have a fast dissolution rate limiting their biomedical application (Sa,00). However, it was shown that the glass dissolution can be tailored and that these phosphate materials can even show dissolution rates similar to the dissolution rate of silicate glasses (Bu,84).

Fluorapatite glass-ceramic are osteoconductive (Br,12). Fluorine is well known to prevent dental cavities by inhibiting enamel and dentine demineralisation, enhancement of remineralisation and inhibition of bacterial enzymes (Fe,00; Th,08). Fluoride-releasing implants might be of used for patients suffering from osteoporosis (Br,12). Glass-ceramic containing fluorapatite have been shown to benefit osseointegration and osteoconduction (Fr,03b). These materials are very interesting candidates for bone tissue engineering due to highest similarity to the natural bone structure compared to other scaffold materials used e.g. metals and polymers. However, one difficulty related to the use of ceramic is imagining them in-vivo to control their dissolution and resorption after implantation. It is because, e.g. bioactive glasses are typically radiotransparent and therefore cannot be detected easily radiographically (Pe,12).

1.2.2 *Optically active glasses*

Glasses doped with rare-earth (RE) elements have great potential as a laser host medium, amplifiers in optical communication systems (Di,01). Rare-earth ions of the lanthanide series are characterized by a closed inner shell of the palladium configuration, with the additional configuration $4f^n \, 5s^2 \, p^6$. For laser technology, the most important RE are: ytterbium- and neodymium-doped gain media for lasers and erbium-doped fibers for erbium-doped fiber amplifiers (Ra,18).

The RE ions are normally trivalent and they have triple positive charge. RE are favorable for achieving laser action, partially due to many excited states that allow optical pumping and subsequent decay to metastable states with high quantum efficiencies and narrow emission lines. Energy levels of the 4f electrons, responsible for optical pumping, are shielded from glass lattice by optically passive 5s and 5p electrons (Di,01). Gain media

doped with RE have long upper state lifetimes, allowing storing of large amounts of energy. This makes RE lasers suitable for pulse generation (Ra,18).

The diagram showing energy levels of the Er^{3+} ion is shown in the Figure 4.
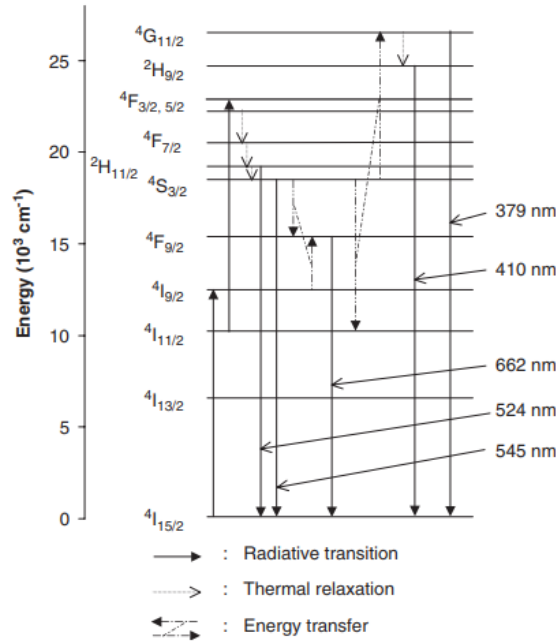

Figure 4. Diagram showing energy levels for Er^{3+} ion and a possible mechanism of upconversion (Pa,07)

Er^{3+} ions operate as a three-level system. Light can be absorbed allowing transition from the ground state $^4I_{15/2}$ to the metastable upper lasting state $^4 I_{13/2}$ (1.49 µm). However, it can also be pumped to $^4I_{11/2}$ (980 nm), $^4I_{9/2}$ (807 nm) $^4F_{9/2}$ (660 nm) or $^2H_{11/2}$ (514.5 nm) higher energy levels from which nonradiative decay to the metastable $^4I_{13/2}$ level, and finally radiative transition from $^4I_{13/2}$ to $^4I_{15/2}$ occur. Er^{3+} lasers have a higher power threshold than Nd^{3+}. Moreover, the $^4I_{13/2}$ metastable state, producing gain at 1500 nm during transmission to the ground state, is of high interest for Er^{3+} doped fiber amplifiers for optical communications applications (Mi,91).

Persistent luminescent (PeL) materials can emit up to several hours after ceasing irradiation (Ai,03). The irradiation source can be for example visible light, UV radiation or X-rays (Ho,09). The first report on the persistent luminescence properties of $SrAl_2O_4:Eu^{2+},Dy^{3+}$ and $CaAl_2O_4:Eu^{2+},Nd^{3+}$ was by (Ya,97). The long lifetime of persistent luminescence is due to trapping of excitation energy and should not be confused with

phosphorescence (Ho,09; Br,12). Phosphorescence is used to describe luminescence from organic compounds involving triplet-to-singlet forbidden transitions, with long decay time, within the luminescence center (Ho,09; Br,12). The mechanism of persistent luminescence of the Eu^{2+} doped materials is presented in the Figure 5 using Sr_3SiO_5:Eu^{2+},Nd^{3+} as an example.
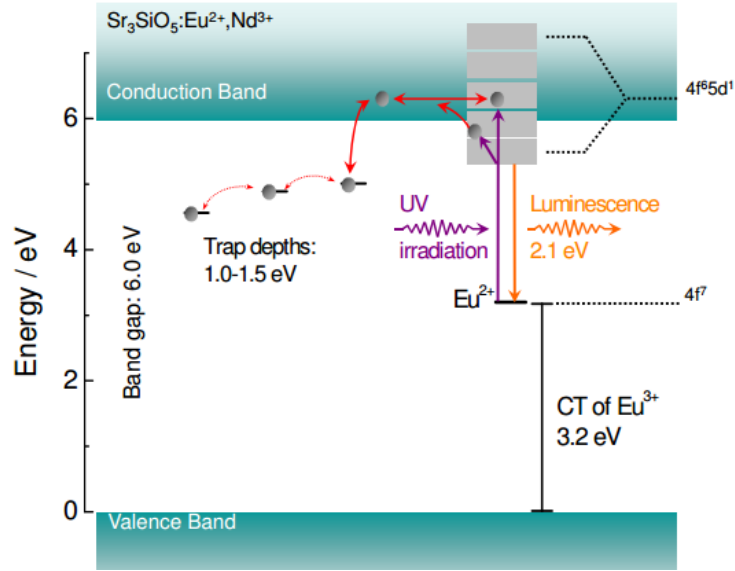

Figure 5. The mechanism of persistent luminescence of the Eu^{2+} in Sr_3SiO_5:Eu^{2+},Nd^{3+} (Br,12)

The excited energy in PeL materials is released from traps with thermal energy. Due to that, PeL is a special case of thermally stimulated luminescence (TSL) (Br,12). Energy is stored in intrinsic traps which can originate from co-doping of the material (Br,11) or from unidentified lattice defects (Ha,10). The Eu^{2+} doped and rare earth (R^{3+}) co-doped alkaline earth aluminates (MAl$_2$O$_4$:Eu^{2+},R^{3+}; M: Ca and Sr) were the first generation of the modern persistent luminescence materials, appeared in both the commercial market and in research laboratories since 1995 (Ho,09).

The irradiation of the material results in the photoexcitation of Eu^{2+} via the $4f^7$ ground state to $4f^65d^1$ excited state. The excited state overlaps with the conduction band of Sr_3SiO_5 which allows easily the escape of some electrons from $4f^65d^1$ directly or assisted by thermal energy (kT), to the conduction band of Sr_3SiO_5. In the conduction band, the electrons move freely until they return to the europium center or meet a defect. They are trapped close to the bottom of the conduction band. When thermal energy is later absorbed, reverse decharging process is initiated in which the trapped electrons escape back to the conduction band in

temperature controlled gradual release and populate the $4f^65d^1$ levels of Eu^{2+}. This is followed by the non-radiative (within the $4f^65d^1$ states) and finally by the radiative relaxation of Eu^{2+} (from the lowest $4f^65d^1$ state) producing the persistent luminescence. The retrapping of the electrons can occur in every step of the decharging process still lengthening the persistent luminescence. (Ho,09; Br,12)

The fundamental challenge in modern biology is to observe physiological processes at the molecular level and in vivo (De,07; Li,13). Due to that, new optical imaging techniques, in which photons are carrying information, are developed and can be utilized in pharmacology, molecular and cellular biology as well as diagnostics (De,07; Sa,18). In vivo optical imaging using fluorescent, probe is commonly used but their application is limited due to numerous disadvantages: autofluorescence (Fr,03a) from tissue organic components that often results in poor signal-to-noise ratio and difficulties with deep tissue imaging due to intrinsic tissue signal attenuation (Ch,90). These limitations can be solved using PeL materials. Their long-lasting afterglow allows the removal of the background noise originating from in situ excitation. Thus, the significant signal-to-noise ratio improvement allows the detection in rather deep organs and real-time biodistribution monitoring of active elements hours after injection (De,07). In the recent years, the use of persistent luminescent particles has been investigated as optical probes to image vascularization, tumors and grafted cells (Ma,14).

Saarinen et al. investigated PeL borosilicate and phosphate bioactive bodies obtained by sintering glass particles with PeL MPs such as $SrAl_2O_4:Eu^{2+},Dy^{3+}$ (Sa,18). After immersion in simulated body fluid, a decrease in the PeL from the bodies was observed and was related to the progressive mineralization overtime of the sintered bodies. This PeL bioactive bodies could be used to track the changes in the PeL overtime. Therefore, such materials have a real potential application as biophotonic sensors to track dissolution and mineralization of the implant in the body.

1.3 Glass-Ceramic

Glass-ceramics were invented in mid-1950s by S.D. Stookey (St,59). Few main applications of glass-ceramic are cook-top panels, dinnerware, electronics, medicine and dentistry, tough glass-ceramic and optical materials (Go,02). As mentioned before, a glass is an amorphous solid. During the preparation of glasses, it is possible to precipitate crystalline phases using controlled nucleation and crystallization process. It will result in

creation of glass-ceramic, material with amorphous glass network in which crystals are homogenously embedded. Crystallization makes the glasses opaque, however they still can be transparent e.g. if the crystals are smaller than the wavelength of visible light (Be,69). Due to the crystallized phase, the mechanical properties of the glass-ceramics are better than those of glasses and the glass-ceramics are strong materials (Ho,12). It is due to the presence of cleavage planes and grain boundaries in crystallized glass which act as obstacle for fracture propagation. Other mechanical, thermal, electrical or optical properties can also be improved in glass ceramic.

The advantages of fluoride glasses and crystals are: lower phonon energy than oxide glasses and high transparency from the near-UV to the middle IR, with excellent RE ions solubility and low vibrational energies (Ku,01). However, oxide glasses have better chemical durability, thermal stability and mechanical strength than the fluoride glasses (Wa,93; Go,02). They are also cheaper and easier to fabricate into rods, fibers or planar waveguides than the fluoride glasses.

The rare earth ions like Er^{3+} should selectively precipitate into fluoride crystals in glass-ceramic to increase their excited state lifetimes and cross sections compared to RE ions embedded in glass phase according to (Ku,01). Due to their low phonon energy which makes them more efficient for infrared upconversion, the oxyfluoride glass-ceramics are great candidates as laser host materials, compared to oxide glasses with limited RE solubility and transparency (from ~300nm–3000nm). These oxyfluoride glass-ceramics combine the advantages of fluoride crystals and oxide glasses. There are few methods to process glass-ceramics.

1.3.1 Nucleation and growth theory

Glass-ceramics can be produced using controlled heat treatment during which submicroscopic nuclei are formed and grow into macroscopic crystals. These two stages are called nucleation and crystal growth which are schematically presented in the Figure 6.
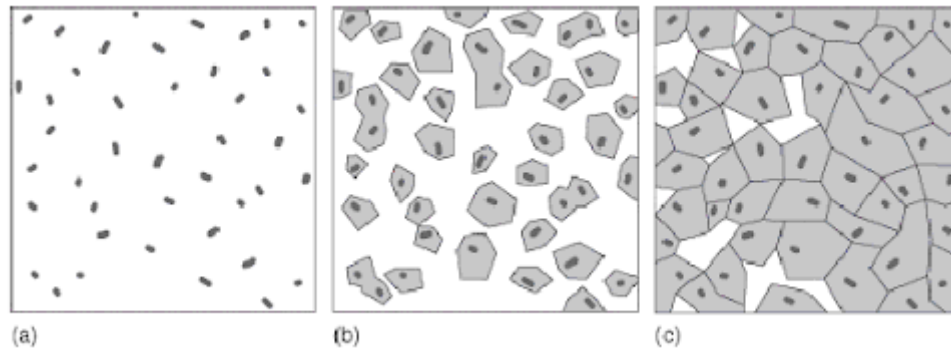
Figure 6. Process of controlled heat treatment a) nuclei formation, b) crystal growth on nuclei, c) glass-ceramic microstructure (Ho,12)

The rates of nucleation and crystal growth depend on temperature and time. Nucleation also depends on the addition of nucleating agent into the glass. To design proper controlled heat treatment process, the thermal properties of glass should be carried out using a DTA to obtain the glass transition and crystallization temperatures.

Nucleation and crystal growth rates as function of temperature are presented in the Figure 7. The crystal grow can be initiated, after nucleation, when the nuclei radius r is bigger or the same as the critical radius of nuclei r*. This happens at the temperature range where nucleation and growth curves overlap. At the Ostwald-Miers temperature range (metastable supercooling), the crystals can grow only from nuclei which were formed in the nucleation range (Ho,12).
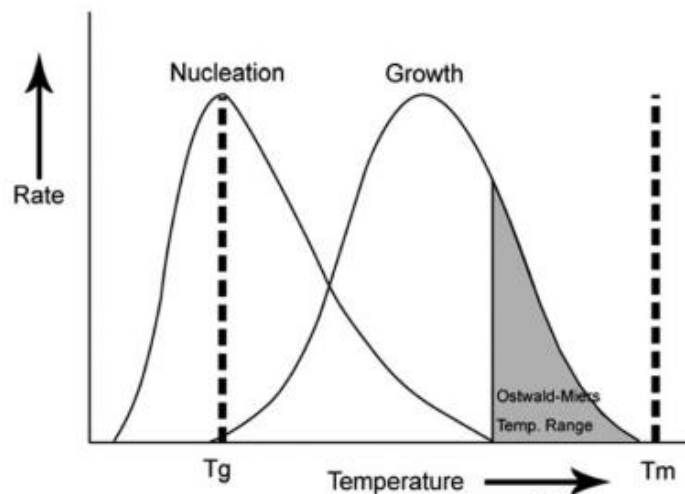

Figure 7. Nucleation rate (I) and crystal growth rate (V) as function of temperature. Modified from (Ka,14)

However, if a glass is cooled down from high temperature and heat treated in the Ostwald-Miers range, no nuclei and crystals won't be formed. Knowing these relations is important to control the crystallization process.

Nucleation is a process in which seed crystal starts the crystallization process. Heterogeneous nucleation occurs when adding nucleation sites to glass composition while nucleation without preferential nucleation sites leads to homogeneous nucleation.

The change in Gibbs-free energy ΔG between the melt and the crystal is thermodynamic driving force the glass-crystal phase transition. The dependence between Gibbs free energy (ΔG) and radius of nuclei (r) is presented in the Figure 8.
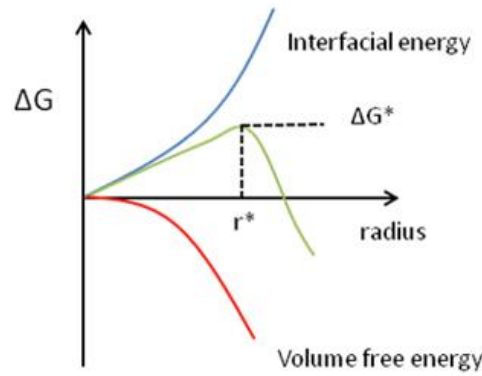
Figure 8. Dependence between Gibbs free energy (ΔG) and radius of nuclei (r)

The thermodynamic barrier at which the change of free energy is enough for growing the nuclei is called critical Gibbs energy. Critical Gibbs energy in heterogeneous nucleation (ΔG_H^*) is given by:

$$\Delta G_H^* = \Delta G^* f(\theta), \tag{1}$$

Where ΔG means change in the Bibbs energy, and $f(\theta)$ is described by equation:

$$f(\theta) = \frac{(2+\cos\theta)(1-\cos\theta)^2}{4}, \tag{2}$$

Where θ is contact angle between nucleus and mother phase.

The critical radius of nuclei, r^* at which $\Delta G_H^* = \Delta G$ is described by:

$$r^* = -\frac{2\gamma}{\Delta g_v},\qquad(3)$$

Where γ means the interfacial energy required for the formation of the new surface of the nucleus, and Δg_v means the free-energy change per unit volume that is produced by the formation of nuclei.

Particles with radius of r* or larger are capable of further growing whereas particles with smaller radius than r* are called subcritical particles and are not capable of growing and will eventually disintegrate in the glass.

The barrier energy needed for the heterogeneous nucleation is reduced by wetting angle. Contact angles greater than zero between phases facilitate particles to nucleate. Phases in heterogeneous nucleation and contact angle θ are illustrated in the Figure 9.
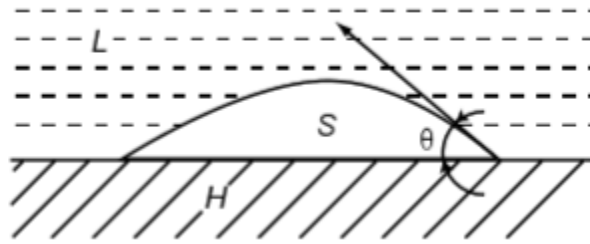
Figure 9. Different phases in heterogeneous nucleation. Θ is contact angle between S (formed crystal) and L (melt/liquid phase). H represents the heterogeneous substrate (Ho,12)

For $0°<\theta<180°$, heterogeneous nucleation occurs and nuclei with radius of r* are preferentially formed.

Nucleation process can be also divided for volume and surface nucleation, schematic which is shown in the Figure 10.

Figure 10.   Schematic of volume and surface crystallization.

The volume nucleation is predominantly used in the production of glass-ceramics. Volume nucleation can be achieved using nucleating agents such as gold, silver and copper metals in ionic form (St,59). Nucleating action is due to an epitaxial effect based on similar lattice parameters. However, heterogeneous nucleation with metals has been successfully applied in the development of glass-ceramics for dental applications. Although most glass-ceramics are prod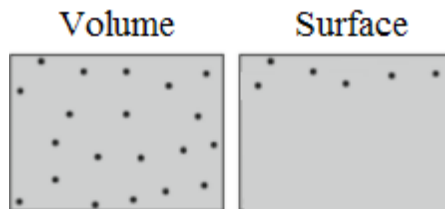uced with volume nucleation, there are glasses in which controlled crystallization can only be achieved with surface nucleation. However, this kind of nucleation is harder to control and not yet well understood.

TiO_2, ZrO_2, P_2O_5, Ta_2O_5, WO_3, Fe_2O_3, and F were found to act as nucleating agents. The increase in the CaF_2 at the expense of CaO in the system $75NaPO_3–(25 − x)CaO–xCaF_2$ (in mol%) was found to decrease the crystallization tendency of the glass after heat treatment (Cu,16). As shown in Figure 11, the glass-ceramics with x=0 and x=20 were respectively opaque and slightly-translucent.

Figure 11.   Picture of the glasses with different content of CaF_2 heat treated for 17 hours at (T_g + 20 °C) and then for 60 minutes at T_p in (Cu,16).

The crystallization tendency of the glass was related to their structure: an increase in the CaF_2 content increases the polymerization of the phosphate network leading to an increase in the number of Q^2 units at the expense of the Q^1 units and so to a shift of the optical band gap to lower wavelength. This change in the glass structure reduces the crystallization tendency of the glass.

The same effect was observed in Er^{3+} doped glasses with composition $75NaPO_3-(25 - x)CaO-xCaF_2$ (in mol%) reported in (No,18). Moreover, the study showed that the diffusion mechanism of Er^{3+} ions during heat treatment is effected by the glass host. The pictures of the glass-ceramics with different CaF_2 contents are presented in the Figure 12. Glass-ceramic with x=0 and x=25 were respectively slightly-translucent and transparent.
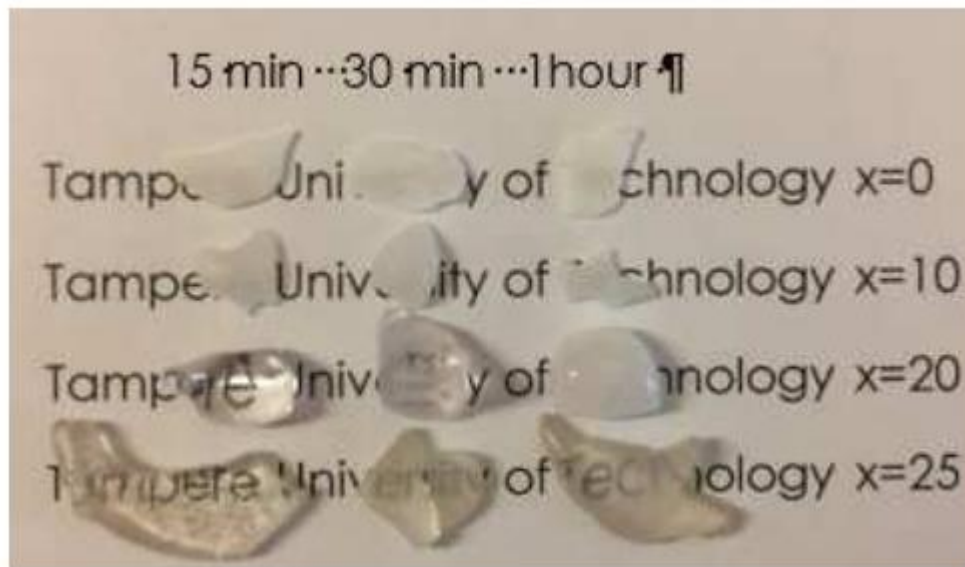

Figure 12.   Picture of the glasses with different content of CaF_2 heat treated for 17 hours at $(T_g + 20 °C)$ and then for 15, 30 and 60 minutes at T_p (No,18)

1.3.2 Direct particles doping method

The production of glass-ceramic using controlled nucleation and growth process has some limitations. Conventional method doesn't allow for a high level of compositional and structural control (Zh,16). The maximum ions concentration that can be incorporated into crystals and the control over arrangement of ions at specific crystalline sites are also limited (Zh,16). Moreover, the crystals may continue to grow during post annealing or reheating process such as fiber drawing. The size of the crystals is proportional to light scattering and results in high optical loss (Zh,16). Finally, glass-ceramic method doesn't allow for growing core-shell and heterogeneous nanostructures to engineer optical properties (Zh,16).

Zhao et al. presented direct doping method which is used to integrate Ln^{3+} containing nanocrystals (NCs) in glass (Zh,16). In direct doping method, crystal particles and glass are prepared separately, and the crystals are subsequently added to glass melt. The most

14

important parameters to control are the doping temperature at which the particles are added and the doping time before casting the glass after adding the particles. The maximum doping temperature is limited by the degradation temperature of crystal particles. This temperature can be estimated using differential thermal analysis (DTA). The minimum doping temperature is limited by the viscosity of glass melt that should be low enough to disperse crystals. The doping time should also be properly chosen. Doping time is proportional to the dispersion of the crystal particles but disproportional to the dissolution of the crystals in the glass melt. Controlling these parameters allows for achieving favorable properties of glass-ceramics and the survival of crystals in high temperature glass melt.

In the Figure 13, the structural differences of glass and glass-ceramic prepared using different production methods are presented.
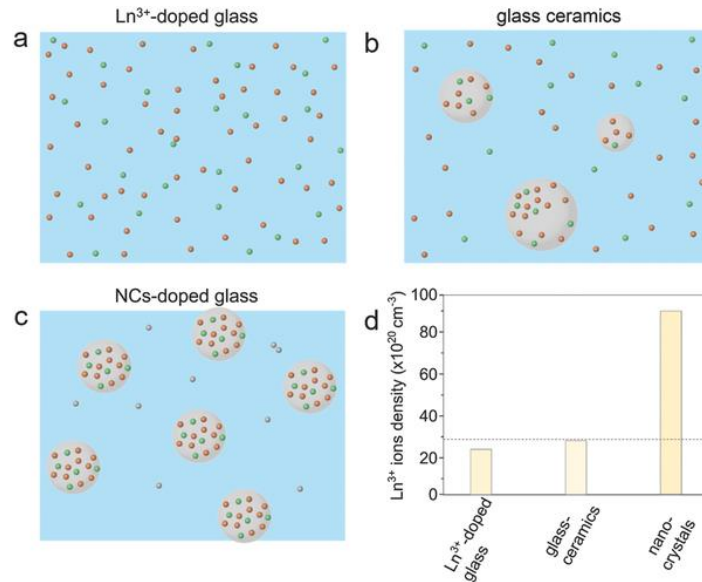
Figure 13.   a-c) Presentation of glass and glass-ceramic structures using different production methods. Nanocrytals-doped glass was prepared using direct doping method. d) Schematic of Ln^{3+} ion densities available in glasses. (Zh,16)

It can be seen that ion densities are the largest inside of nanocrystals produced via direct particles doping method. In conventionally prepared glasses, there is no crystals and ions are distributed homogenously in glass phase.

In this research, biophotonic PeL phosphate glasses with composition (75 $NaPO_3$-25 CaF_2)$_{100-x}$-(TiO_2/ZnO/MgO)$_x$ (in mol%) were prepared to evaluate their potential utilization as bone implant. This glass system was chosen as its composition contains minerals naturally occurring in bone structure: calcium and phosphate are natural components of human bone.

Bone is a mineralized tissue, which is composed of an organic matrix strengthened by deposits of calcium phosphate in the form of hydroxylapatite (HA) crystals (Ba,06). Calcium phosphate composition is similar to one of bone mineral and induces a biological response similar to the one generated during bone remodeling (Ba,06). The investigated glasses were doped with Er^{3+} in order to prepare new active bioactive glass-ceramics using the nucleation and growth technique. The glasses were also prepared with 0.25-1.0wgt% of luminescent pigment $SrAl_2O_4:Eu^{2+},Dy^{3+}$ using the direct doping method.

1.4 Patterning

Nanofabrication is focused on processes involved in manufacture elements in nanosize which are crucial for modern technology which drives toward miniaturization. The purpose of nanofabrication is to produce nanoscale structures that form part of a system, device, or component in large quantities and at a very low cost. Fabrication methods can be divided into two groups: top-down and the bottom-up method.

Top-down approach is based on removing the extra material from the bulk material to generate nanofeatures. The processes involved in top-down strategies rely mostly on different thin film deposition, lithography and etching techniques. Bottom-up approach utilizes individual molecules or atoms to create the structure layer by layer. Due to the nano size of features the bottom-up approach is more efficient. Obviously, manipulation of individual atoms and molecules is very complicated process which requires special equipment and environment to be successful. Even particles of dust are relatively big in nanoscale and can affect manufacturing process. Sterile, shockproof and vibration-proof environment is needed to achieve precise manipulation of molecules. To provide this requirements nanofabrication processes are carried out in clean room which is space with controlled temperature, humidity, pressure and very low level of contamination (controlled number of particles per cubic meter) (Ha,16; Na,19).

In this study, we utilized top-down micro/nanofabrication processes to pattern glass samples. The goal was to analyse the feasibility to create micro sized patterns on phosphate glass surfaces. It is important because micro/nanofabrication processes are crucial for manufacturing waveguide-based photonic devices and metasurfaces for optical applications such as lasing, imaging and optical biosensing. It is also important in biomedical applications where cell adhesion and integration of the implants in the host tissue is affected by surface

wettability which can be controlled by patterning of hydrophilic and hydrophobic stripes (Gi,17).

2 Materials and methods

2.1 Preparation of the materials

2.1.1 Glasses

Fluorophosphate glasses with the composition $(75\ NaPO_3\text{-}25\ CaF_2)_{100\text{-}x\text{-}0.25}$-$(TiO_2/ZnO/MgO)_x$, doped with 0.25mol% Er_2O_3, with x=0 and x=1.5 were prepared using standard melting processing by mixing powder chemicals and melting them for 5 minutes in air in platinum crucible. The chemicals were $NaPO_3$ (Alfa-Aesar, technical grade), CaF_2 (Honeywell-Fluka, 99%), Er_2O_3 (Sigma-Aldrich, 99,9%), MgO (Honeywell, ≥99%), TiO_2 (Sigma-Aldrich, 99,8%) and ZnO (Sigma-Aldrich, 99,99%) in powder form. Finally, glasses were quenched and annealed for 5h at 200°C to release the stress from the quench.

Depending on their composition, the glasses needed to be melted at different melting temperatures to obtain a crystal-free material (Table 1).

Table 1. Phosphate glasses and their melting temperature

x (mol%)	Glass label	Melting temperature T_m (°C)
0	Ref 1	1000
0	Ref 2	900
0	Ref 3	950
1.5 Zn	Zn	1000
1.5 Ti	Ti	1025
1.5 Mg	Mg	900

2.1.2 Glass-ceramics

Glass-ceramics were produced from the as-prepared glasses using controlled heat-treatment as explained in the previous section. Firstly, the glasses were kept for 17h at 20°C above their glass transition temperature T_g. Secondly, the temperature was increased to the glasses maximum crystallization temperature T_p for 1,3 or 6 hours.

18

2.1.3 PeL glasses

The PeL glasses were prepared by adding 0.25-1.0wgt% of luminescent pigment $SrAl_2O_4:Eu^{2+},Dy^{3+}$ (Realglow®) in powder form in the melt of the glass with the composition (75 $NaPO_3$-25 CaF_2) (mol%). Firstly, the glasses were melted for 5 min at 925˚C. The particles were added at different doping temperatures. x min after adding the particles (dwell time), the glasses were cast and annealed at 200˚C for 4h. The different doping parameters as well as the sample code are listed in the Table 2.

Table 2. Doping parameters used to prepare the PeL glasses

Glass label	Doping temperature T_{doping} (˚C)	Dwell time t (min.)	Pigment (wgt%)
875-3-0.5	875	3	0.5
875-5-0.5	875	5	0.5
875-10-0.5	875	10	0.5
900-3-0.25	900	3	0.25
900-3-0.5	900	3	0.5
900-3-1.0	900	3	1.0
900-5-0.5	900	5	0.5
900-10-0.5	900	10	0.5

2.2 Scanning Electron Microscope (SEM)

In this study, the imaging and the composition microanalysis of the glasses were carried out using Carl Zeiss Crossbeam 540 Gemini Scanning Electron Microscope (SEM) connected with an Oxford Instruments Energy Dispersive X-ray Spectroscopy (X-Max[N] 80) detector (EDS). The glass samples were polished and coated with carbon. The carbon coating is usually used for non-conductive samples to improve the image contrast. Polishing is necessary for compositional microanalysis using EDS to get rid of scratches. If scratches occur, the uneven topography will interfere with signal reaching the detector.

SEM allows one to image materials using high resolution ~10 nm, much smaller than in optical microscope due to the smaller wavelength of electrons in comparison to photons used in optical microscope. Electrons are generated and accelerated in electron gun, then they travel

down the column in vacuum environment. The electron beam is focused by lenses onto the specimen producing spot size smaller than 10 nm. The surface of specimen is scanned point by point while the beam electrons interact with the specimen electrons. Schematic presentation of SEM equipment is presented in the Figure 14.
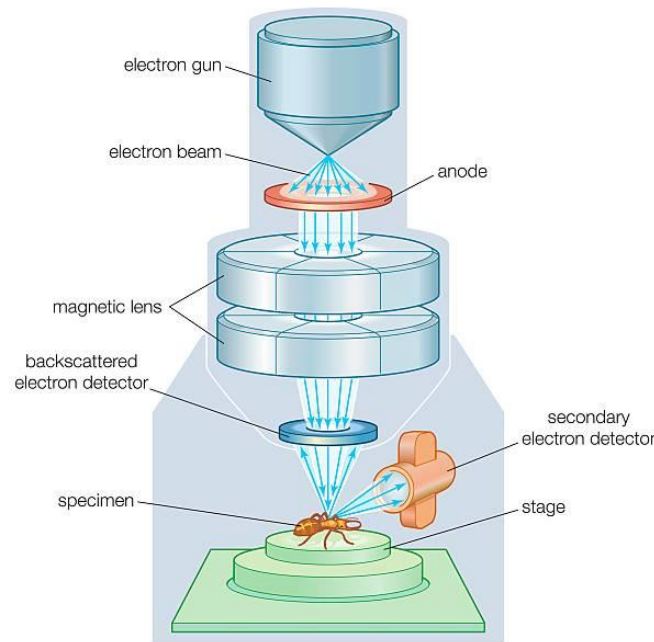
Figure 14.   SEM equipment illustration

When electrons from beam interact with specimen, they can result in elastic and inelastic scattering (Go,17):

- Elastic scattering happens when beam electrons interact with atoms of specimen and its trajectory is changed creating the so called backscattered electron (BSE). After scattering, some electrons can leave the sample surface and so can be detected by detector. Scattering is called elastic because there is no change in kinetic energy and velocity of electrons. Electrons are more scattered and deflected when interacting with heavy elements. Due to that, the backscattered electrons can carry information about the composition of the sample, since heavy elements will create more BSE than specimen made of light elements.

- Inelastic interactions of beam electrons with specimen atoms produce secondary electrons (SE). These SE are created when primary electrons from beam eject electrons from specimen atom. This scattering is inelastic because primary electrons are losing their energy that is transferred to specimen electrons. SE

electrons have low energies, smaller than 50 eV and due to that, only electrons very close to the surface of specimen have enough energy to leave the specimen and to be detected. Due to the edge effect, more secondary electrons are emitted at the edges or areas facing towards the detector and produce brighter regions in the image. Consequently, SE carries information about topography of sample and is mainly used for imaging purposes.

Inelastic interaction produces two kinds of X-rays: characteristic and bremsstrahlung.

- The bremsstrahlung X-rays are produced when the primary electrons are slightly deflected and slow down due to inelastic interaction with specimen's atom. The lost energy of primary electron is emitted in the form of Bremsstrahlung X-ray.
- When electron transits into lower energy shell vacancy it will emit characteristic X-ray equal to the difference between electron shells. These X-rays are called characteristic because they have characteristic energies that are specific for every element's electron. Therefore, the X-rays can be used for mapping of elemental composition using Energy Dispersive X-ray Spectroscopy (EDS) technique.

The EDS detector can collect x-rays produced by primary electrons interactions with specimen atoms. The major signals produced during electron-matter interactions used in SEM imaging and EDS elemental mapping are shown in the Figure 15.
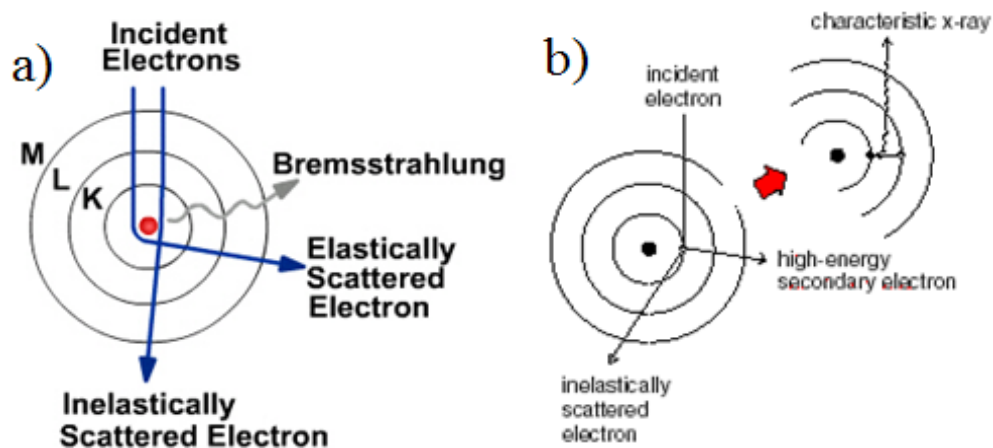
Figure 15. a) Incident electron interact with specimen sample elastically, without losing energy. Elastically scattered electron is called Backscattered Electron. It can also interact inelastically, losing energy that is transformed into Bemsstrahlung X-ray, b) Incident electron ionize specimen's atom and specimen's electron is ejected. Electron from higher energy shell occupy the vacancy and Characteristic X-ray is produced (Xr,18)

2.3   X-ray diffraction

In this study, the glasses and GCs were crushed into powder and their crystal structure analyzed using the Panalytical EMPYREAN multipurpose X-Ray Diffractometer (XRD) using nickel filtered copper K-Alpha radiation. The spectra were obtained using the Bragg-Brentano geometry and by rotating the sample holder around the Phi-axis at a constant speed of 16 revolutions per minute.

In this technique, x-rays are produced and accelerated onto specimen where they interact with specimen atoms. The x-ray tube is made of tungsten filament as cathode and copper as anode. Cathode emits electrons that are accelerated onto the anode. Electrons interact inelastically with anode's atoms and characteristic x-rays are produced. Primary optics, shown in the Figure 16, concentrate and direct the x-ray beam onto the specimen surface.
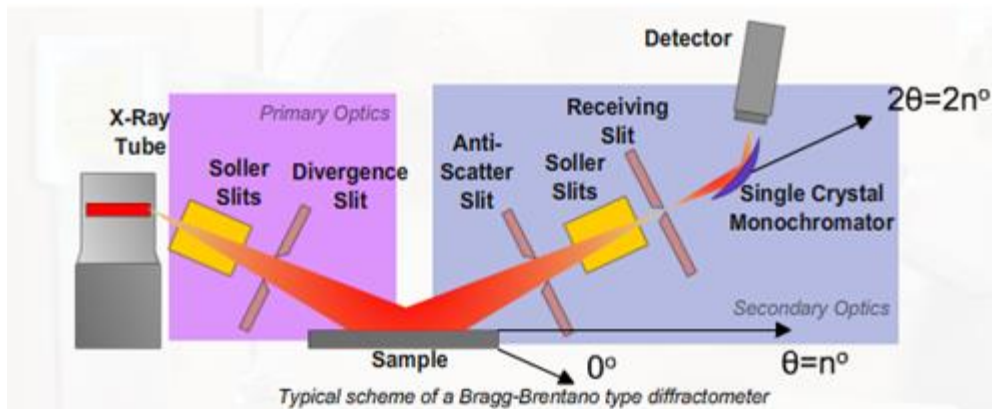
Figure 16.   The schematic illustration of diffractometer with Bragg-Brentano type geometry. Retrieved from (Pa,18)

However, only x-rays with the most intense characteristic lines: $K\alpha_1$ and $K\alpha_2$ are used. Other x-rays should be filtered out using monochromator. Incident x-rays are scattered by crystal lattice and can further interfere with each other. If scattered x-ray waves are not in phase with each other, they will undergo destructive interference. This happens to most of the scattering. However, at certain angles, described by Bragg's Law, scattered x-rays will interfere constructively and diffracted ray occurs. The diffracted x-rays are concentrated and directed by secondary optics onto detector and create maximum intensity peak in spectrum. Bragg's angle is unique for each crystalline structure and can be used for its identification in different materials.

The equation for Bragg's Law is following:

$$2d \sin \theta = \lambda, \tag{4}$$

Where d denotes lattice interplanar spacing of the crystal, θ is the x-ray incident angle (Bragg's angle), and λ the wavelength of the x-rays.

For better understanding, the relation described by Bragg's Law is presented in the Figure 17.
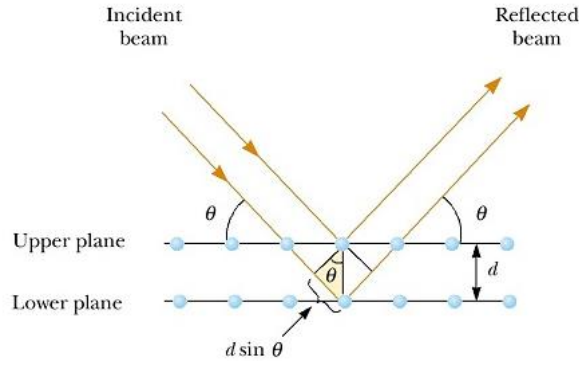
Figure 17.   Illustration of Bragg's condition for constructive interference of scattered, incident beam. Retrieved
(Di,18)

2.4   Physical properties

The density of the glasses was measured using the Archimedes' principle stating that the weight of object immersed in fluid is decreased by amount of weight of displaced liquid. This observation is described by the following equation:

$$\frac{\rho}{\rho_{fluid}} = \frac{m}{m - m_{immersed}},$$
(5)

Where m denotes the mass of an object, immersed the mass of an immersed object, ρ the density of the object, and ρ_{fluid} the density of fluid.

This method gives an ability to measure the density of samples with irregular shape like e.g. glass pieces. For the density measurement, an OHAUS Adventurer Analytical scale was used. The chosen liquid was ethanol taking under the consideration the high hydrophilicity of the glass samples. Firstly, samples were weighted in air and then in ethanol. Secondly, the Equation 6 was used to calculate the density of glass:

$$\rho_{glass} = \frac{m_{air} * \rho_{ethanol}}{m_{air} - m_{ethanol}},$$
(6)

Where m_{air} denotes the mass of glass in air, $m_{ethanol}$ the mass of glass in ethanol, ρ_{glass} the density of glass, and ρ_{fluid} the density of ethanol at the temperature at the time of measurements.

The accuracy of measurement is $\pm 0.02 g/cm^3$.

2.5 Thermal analysis

The thermal analysis was carried out using NETZSCH STA 449 F1 Differential Scanning Calorimetry (DSC) equipment depicted in the Figure 18. These measurements are necessary to evaluate the glass transition temperature T_g, the onset of crystallization T_x, and the crystallization temperature T_p values of glass. During the measurement, the sample pan with powdered glass sample and the pan with reference material were heated using a heating rate of $10°C/min$ (see Figure 18).
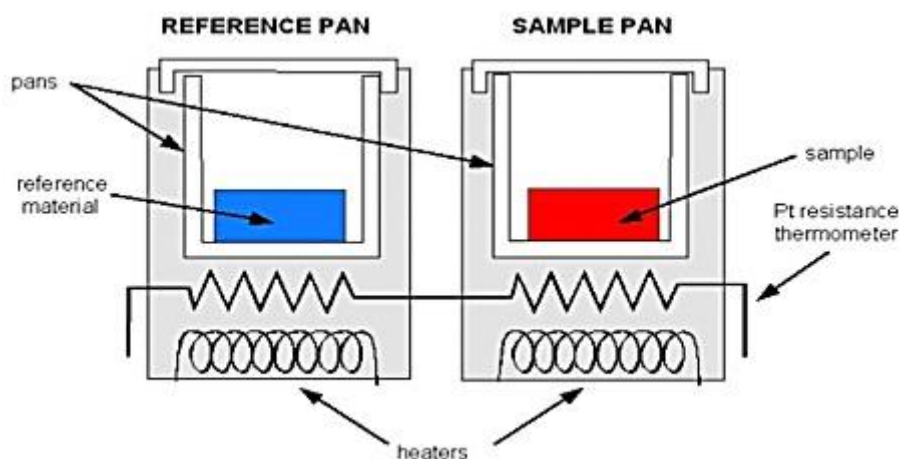

Figure 18.   Schematic presenting DSC equipment (Le,13)

The DSC measures the energy change during the absorption of energy in form of the heat. As the absorbed energy is different for the sample of investigation and the reference material, their energy enthalpies will also differ. The information about the difference is given in heat flow that is the amount of power input (Watts) needed to increase the temperature of mg of sample by $1°C$. The reactions can be divided for endothermic and exothermic. During endothermic process, the energy is absorbed whereas in an exothermic process the energy is released. The transition from glass to crystalline solid is an exothermic process, and results in a peak in the DSC signal

On the other side, the glass transition temperature is not characterized by a release or an absorption of energy, but by a change in heat capacity. T_g is in fact a range of temperature over which an amorphous solid transforms into a liquid and appears as a step in the thermogram. However, the change in the enthalpy may occur producing an endothermic peak. The glass transition temperature shouldn't be mistaken with the melting temperature that occurs in crystallized materials.

The result of a DSC measurement is the glass thermogram, like the one shown in the Figure 19.
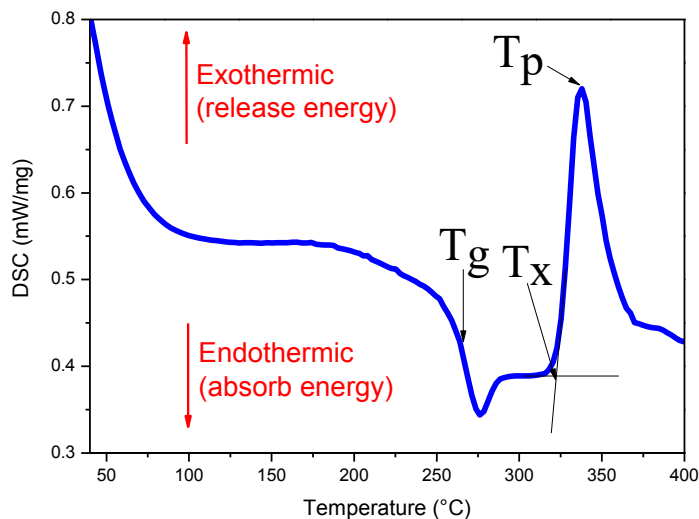

Figure 19.   Typical thermogram produced using a DSC

The glass transition temperature T_g is taken at the inflection point of the endotherm, obtained by taking the first derivative of the DTA curve. The crystallization temperature T_p is found as the maximum of the exothermic peak. The onset of the exothermic peak is onset of crystallization T_x. The accuracy of these measurements is $\pm 3°C$.

2.6 Optical properties

In this study, the absorption and transmission spectra were measured using UV-Vis-NIR spectrophotometer (UV-3600 Plus, Shimadzu) from 200 to 1800 nm with 0.5 nm interval. Samples were polished and their thickness was evaluated using a digital caliper with an accuracy of ± 0.05 mm.

The schematic presentation of spectrophotometer used for transmittance and absorbance measurements is shown in the Figure 20.
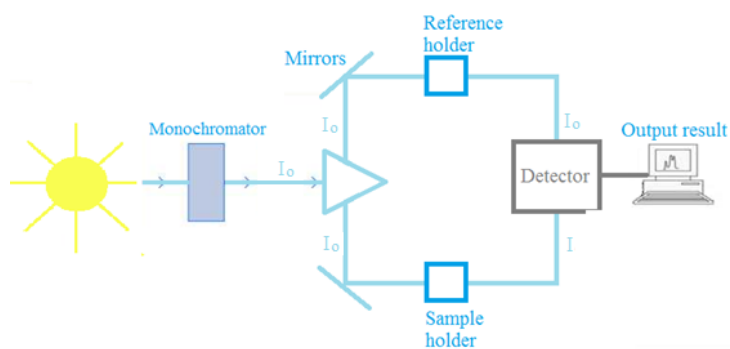
Figure 20.   Construction of double beam spectrophotometer

Usually, a halogen lamp is used as the light source. The monochromators disperse the light into narrow spectral bands, from which one will be further split into two beams. Beams will travel into sample's compartment, where one passes through the sample holder and the second one through the reference holder. Next, the light beams enter the detector and the computer presents the output result. The spectrophotometer measures the changes in the intensity of initial beam I_o after passing through the sample.

The transmittance gives information about how much light is transmitted when light passes through the sample. It can be calculated using the following equation:

$$T = \frac{I}{I_o}, \tag{7}$$

Where T denotes the transmittance, I the intensity of the light that passes through the sample, and I_o the intensity of the light that passes through the reference (empty holder).

The absorbance gives information about how much light is absorbed when light passes through the sample. It can be calculated using following equation:

$$A = \log_{10} \frac{I_o}{I}, \tag{8}$$

Where A denotes the absorbance.

During absorption, the light intensity is decreased. The reduction in the intensity is recorded by the detector and is plotted as a function of the wavelength. The level of absorption

depends on the concentration of the absorbing molecules and the thickness of the sample. The absorption coefficient can be calculated:

$$\alpha = \ln(10)\frac{A}{L}. \tag{9}$$

Consequently, the absorption cross-section [cm^{-1}] can be derived from Beer-Lambert Law:

$$\alpha(\lambda) = \frac{2.303}{NL} log\left(\frac{I_0}{I}\right), \tag{10}$$

Where N is the number of ions per cm^3 absorbing at the specific λ. The accuracy of the absorption cross-section is $\pm 10\%$.

2.7 Structural analysis

2.7.1 IR spectra

The IR spectra of the glasses were measured using a Perkin Elmer Spectrum FTIR2000 spectrometer with Attenuated Total Reflection (ATR) mode between 600 and 2000 cm^{-1}. The resolution was 2 cm^{-1} and obtained from 8-scan accumulation. The samples were crushed into powder.

The IR spectra were obtained using Fourier-transform infrared spectroscopy (FTIR) technique based on the interaction of infrared radiation with matter. The infrared radiation is an electromagnetic radiation having wavelength range of about 700 nm to 1 mm. These wavelengths are higher than that of visible light as seen in the electromagnetic spectrum in the Figure 21.
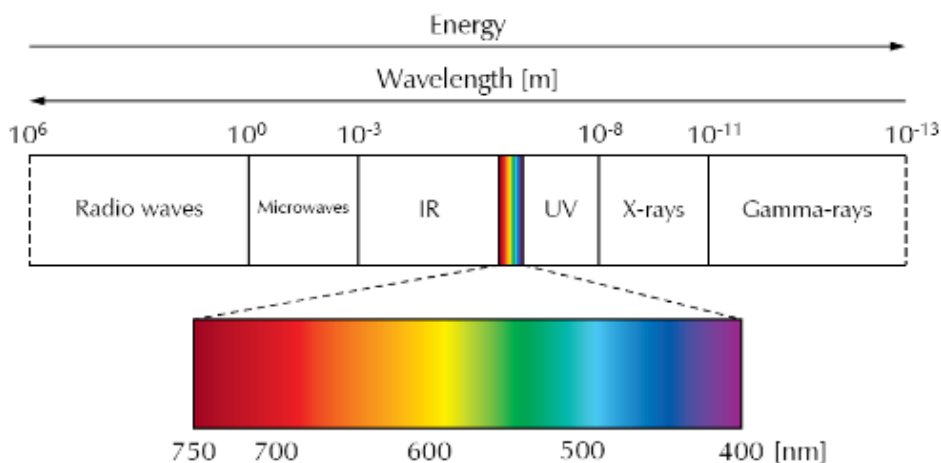
Figure 21.　　　　Electromagnetic spectrum. Retrieved from (Ov,18)

The energy of infrared radiation photons is relatively small and is not able to excite electrons. However, these energies are large enough to induce vibrations of covalently bonded atoms. The exact frequency, at which a given vibration occurs, is determined by the strengths of the bonds involved and the mass of the atoms. The absorption peaks in output spectrum correspond to the frequencies of vibrations between the bonds. Consequently, the FTIR technique is commonly used to study the structure of a glass.

FTIR spectrometer is made of an IR source, a beam splitter, a stationery and a moving mirror, a sample holder and a detector. The structure of a FTIR spectrometer is shown in the Figure 22.
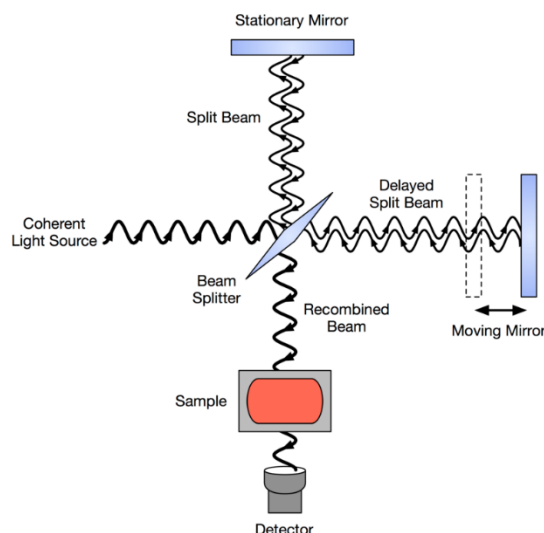
Figure 22.   Schematic of a FTIR spectrometer (Fo,18)

The infrared energy emitted by the source is split into two even portions by the beam splitter. One half goes to the moving mirror while the second part goes to the stationery mirror. The mirror reflects the beam back onto the beam splitter. The distance between the moving mirror and the beam splitter can be changed and consequently, it will affect the interference of beams. This results in the creation of constructive and destructive interference, resulting in an interferogram. Next, the recombined beam travels through the sample which absorbs different wavelengths. The detector collects the interferogram which is the energy versus time signal, for all wavelengths. The mathematical function, the Fourier transform, is used to convert interferogram into an intensity versus wavelength, as illustrated in the Figure 23.
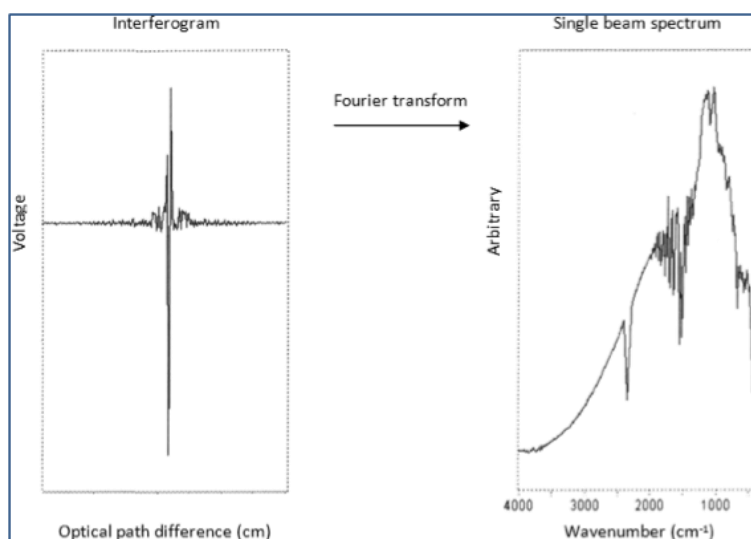
Figure 23.   Fourier transform from interferogram to actual IR spectrum (Sm,07)

2.8   Spectroscopic properties

2.8.1   *Er³⁺ luminescence properties, including lifetime measurement*

In this study, the emission at 1.5μm and the upconversion spectra were measured at room temperature using a monochromator (Digikrom, DK480) and a lock-in amplifier (Stanford Research Systems, SR830) equipped with a TEC-cooled silicon photodiode. The materials were excited using a TEC-cooled fiber-coupled multimode laser (II-VI Laser Enterprise, λ_{exc}~980 nm, incident power on sample 23.5 mW). Finally, the emitted light was collimated, collected and directed to the monochromator through a long-pass filter with a cutoff at 1200 nm (Thorlabs, FEL 1200). The smallest excitation spot size is estimated to be ~100 μm in diameter.

When an atom is excited, it moves from its ground state to a higher energy shell. The excitation can be caused by e.g. collision with electron or photon which gives its energy to an atom's electron. However, the electron won't stay forever in the excited state, and after some time it will come back to its ground state. During this transition, the energy difference between excited state and ground state will be emitted in the form of photon. Emitted photons will have specific wavelength in the spectrum depending on their energy.

The emission spectroscopy is a technique that examines the wavelengths of photons emitted when material's electron transitions from an excited state to a lower energy state. In this method, the photons are used to excite electrons in the so called photoelectric effect. The elemental composition of the material can be investigated by observing characteristic set of discrete wavelength that are emitted based on the element and the electron transitions. The photon's wavelengths are collected to create an output information in the form of an emission spectrum. The mechanism resulting in the emission at 1.5μm is shown in the Figure 24.
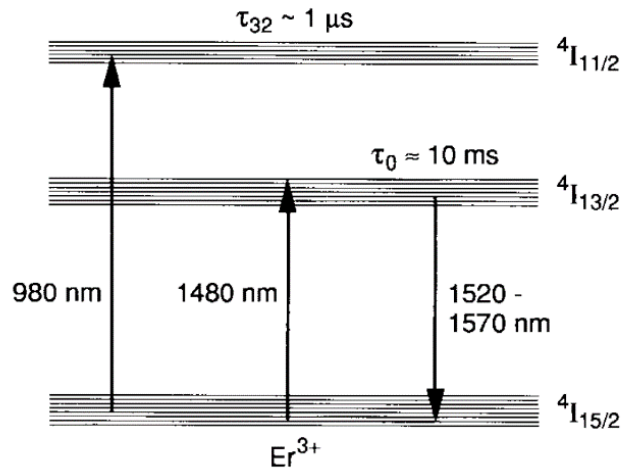

Figure 24.   Mechanism resulting in emission at 1.5μm

The upconversion is a process in which lower energy photons excite materials (possessing luminescent properties) in the visible spectral range and are later transformed into fewer, higher energy photons. This photons are then emitted as antistokes fluorescence in the near infrared (NIR) range. The possible energy levels and upconversion mechanism for Er^{3+} ions are presented in the Figure 4.

In RE doped materials, there are three main processes causing upconversion emission: excited state absorption (ESA), energy transfer upconversion (ETU), and photon avalanche (PA) processes. Schematics of all of these processes are shown in the Figure 25.
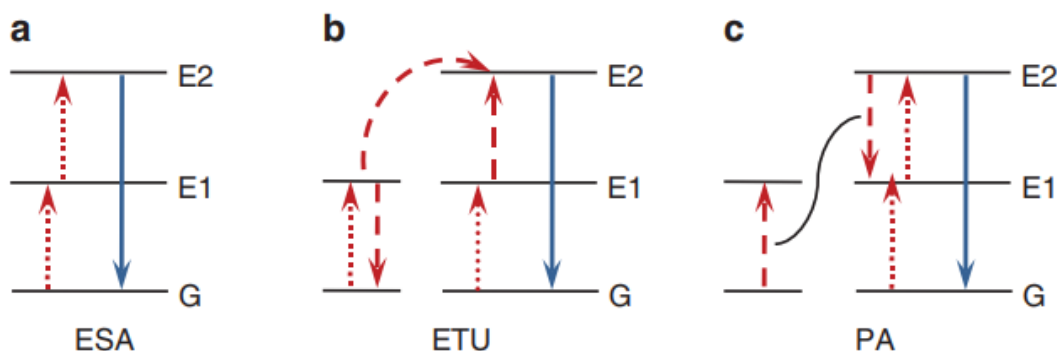
Figure 25.   Schematic presentation of the three main types of processes causing upconversion in rare earth doped materials: (a) excited state absorption; (b) energy transfer upconversion; (c) photon avalanche. Dotted lines - photon excitation, dashed lines - non-radiative energy transfer, full arrows - emission processes (Ac,10).

- When two photons are absorbed by a single ion, ESA upconversion can occur (Figure 25a). Firstly, the ion is in its ground state (G) when the absorption of the first photon causes the excitation to the metastable state (E1). Secondly, the second photon is absorbed from this level leading to the promotion of ion from E1 to higher energy level E2. Finally, the emission from E2 to G occurs. This upconversion process produces the weakest emission.

- In ETU process, two adjacent ions are excited by the absorption of a photon from G to E1 (Figure 25b). Next, the excited state energy from one ion is transferred to the second ion also in excited state E1. The donor ion relaxes to its ground state G while the ion accepting the energy transfer is promoted to the excited state E2. Finally, the emission from E2 to G occurs. This upconversion process is independent of pump power and occurs without delay after excitation.

- The PA process only occurs at a certain pump intensity (Figure 25c). Firstly, one ion is excited to E1 state through weak non-resonant absorption of photon. This happens when adjacent ion undergoes excited state absorption and it is excited to energy state E2. Further, the cross-relaxation energy transfer to an adjacent ion in its ground state results in both ions occupying E1. Finally, the resonant excited state absorption and the cross-relaxation energy transfers exponentially increase the population of E2 and therefore the upconversion emission intensity. Although, this process is the most efficient process, it depends on the pump power and has a slow (up to several seconds) response to excitation due to the number of ESA and cross relaxation processes (Ac,10).

The fluorescence lifetime is an average time that a molecule stays in its excited state before emitting a photon. The measurements of the lifetime were carried out using the same equipment used for upconversion analyses with additional Time-Correlated Single Photon Counting (TCSPC) unit to measure the time between excitation by a pulsed laser and the arrival of the emitted photon at the detector. For this purpose a photodiode and a single-photon sensitive detector are usually used, to provide a start and stop signal for measuring time delay. The measurement is repeated many times and mean value of lifetime is calculated by the system. The accuracy of the measurement was ±0.2 ms. This measurement was performed in at the Istituto Superiore Mario Boella (Italy) in collaboration with Dr. Nadia Boetti.

2.8.2 Eu^{2+} *luminescence properties*

The persistent luminescent (PeL) spectra were measured using a Varian Cary Eclipse Fluorescence Spectrophotometer coupled with a Hanamatsu R928 photomultiplier (PMT). The samples were irradiated using a UVGL-25 (4W, λ_{exc}=254 nm) lamp for 5 minutes. The measurement was taken 1 minute after ceasing the excitation.

The conventional luminescence spectra were measured using a spectrophotometer with a charge-coupled devices (CCDs) camera (Avantes, AvaSpec-2048x14) as a detector. The excitation source was a Nd:YAG pulse laser (λ_{exc}=266 nm, 8 ns, TII Lotis) with 50 ms integration time and 10 averaging. The luminescence properties of the glasses were measured at Turku University (Finland) in collaboration with Dr. Mika Lastusaari.

The luminescence spectra were measured using a spectrophotometer, the schematic of which can be found in the Figure 26.
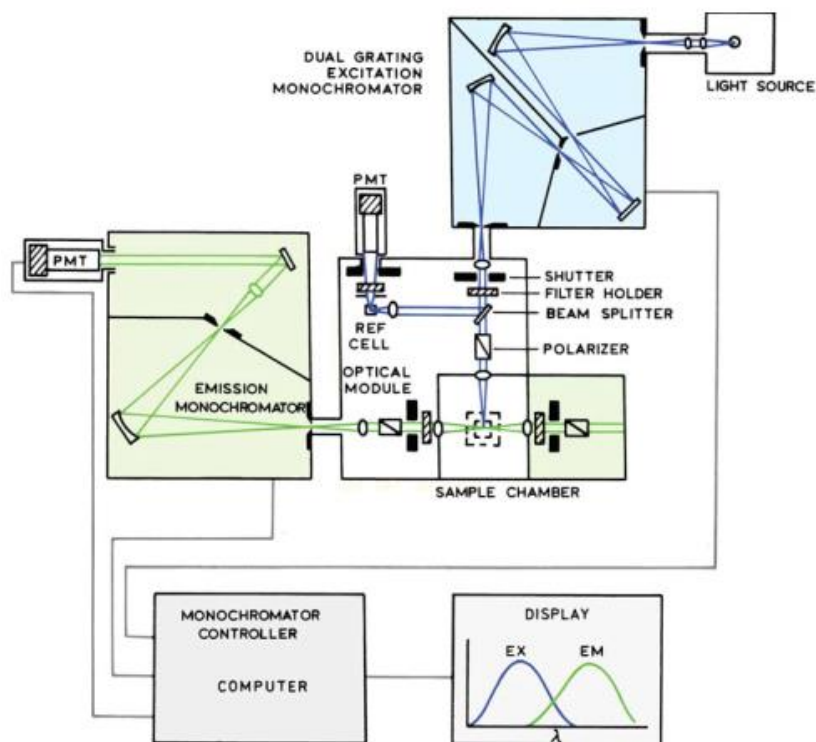
Figure 26.   Schematic of a spectrophotometer. Modified from (La,06)

Firstly, the source of light can be produced either using a lamp or a laser. If a lamp is chosen, the monochromator is used to remove the wavelengths different from the chosen one or the scattered light. Filters are also often needed, in addition of monochromators. Moreover, a beam splitter can also be provided in the excitation light path. This splitter reflects part of the excitation light to a reference cell, which generally contains a stable reference fluorophore. Secondly, the sample is excited with the light which leads to the transition of electrons to higher energy state. Subsequent, the transition of electrons back to the ground state results in the emission of a photon. Finally, the photons are detected, generally using photomultiplier tubes (PMT) and quantified with the appropriate electronic devices. Fluorescence spectral data are presented as emission spectra, a plot of the fluorescence intensity versus wavelength in nm (La,06).

2.9   Surface patterning

The surface patterning of the glasses was carried out at Technical University of Madrid (UPM), Spain, under the supervision of Prof. Carlos Angulo Barrios and with the assistance of Dr. Manuel Abuín. Patterning of the glasses was performed in a clean room (100-1000 class)

belonging to the Institute for Optoelectronic Systems and Microtechnology (ISOM-UPM). Initial experiments were carried out with fluorophosphate glasses with the composition (75 NaPO$_3$-25 CaF$_2$)$_{100-x-0.25}$-(TiO$_2$/ZnO/MgO)$_x$, doped with 0.25mol% Er$_2$O$_3$, with x=0 and x=1.5. However, these samples were very hygroscopic and their surface was seriously degraded (increased surface roughness) when exposed to air, preventing us from performing any patterning process on them. Therefore, patterning studies were achieved with more chemically stable phosphate glass samples.

Phosphate glasses with the composition 49.3P$_2$O$_5$-39.4 SrO-0.9Na$_2$O-1.5TiO$_2$ (in mol%) were prepared using standard melting processing by mixing powder chemicals and melting them for 5 minutes in air in platinum crucible. The chemicals were NaPO$_3$ (Alfa-Aesar, technical grade), CaF$_2$ (Honeywell-Fluka, 99%), SrO (Sigma-Aldrich, 99,9%) and TiO$_2$ (Sigma-Aldrich, 99,8%) in powder form. Finally, glasses were quenched and annealed for 5h at 200°C to release the stress from the quench. The glasses were doble-side polished and cut in order to produce samples 1.5cm x 1cm x 0.3cm in size.

The first step of the patterning process was spin-coating a photoresist layer onto the glass surface. Then, UV lithography was carried out to produce a micropattern in the photoresist film. Subsequently, a chromium layer was deposited using a thermal evaporation technique. The chromium/photoresist areas were then removed using a lift off procedure leaving only the patterned chromium mask on the glass surface. Next, the glass material was etched using Inductively Coupled Plasma (ICP) etching. Finally, we removed chromium by soaking the sample in slightly heated industrial chromium remover based on KOH. In the Figure 27 the whole surface patterning process is presented schematically.

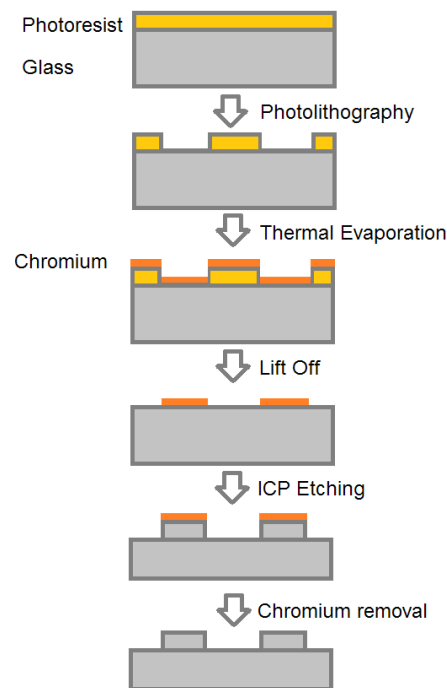A detailed description of each process step is presented as follows:

Figure 27.　　　　Schematic of all surface patterning processes

2.9.1　Sample cleaning

Before any process started the cleaning of the sample was carried out to remove any residues that could interfere with patterning process. For any micro and nano fabrication process the sample surface should be clean and homogenous. Firstly, the sample was put into a beaker with acetone (BASF Selectipur®) and then into an ultrasonic bath for 5 min. Secondly, the sample was put into a beaker with isopropanol (BASF Selectipur®) and for 3 minutes again into ultrasonic bath. Finally, the wet glass surface was treated with pressurized nitrogen air to detached any remaining dirt particles and dry the surface. After cleaning, the surface was checked under the optical microscope to confirm that there were no residues left.

2.9.2 Spin-coating

In this work, spin coater CONVAC 1001 was used at speed of 1000 rpm for 60 seconds to deposit the positive photoresist Poly(methyl methacrylate) PMMA AR-P 671.05 (ALLRESIST) on glass substrate. The glass sample was first attached to a plastic sample holder using sticky tape and then placed in the middle of the spinner. Few drops of resin were applied on the surface of the glass just so that they completely cover the sample without bubbles. After spin-coating process the sample was heated on a hot plate for one hour at 60°C. The final thickness of the resist film was 50 nm. The general steps of spin-coating are presented in the Figure 28.

Deposition   **Spinning**   **Drying**
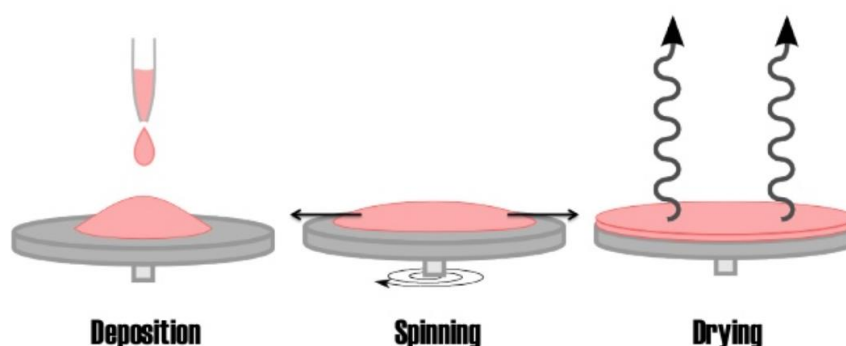
Figure 28.   Schematic of the spin coating process steps (Ar,19)

Spin coating technique is used for simple, low-cost deposition of 1–10 μm thickness uniform coatings (Sm,13). Coating solution is distributed onto the sample surface which is immobilized on the spinner often using vacuum (Bi,04). The solution is spread out uniformly at the surface due to the centrifugal force caused by fast spinning motion of the spinner (Zh,18). The thickness of the resist layer on the sample surface depends on rotation rate, the solution density and viscosity (Bi,04).

The films that can be deposited can be organic (e.g. polymers) and inorganic (e.g. chalcogenides). Generally, the solution is diluted in a solvent which is then partially removed during spinning and then partially during final baking at elevated temperature (Ng,12). There are two types of photoresists: positive and negative. Positive photoresist when exposed to UV light is becoming more soluble and can be later removed using developer. Negative photoresist acts in oppositive way and is becoming less soluble when exposed to UV light. The behaviour of different photoresists is presented in the Figure 29.
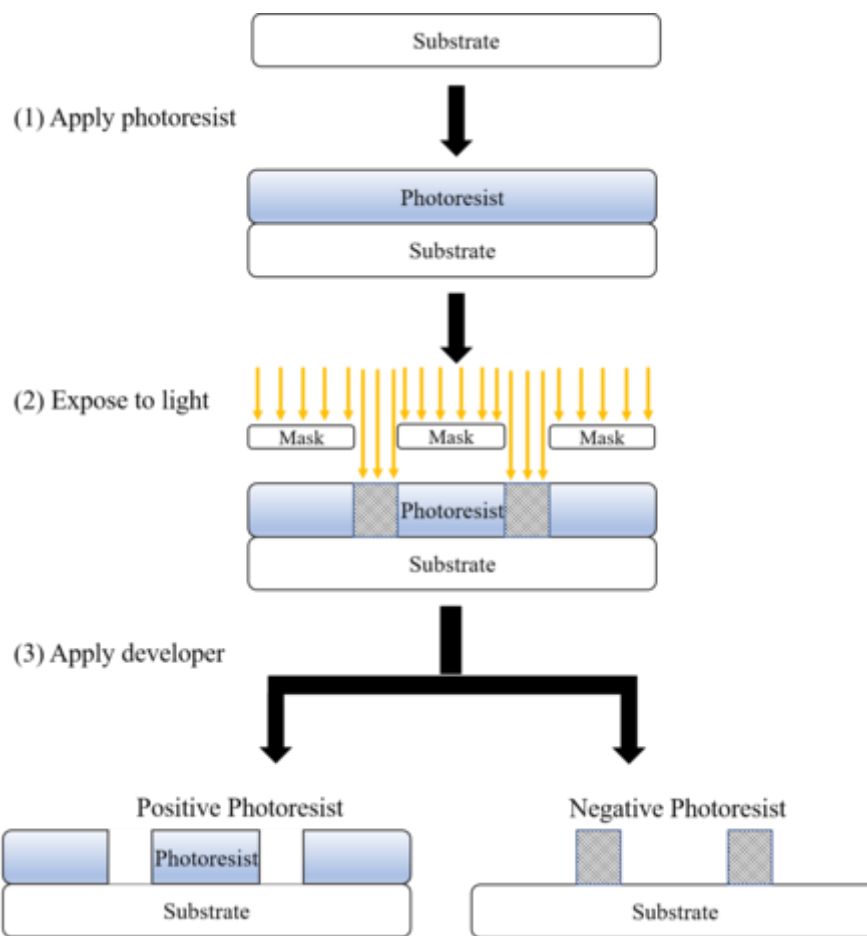
Figure 29.   Schematic showing difference between positive and negative photoresist (Ph,19)

2.9.3   Lithography

In this study, the MJB4 Mask Aligner from SUSS MicroTec has been used for creating a pattern in previously deposited positive photoresist. Optical lithography was carried out at room temperature, in soft-contact mode and using UV light. The used ADTEK photomask consists of 2D square gratings and 10 to 100 μm wide stripe patterns. Firstly, the mask is immobilized on the sample holder using vacuum. Next, the mask is aligned and focused so that the chosen pattern of different 2D square grating, from 2 to 6 μm side, are properly positioned onto the sample surface. The lithography was carried out in soft contact mode. Subsequent, exposure was carried out in two cycles, 500 seconds each. After removing the sample from the lithography machine, the pattern was developed for 2 min using AR 600-55 (ALLRESIST) developer. Finally, the sample was put into a beaker with isopropanol to stop the developer action. The pattern was checked under optical microscope and if it is not fully developed, the

sample is put back into the developer for an additional minute. If the exposure and developing time are appropriate, there should be no resist remaining in the UV-exposed regions.

Photolithography is a micro fabrication process used for creating micro and nano sized patterns in photoresist film. Pattern can be as small as few tens of nanometers. It is done by exposing photoresist to UV light through a mask and by that transferring the pattern on the photoresist. Electron beam or x-ray scan also be used and provide better resolution. Depending on the kind of the photoresist (positive or negative), places exposed to light are becoming less or more soluble. After UV exposure, the more soluble part of the photoresist is removed using a chemical solution called developer (Li,12; Ma,11).

Printing of the pattern can be done in three different exposure modes: contact printing, proximity printing and projection printing. In contact printing the sample is brought in physical contact with photo mask. Due to that high resolution is possible. The contact can be 'soft' and 'hard'. In soft contact mask is brought softly in contact with sample surface. In hard contact, the sample is pressed against the mask. The main disadvantage is that mask can be damaged easily, and debris between resist and mask can cause defects in the pattern. When proximity printing is used the photo mask is kept at some distance from the sample surface (10-25 µm). This mode is safer for the mask. In projection printing, pattern on the photo mask is projected to photoresist using for example lenses. Different exposure modes are presented in the Figure 30.
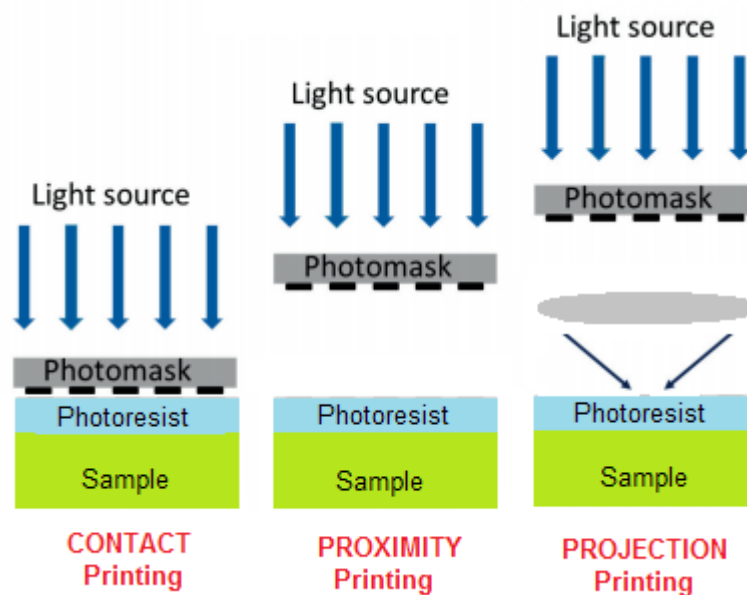

Figure 30.   Schematic showing different exposure modes in photolithography (Pu,17)

2.9.4 Thermal evaporation and Lift Off

In this work, thermal evaporation of chromium was carried out using Balzers BAE 250 Coating system. The process was carried out at T<70°C, rate of deposition 0.5nm/s, background pressure $P_{backgroud}$=7.4x10^{-7} mBar and pressure during process P=2.8x10^{-6} mBar. Around 100nm thick chromium film was deposited on the lithographied resist/glass sample. The role of the chromium layer is to act as a protecting mask for the underneath glass material during the glass etching step.

Thermal evaporation is one method out of few physical vapour deposition techniques. Firstly, the material to be deposited is heated up using either Joule effect (resistance heating) or bombardment with a high energy electron beam until evaporation. To heat up the metal crucible using Joule effect first the current has to be applied to it. Because of the Joule effect the current passing through conductor (metal crucible) produces heat which is causing evaporation of the metal inside of the crucible. In the e-beam evaporation the heating is caused by an electron beam focused on the material to be evaporated. This is a good option for high temperature melting materials. Vacuum allows metal atoms to travel in straight line from the source to the samples cold surface where they are deposited in the form of thin film. In the Figure 31 the general schematic of the thermal evaporation process is presented.
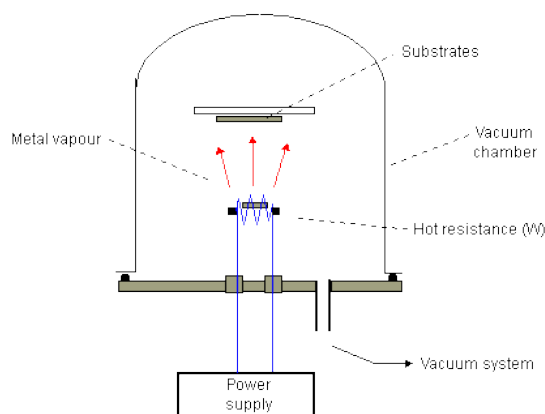

Figure 31.   Schematic presentation of thermal evaporation machine using Joules effect (Th,19)

Lift-off process was carried after thermal evaporation to remove the areas of pattern with photoresist and chromium. In this way only chromium pattern stayed on the glass sample surface. Lift off was carried out by immersing the sample in acetone at 40°C for 2 minutes.

2.9.5   *ICP etching and Chromium removal*

In this work, inductively coupled plasma (ICP) etching has been carried out using PlasmaPro NGP0 (Oxford Instruments) and LEP400 etch depth monitor at room temperature. The following ICP process parameters were employed: flow of CHF_3 = 40 sccm, flow of Ar = 4 sccm, RF=200 W, ICP=400 W, minimum DC Bias=30 V, pressure 5 mTorr, time t=5 min.

ICP is a plasma-based dry etching technique that works as follows. Firstly, time-varying high radio frequency (RF) electric current generates oscillating magnetic field when passing through a coil. Generated from a coil spark initiate ionization of the pure gas, usually argon, helium or nitrogen, and reactive gases such as CHF_3, into plasma. Cations and electron generated in magnetic field collide with gas atoms to further ionize it. Hot plasma reacts with surface molecules, dissociate them and etch the surface (In,19c)

ICP etching is commonly used for dry etching of semiconductors, dielectrics, metals, and polymers (In,19b). In particular, ICP etching of glass is typically carried out using SF_6, CF_4 and CHF_3 reactive gases with different combinations of O_2 and/or Ar.

After proper process parameter optimization, ICP etching can allow high etch rates, high etching selectivity and low damage processing (In,19a). Schematic of an ICP etcher is presented in the Figure 32.
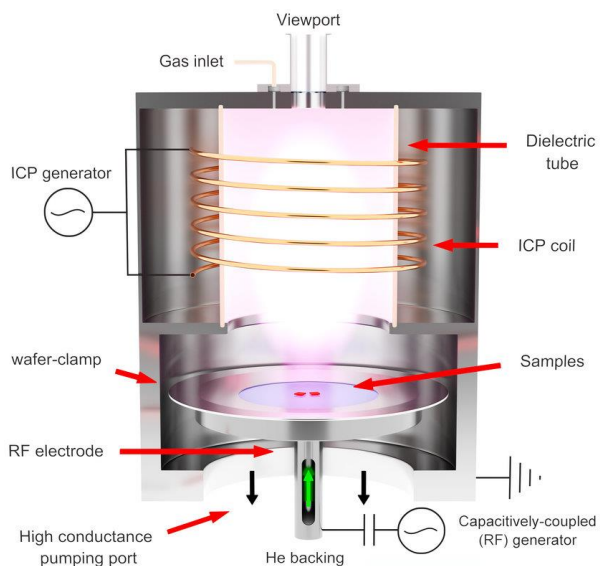

Figure 32.   Schematic presentation of ICP etcher (Hö,18)

Subsequent chromium removal was carried out using a commercial product to etch chromium. The etchant was first heated to 40°C and the sample was dipped in it for 20s. Then

after checking under the microscope than not all chromium was removed, the sample was kept for extra 15 seconds in the etchant for a complete Cr removal.

2.9.6 *Profilometer*

In this study, Alpha-Step IQ Surface Profilometer was used to measure sample surface profile at different stages of the microfabrication process. In this type of mechanical profilometer, topographical data is extracted by a diamond stylus physically touching the surface and moving laterally for a specified distance and with specified contact force. Height variations are measured as either the stylus or the sample is being moved and then converted to electrical signals. The signal, after being magnified by an electronic amplifier, is collected to generate the surface profile. This allows for surface topography analysis with sub-angstrom resolution. However, this technique is slower than non-contact methods and can be destructive to some surfaces (Zh,00). Schematic of a contact profilometer is presented in the Figure 33.
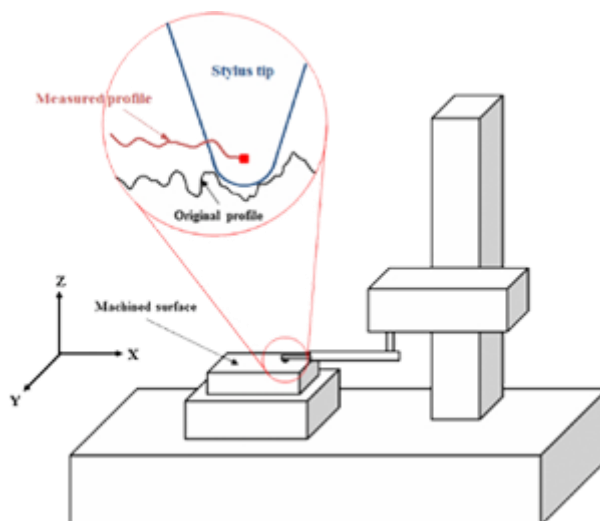

Figure 33.   Schematic presentation of contact profilometer (Op,19)

2.9.7 *Glass grating diffraction measurements*

Micropatterns created on the glass surfaces consisted of 2D gratings, which diffracted light. The phosphate glass is hydrophilic and hygroscopic, and by measuring the optical response of the glass grating when inmersed in water, the effect of the latter on the phosphate material integrity could be monitored. Optical characterization of a fabricated 2D phosphate glass grating immersed in deionized (DI) water was carried out using the setup shown in the

Figure 34. First, the glass grating sample was placed inside a cuvette filled with DI water, and then the cuvette was sealed to avoid liquid evaporation. A 635-nm-wavelength laser beam impinged normally the 2D grating and two photodetectors were collecting optical power values from zeroth and first diffracted orders, respectively. The incident laser beam was produced by a 10 mW laser diode. An iris diaphragm placed between the laser source and the glass grating was used to decrease the incident laser power down to 5.5 mW. In the zero-order mode (directly transmitted light) the laser beam was passing through an optical attenuator (neutral-density filter, transmittance = 0.1) and an iris diaphragm to reduce the power hitting the photodetector (otherwise, it could be damaged). In the first-order mode, laser beam was hitting the second photodetector without attenuation. Both photodetectors were connected to a power meter which in turn was connected to a computer for recording and processing the measured power data.
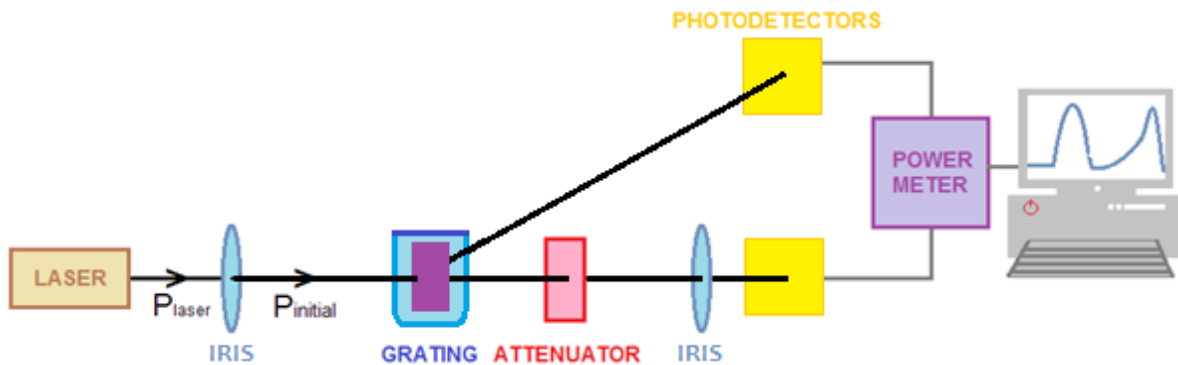

Figure 34.   Schematic presentation of set up for diffraction effieciency measurements

3 Results and discussion

3.1 Impact of the glass composition on various glass properties

The main challenge when investigating fluorophosphate glasses is the preparation of the glass as fluorine is well known to be volatile. Additionally, the quantification of fluorine within the glass is also difficult to perform. Therefore, the first part of this section is the investigation of different melting temperatures (and so different F content) on the spectroscopic properties of Er^{3+} of glasses to understand which impact the F has on various glass properties. Then the changes in the glass composition on the various properties of the glasses are discussed.

3.1.1 Impact of F concentration on various glass properties

To investigate the impact of F on the emission and upconversion properties of fluorophosphates glasses, Er^{3+} doped oxyfluorophosphate glasses were prepared using standard melting method using different melting temperatures (T_m). The increase of melting temperature is expected to lead to an increase in the fluorine evaporation and so to a reduction in the fluorine content in the glasses. Glasses were melted at 900, 950 and $1000^{\circ}C$.

The thermal properties of the as-prepared glasses are summarized in Table 3 along with the measured density. Also shown in the table is the quantification of CaF_2 performed by Bureau Veritas, a global leader in Testing, Inspection and Certification (TIC). The quantification was performed using an Electron Microprobe (EPMA).

Table 3. Physical and thermal properties of the glasses. Also included in the CaF_2 quantification using EPMA

T_m (°C)	CaF_2 content±0.1 (mol%)	$\rho \pm 0.02$ (g/cm³)	$T_g \pm 3$ (°C)	$T_x \pm 3$ (°C)	$T_p \pm 3$ (°C)	$\Delta T = T_x - T_g \pm 6$ (°C)
900	19.7	2.63	269	323	338	54
950	19.4	2.63	266	321	335	55
1000	18.7	2.64	277	332	346	55

An increase in the melting temperature leads to a decrease in the CaF_2 content as expected. It does not have a noticeable impact on the density and on the ΔT of the glasses which is a gauge of the glass resistance toward crystallization. The ΔT of the glasses is less than $100^{\circ}C$

indicating that the glasses of investigation are poor glass formers. However, one can notice some changes in the thermal properties depending on the melting temperature: an increase in the T_m to $1000°C$ leads to an increase of the glass transition temperature, T_g, of the onset of crystallization, T_x and of the maximum of the crystallization peak, T_p. The changes in the thermal properties induced by the increase in the melting temperature confirm that the glasses possess different fluorine content. As it is well know that fluorine reduces T_g, T_x and other thermal properties (Cu,16; No,18), a lower concentration of F is expected in the glass melted at $1000°C$. Additionally, the change in T_x with increasing temperature is a clear indication that the crystallization process will be different depending on the T_m and so on the F content.

It should be pointed out that the thermal properties of glasses are higher compared to the same glass composition prepared with 0.15 mol% of Er_2O_3, presented in (No,18). This is due to the larger amount of Er_2O_3 in the investigated glasses.

The IR spectra of the glasses, normalized to the main band at $\sim1130 cm^{-1}$, are presented in Figure 35.

The spectra exhibit bands at 720, 890, 1125 and 1260 cm^{-1}. Multiple shoulders in the range are also present. The bands at ~700, 880, 1160 and 1280 cm^{-1} are due to $\nu_{ss}(POP)$, $\nu_{as}(POP)$, $\nu_{ss}(PO_2^-)$ and $\nu_{as}(PO_2^-)$ fundamental vibrations of Q^2 units respectively (Ko,10). The various bands between 930 and 1010 cm^{-1} are often related to rings-type formation in the glass network (Wi,84). The shoulders at ~980 and 1085 cm^{-1} are due to symmetric and asymmetric stretching vibrations of the PO_3^{2-} in Q^1 units respectively.
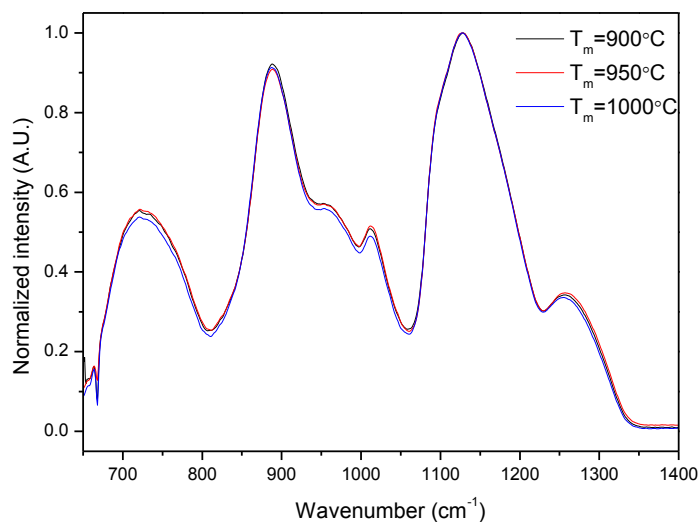
Figure 35.   Normalized IR Spectra of the investigated glasses

Besides, the band at 1085 cm^{-1} can be attributed to an overlap between PO_3^{2-} of Q^1 units and PO_2^- of Q^2 groups in metaphosphate (Il,01). Finally, the shoulder at 1010 cm^{-1} might be related to $\nu_{as}(PO_3F)$ bond vibration according to (Mu,63). The shoulder at 1160 cm^{-1} and the absorption band at 1250 cm^{-1} correspond to the symmetric and asymmetric vibrations of PO_2 in Q^2 units, respectively (Me,97). There is no bands at higher wavenumber than 1300 cm^{-1}, indicating that there is no Q^3 groups in the investigated glasses. These IR spectra clearly indicate the presence of a metaphosphate structure. It is clearly shown that there is no noticeable change in the IR spectra caused by the increase in the T_m confirming that it is difficult to track losses in fluorine occurring during the glass preparation using the FTIR spectroscopy.

Figure 36 presents the absorption spectra for the as prepared glasses.
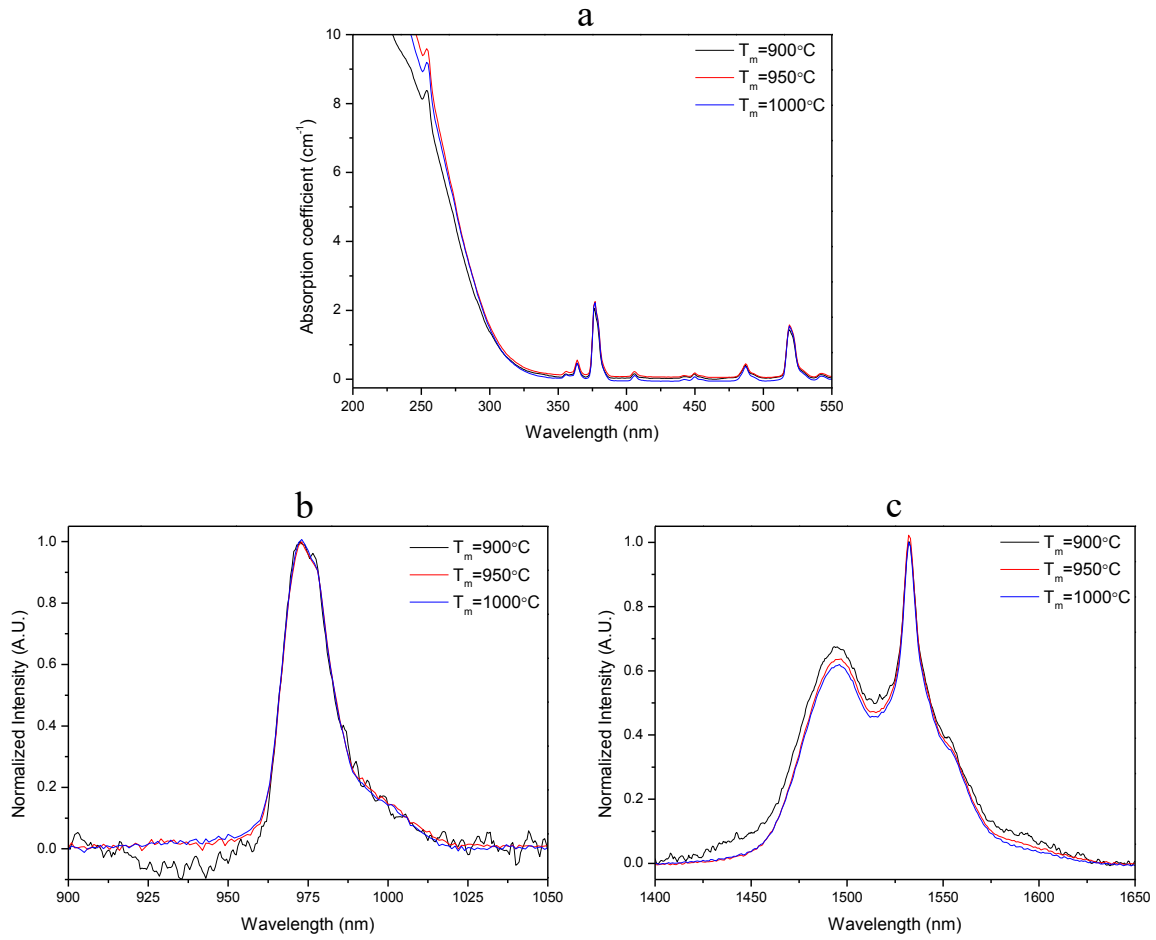

Figure 36.   Absorption spectra a) and normalized absorption band at 975nm b) and at 1500nm c) of the investigated glasses

The absorption spectra exhibit several bands, which are characteristics of the Er^{3+} ion 4f-4f transition from the ground state to various excited levels of Er^{3+} ions (Ba,94). There is no noticeable shift of the absorption edge induced by the increase in T_m. As seen in Figure 35b and c, an increase in T_m has also no noticeable impact of the shape of the absorption band at 980 and 1530 nm indicating that the sites of Er^{3+} ions are not strongly affected by the T_m change.

From the absorption spectra, the absorption cross-section at 980 and 1530nm were calculated from the absorption coefficient using Equation 10 and are presented in the Table 4.

Table 4.   Absorption coefficient and absorption cross section values

T_m (°C)	Er^{3+} ions/cm³ $(10^{19}) \pm 5\%$	σ_{Abs} at 975 nm (cm^{-1})	σ_{Abs} at 975nm $(10^{-21} cm^2) \pm 10\%$	σ_{Abs} at 1530 nm (cm^{-1})	σ_{Abs} at 1530nm $(10^{-21} cm^2) \pm 10\%$
900	8.19	0.16	2.01	0.52	6.32
950	8.19	0.18	2.19	0.52	6.40
1000	8.22	0.19	2.29	0.56	6.85

Within the error of the measurement, the increase in T_m has no significant impact on the absorption cross-section at 980 and 1530 μm indicating that the sites of Er^{3+} ions are not strongly affected by the T_m change.

The emission spectra of the glasses were measured using 976 nm pumping and are presented in Figure 37.
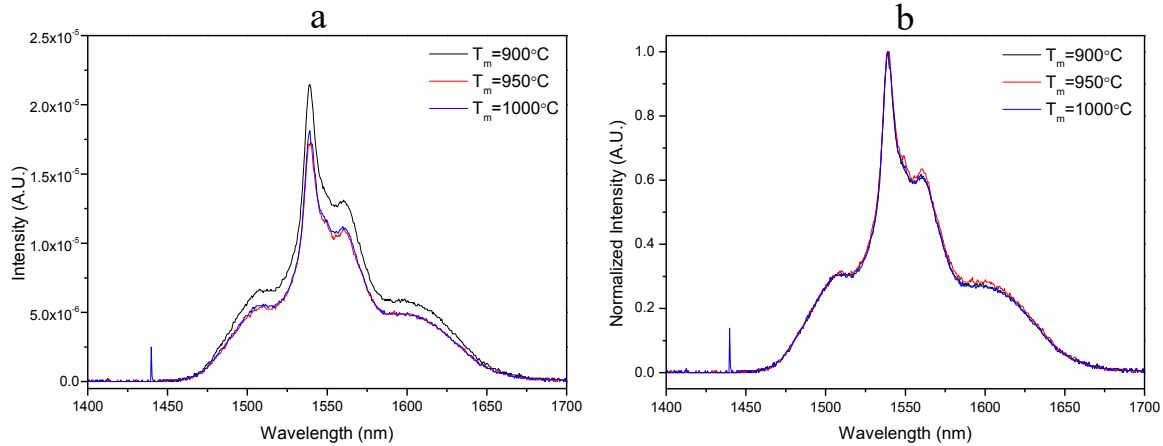

Figure 37.   Emission a) and normalized emission b) spectra of the investigated glasses measured using 976 nm pumping

The spectra of the glasses exhibit a broad emission band at 1.5 μm, which is typical of the Er^{3+} emission $(^4I_{13/2} \rightarrow {}^4I_{15/2})$ (Ob,98). The glass with lowest $T_{m=}900$°C shows the highest intensity. An increase in T_m leads to a small decrease in the intensity of the emission. No significant change in the shape of the emission band can be seen with changing T_m, confirming that the site of Er^{3+} ions is not influenced by the changes in the F doping (Figure 37b)

The lifetime values of $Er^{3+}:^4I_{13/2}$ level in investigated glasses are reported in Table 5.

Table 5.   Lifetime values of Er^{3+}:$^4I_{13/2}$ level of the investigated glasses

T_m (°C)	Lifetime ± 0.2 (ms)
	no HT
900	8.2
950	8.5
1000	8.5

Within the accuracy of measurement, an increase in T_m has no noticeable impact on the the lifetime values of Er^{3+}:$^4I_{13/2}$ level. One can notice that the lifetimes are larger than those reported in (No,18) and also than those of tellurite glass (3.3 ms) (Di,01), bismuth based glass (1.8 ms) (Di,01) and borosilicate glass (2.0 ms) (Li,14).

According to (No,18), we expect the glasses with high content of F to exhibit an upconversion with high intensity due to the decrease in the phonon energy. However, as the glasses were crushed into powder for the measurement, it is not accurate to compare the intensity of the upconversion of the glasses. The normalized upconversion spectra presented in the Figure 38 were obtained using 975 nm pumping.
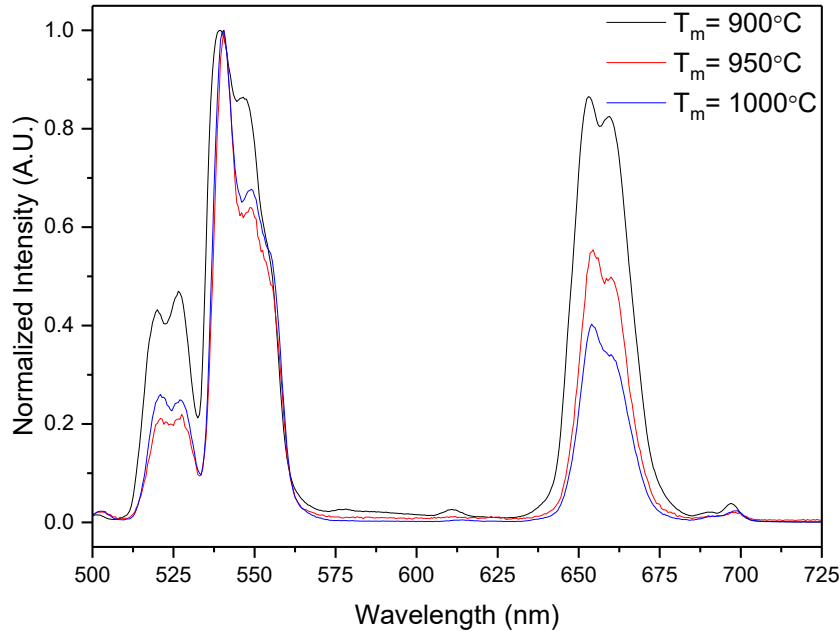
Figure 38. Normalized upconversion spectra of the investigated glasses. Spectra were obtained using λ_{exc}=975nm

All the spectra exhibit green and red emissions, which correspond to $^2H_{11/2}$, $^4S_{3/2} \rightarrow {}^4I_{15/2}$ and $^4F_{9/2} \rightarrow {}^4I_{15/2}$ transitions of Er^{3+} respectively (Pa,07). For all glasses, the green emission is more significant than the red emission. A decrease in the intensity of the red emission as compared to the green one can be seen when T_m increases. This could be explained as an effect of a cooperative up-conversion process between Er^{3+} ions that is favored by the lower phonon energy (Di,01). A possible energy transfer mechanism for red emission centered at 662 nm is that one ion decays from the metastable level $^4S_{3/2}$ state ($^4S_{3/2} \rightarrow {}^4F_{9/2}$) and the second is excited to the $^4F_{9/2}$ state ($^4I_{9/2} \rightarrow {}^4F_{9/2}$) (Pa,07). Changes in the shape of the green emission are also visible. This band is due to a hypersensitive transition, the intensity of which is known to strongly depend on the environment of Er^{3+} ions (Li,15). Therefore, from the changes in the shape and position of this band, the site of the Er^{3+} ions is suspected to be slightly modified when T_m increases.

In summary, losses in F occurring during the glass melting process can lead to small changes in the thermal properties and also in the spectroscopic properties of the glasses. It is therefore crucial to prepare fluorphosphate glasses using the same melting process (duration of the melting) to control the evaporation of F.

3.1.2 *Impact of the glass composition on the various glass properties*

Glasses with the composition $(75 \text{ NaPO}_3\text{-}25 \text{ CaF}_2)_{100\text{-}x\text{-}0.25}\text{-}(\text{TiO}_2/\text{ZnO}/\text{MgO})_x$ (in mol%) were prepared with 0.25mol% Er_2O_3, with x=0 and x=1.5 (labeled as Ti, Zn and Mg). The glass with x=0 is the glass melted at 900°C from the previous section. This glass is now labeled as Ref. The thermal properties of the prepared glasses are summarized in Table 6 along with the measured density and the quantification of CaF_2.

Table 6. Density and thermal properties of the investigated glasses. Also included is the CaF_2 quantification using EPMA

Glass label	CaF$_2$ Content (mol%) ±0.1mol%	T$_m$ (°C)	ρ ± 0.02 (g/cm³)	T$_g$ ± 3 (°C)	T$_x$ ± 3 (°C)	T$_p$ ± 3 (°C)	ΔT ± 6 (°C)
Ref	19.7	900	2.63	269	323	338	54
Zn	19	1000	2.65	276	334	350	58
Ti	18.8	1025	2.65	286	350	370	64
Mg	20.4	900	2.66	279	345	365	66

The changes in the glass composition leads to a slight increase in the density, T_g, T_x, T_p and ΔT, the addition of TiO_2 being the most effective in these changes. The increase in T_g may be related to the different CaF_2 content but may also indicate that the changes in the glass composition increase the strength of the network and the bond strength. Although ΔT increases after adding Ti, Zn or Mg, it still remains lower than 100°C.

The IR spectra of the glasses are presented in Figure 39. They are normalized to the main band at ~1130cm^{-1} . Consequently, the intensity changes are expressed relatively to the main band. According to (Cu,16; No,18), these IR spectra clearly indicate the presence of a metaphosphate structure.
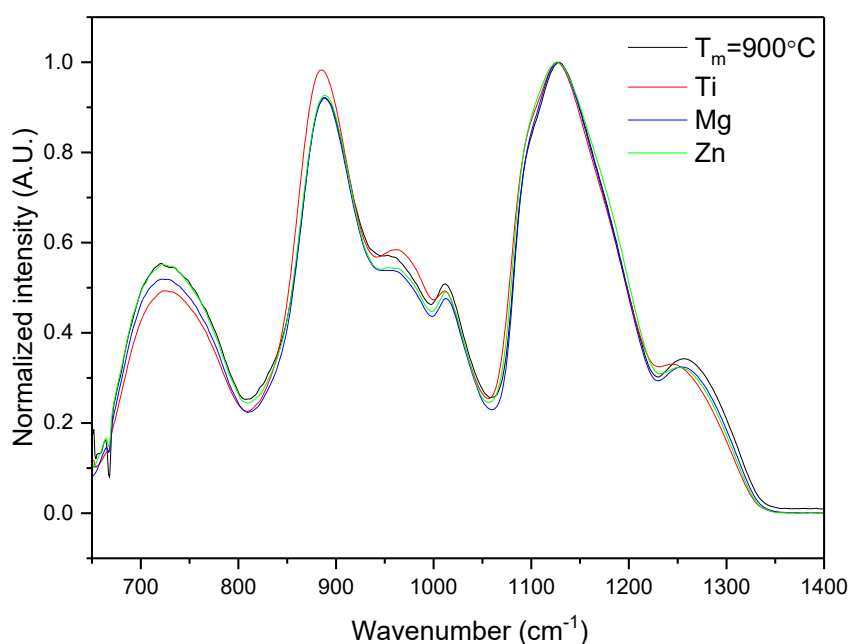
Figure 39.   Normalized IR spectra of the investigated glasses

The spectra are similar to those presented in Figure 27. The addition of ZnO and MgO leads to similar changes: a decrease in intensity of the bands at 700, 950, 1000 and 1250 cm^{-1} as compared to the main band. These changes can be related to a decrease in the Q^2 units. Therefore, Zn and Mg seem to act as a modifier, leading to a depolymerization of the phosphate network and to a less cross-linked network. The addition of TiO$_2$ decreases the intensity of the bands at 700, 1000 and 1250cm^{-1} while it increases the intensity of the bands at 900 and 950 cm^{-1}. The increase in intensity of the shoulder at ~980 may be related to the decrease of bridging oxygens due to formation of P-O-Ti bonds (Ki,12). This change in the IR spectra indicates that the glass network consists of Q^2 tetrahendra arranged in chain and ring formation, the amount of which increases at the expense of Q^1 units, with addition of TiO$_2$. Moreover, the addition of TiO$_2$ shifts the band of Q^2 at 1250 cm^{-1} towards smaller wavenumber. This may indicate changes in the strength of the chemical bonds in glass network. It has been shown that addition of TiO$_2$ leads to creation of 3D networks of P-O-Ti linkages causing distortion of the glass network and consequently increasing T$_g$ (Se,10).

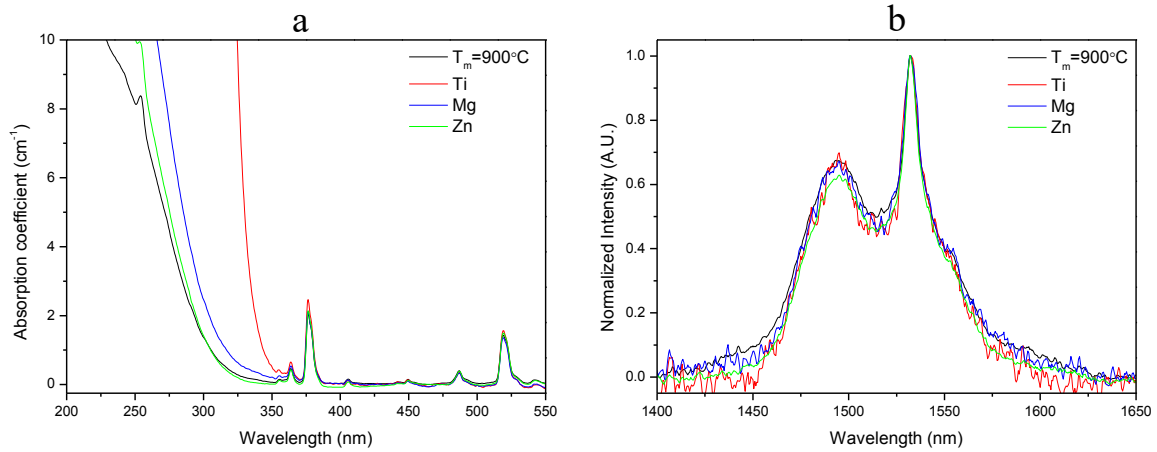The absorption spectra of the glasses are shown in the Figure 40.

Figure 40. Absorption spectra of the investigated glasses a) and normalized absorption band at 1500nm b)

The addition of TiO$_2$ leads to a shift of the band gap to longer wavelength most probably due to the presence of Ti^{3+} according to (Zi,69). The change in the position of the band gap can also be related to the formation of Ti-O-P bonds. The addition of MgO leads to a shift to longer wavelengths while having the largest amount of CaF$_2$. The addition of ZnO has no significant impact on the position of the band gap as shown in the Figure 40a.

As seen in Figure 40b, the shape of the absorption band is similar for all glasses. The site of the Er^{3+} ions is suspected not to be strongly impacted by the changes in the glass composition. Consequently, Ti, Mg and Zn are not suspected to participate to the second coordination shell around Er^{3+} (Lo,17).

The absorption coefficient and absorption cross-section are listed in the Table 7.

Table 7. Absorption coefficient and absorption cross section values.

Glass label	Er^{3+} ions/cm^3 (10^{19}) ± 5%	Abs. Coeff. at 975 nm (cm^{-1})	σ_{Abs} at 975nm (10^{-21} cm^2) ± 10%	Abs. Coeff. at 1530 nm (cm^{-1})	σ_{Abs} at 1530nm (10^{-21} cm^2) ± 10%
Ref	8.19	0.16	2.01	0.52	6.32
Zn	8.27	0.18	2.16	0.53	6.41
Ti	8.27	0.19	2.34	0.52	6.23
Mg	8.35	0.15	1.82	0.47	5.61

Within the accuracy of the measurement, the changes in the glass composition has no impact on the absorption cross-section at around 980 and 1500 nm.

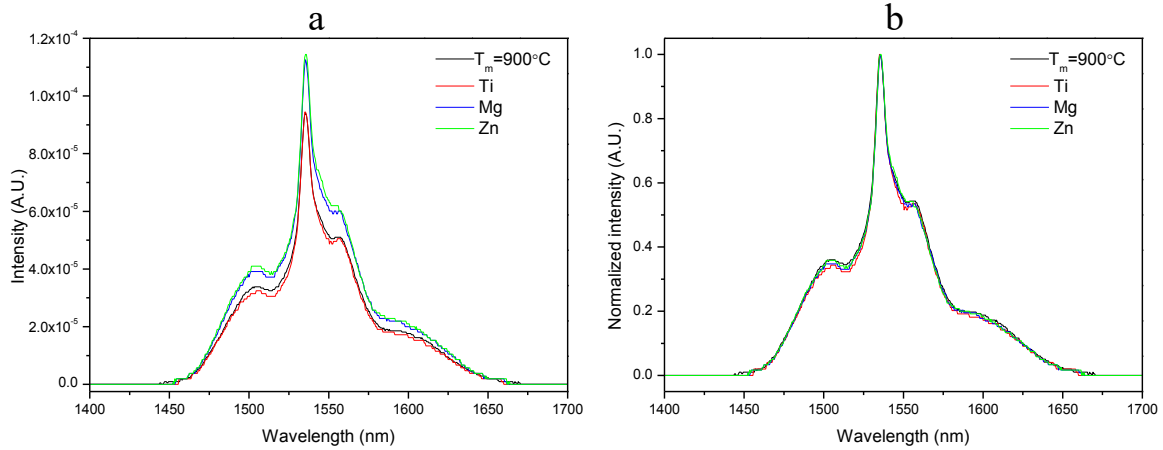The emission spectra of the glasses were measured using 976 nm pumping and are presented in Figure 41.

Figure 41.   Emission a) and normalized emission b) spectra of the investigated glasses. Spectra were obtained using λ_{exc}=975nm

The spectra exhibit a broad band which corresponds to the Er^{3+} emission ($^4I_{13/2} \rightarrow {}^4I_{15/2}$) in glasses (Ob,98). Whereas the addition of ZnO and MgO does not impact the intensity of the emission at 1550nm, the addition of TiO_2, slightly decreases the intensity of the emission at 1550nm. This is most probably related with decrease of solubility of Er^{3+} ions associated with a reduction of Er-Er distance due to the formation of the P-O-Ti bonds as reported in (Lo,17). As seen in Figure 41b, the shape of emission spectra is unaffected by doping with different elements confirming that Ti, Mg and Zn have no impact on the site of the Er^{3+} ions.

The lifetime values of Er^{3+}:$^4I_{13/2}$ level are presented in the Table 8.

Table 8.   Lifetime values.

Glass label	Lifetime ± 0.2 (ms)
Ref	8.5
Zn	8.3
Ti	8.4
Mg	8.2

Within the accuracy of the measurement, the change in the glass composition has no impact on the lifetime value. The lifetime in the Mg glass is probably lower than that of the Ref probably due to its largest amount of CaF_2.

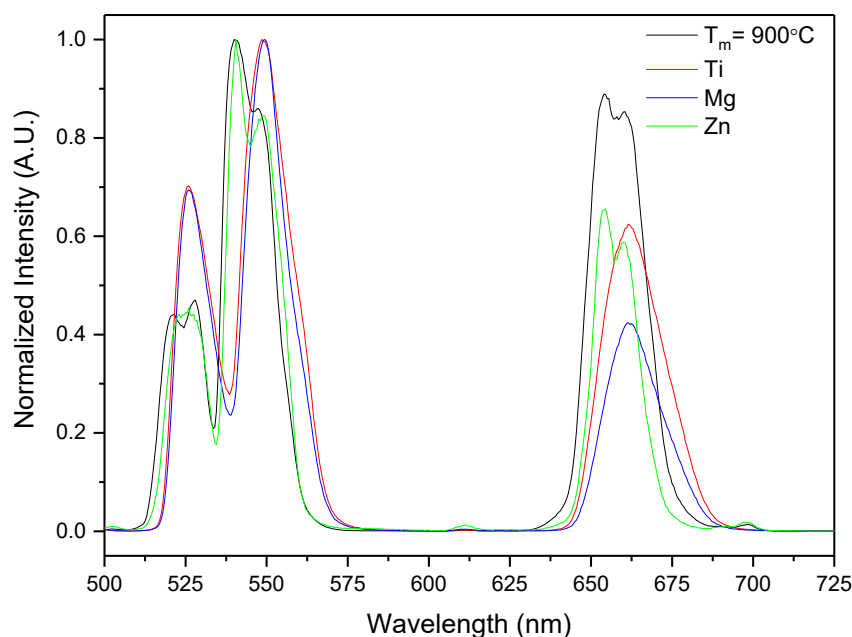The up conversion spectra presented in the Figure 42 were obtained using 975 nm pumping.

Figure 42.   Normalized upconversion spectra of the investigated glasses. Spectra were obtained using λ_{exc}=975nm

All the spectra exhibit similar green and red emissions seen in Figure 38. The changes in the glass composition decreases the red emission as compared to the green one. However, one can notice that the shape of the upconversion from the Ti and Mg-containing glasses is unusual, most probably due to the low intensity of the upconversion from the glasses. Therefore, the measurement should be repeated before bringing any conclusion.

In summary, when added in 1.5mol%, the addition of Ti, Zn and Mg leads to small changes in the physical, thermal, optical and spectroscopic properties of the glasses.

3.2 Er^{3+} doped glass-ceramics

3.2.1 Impact of F concentration on the nucleation and growth mechanisms

The glasses melted at 900, 950 and 1000°C were heat treated for 17h at T$_g$ + 20°C and then at T$_p$ for 1,3 or 6 hours. The picture of the glasses prior to and after heat treatment are presented in the Figure 43.
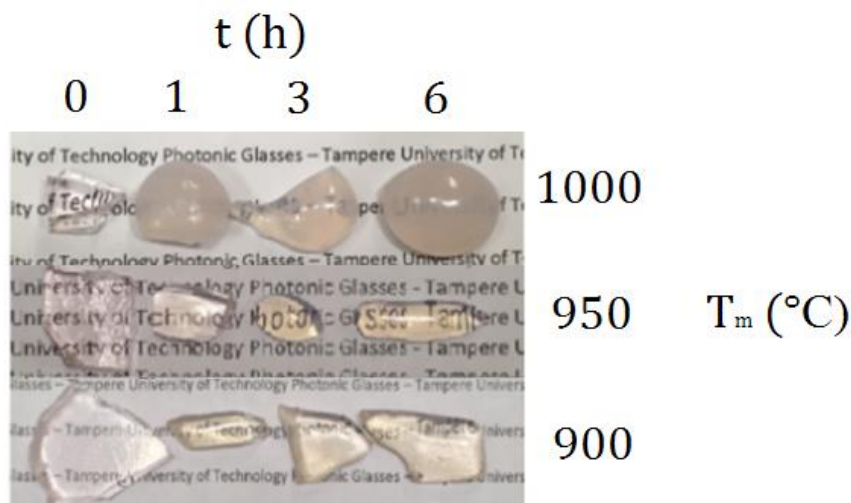

Figure 43.   Picture of the as prepared glasses prior to and after 1, 3 and 6h of heat treatment

After heat treatment, the glasses became milky. As reported in (No, 18), bulk crystallization occurs during the heat treatment. An increase in the T$_m$ increases the tendency of the glass to crystallization as only the glass melted at 1000°C becomes opaque after heat treatment. According to (Cu,16), an increase in F content is suspected to reduce the crystallization tendency of the glasses. Therefore, from the changes in the transparency of the glasses after heat treatment, we confirm that an increase in T$_m$, which leads to losses in F content, leads also to changes in the crystallization tendency of the glasses as suspected from the changes in the thermal properties of the glasses (Table 3).

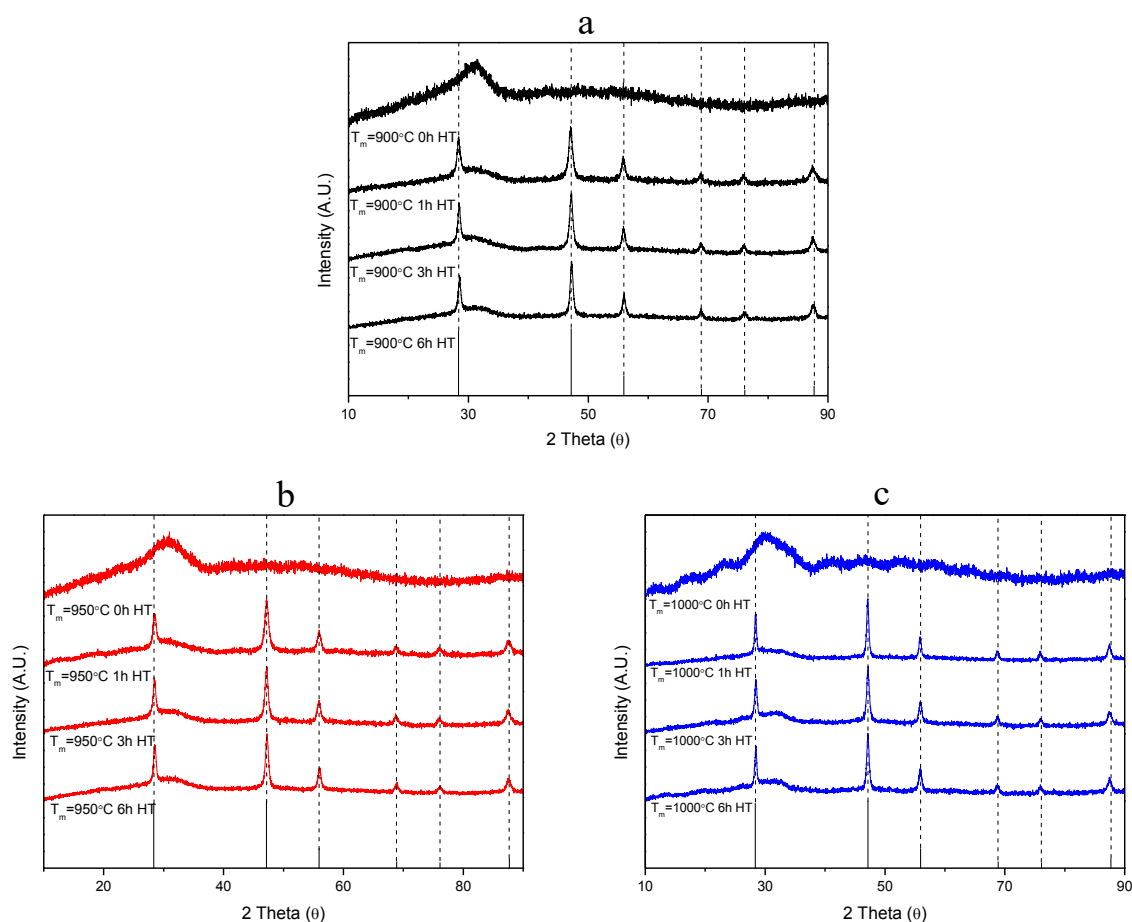The XRD patterns of heat treated glasses are presented in the Figure 44.

Figure 44.   XRD of as prepared glasses after 3h of heat treatment, showing CaF_2 crystals precipitation

Independently of the T_m, the spectra show sharp peaks which correspond to the precipitation of CaF_2 (ICDD PDF #00-035-0816). CaF_2 starts to be visible after 1h of heat treatment. Similar crystals were found to precipitate in this glass system (No,18). Although some glasses after heat treatment are transparent (Figure 43), CaF_2 crystals were detected clearly showing that it is possible to prepare transparent glass-ceramics from the investigated glasses.

The transmittance spectra of the glasses are presented in Figure 45.
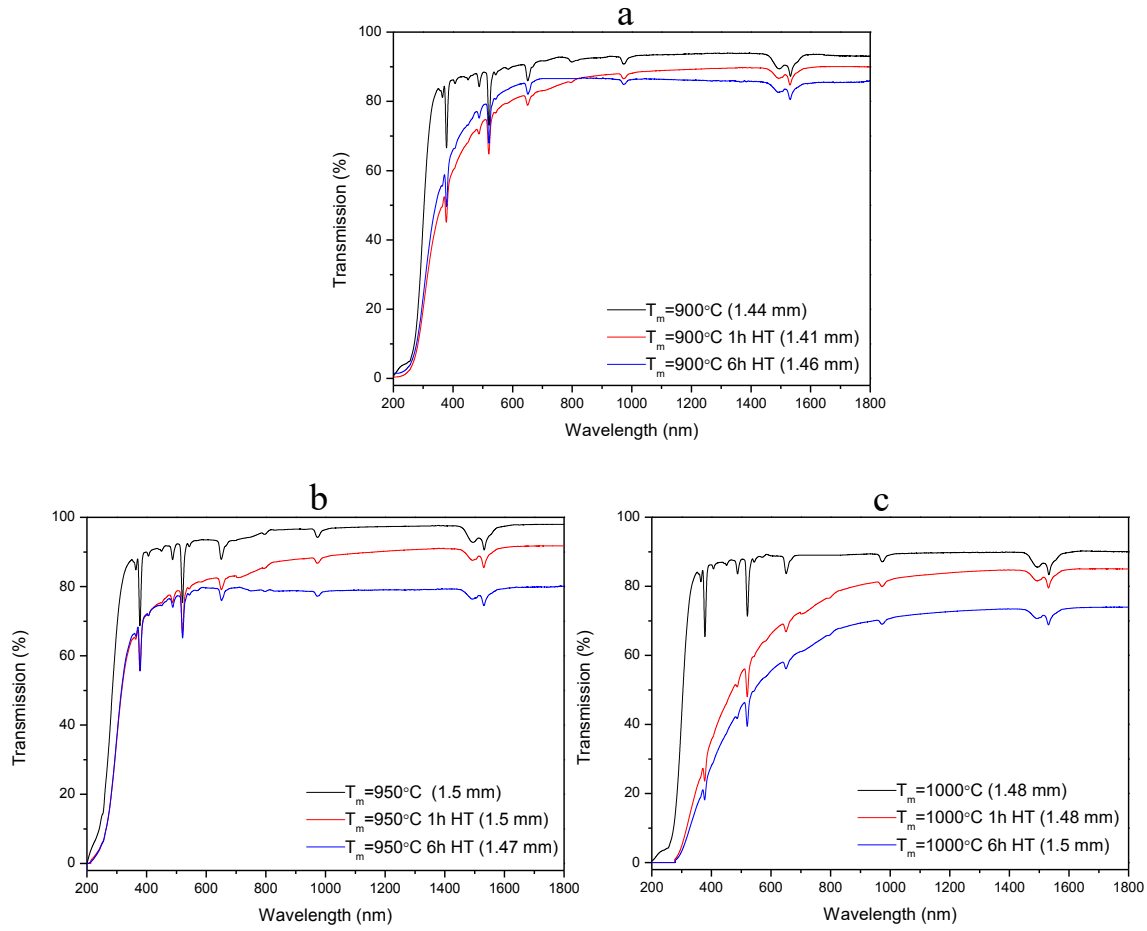
Figure 45.　　　Transmission spectra of T_m=900°C glass a), T_m=950°C glass b) and T_m=1000°C glass c) prior to and after heat treatment

After heat treatment, the transmission decreases confirming that glass's crystallization increases with increasing heat treatment time. This results are in agreement with the picture of the glasses after heat treatment presented in the Figure 43.

The emission spectra of the heat treated glasses, measured using 976 nm pumping, are presented in Figure 46.
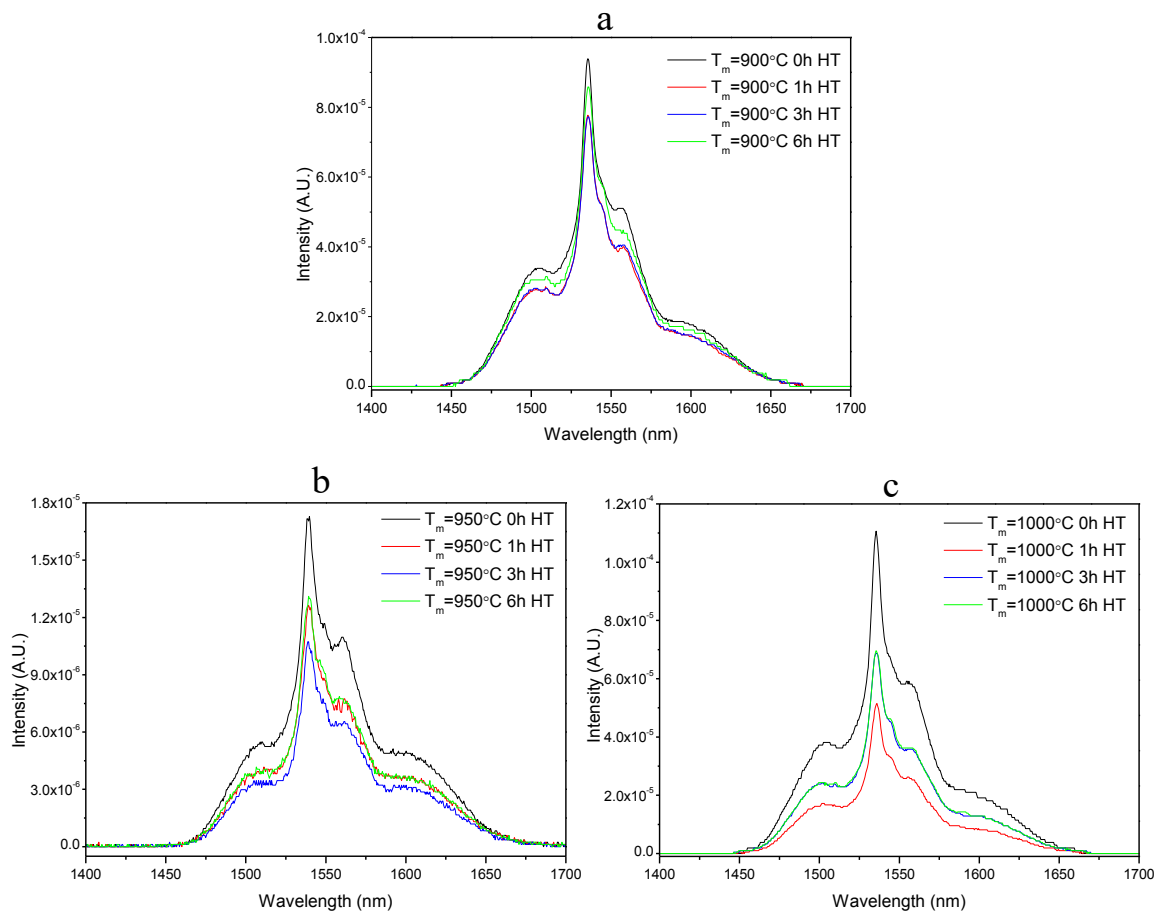
Figure 46. Emission spectra of $T_m=900°C$ glass a), $T_m=950°C$ glass b) and $T_m=1000°C$ glass c) prior to and after heat treatment. Spectra were obtained using $\lambda_{exc}=975nm$

No significant change in the shape of the emission band after heat treatment was observed indicating that the site of Er^{3+} ions is not influenced by the heat treatment and that some Er^{3+} remain the glass network. This is in agreement with (No,18). However, the intensity of the emission is reduced after the heat treatment indicating that the CaF_2 crystals contain some Er^{3+} ions. The reduction in the emission intensity is the most visible in the glass melted at 1000°C.

The lifetime values of $Er^{3+}:^4I_{13/2}$ level for all the glass and glass-ceramic are presented in the Table 9.

60

Table 9. Excited state $^4I_{13/2}$ lifetime values of the glasses prior to and after heat treatment at $(T_g + 20°C)$ for 17h and then for 15, 30 and 60min at T_p. Measurements were performed using laser excitation at 976 nm.

T_m (°C)	Lifetime ± 0.2 (ms)			
	no HT	1h	3h	6h
900	8.2	8.9	8.9	8.8
950	8.5	9.6	9.3	9.4
1000	8.5	8.6	8.8	9

Within the accuracy of the measurement, the heat treatment for 1h at T_p increases the lifetime value for the glasses with $T_m=900°C$ and $T_m=950°C$. However, the lifetime remains almost constant when the glasses are heat treated for longer times at T_p. The lifetime of the glass with $T_m=1000°C$ increases from 1h to 6h of heat treatment. The increase in the lifetime confirms the that the CaF_2 crystals are doped with Er^{3+}.

The upconversion spectra presented in the Figure 47 were obtained using 975 nm pumping.
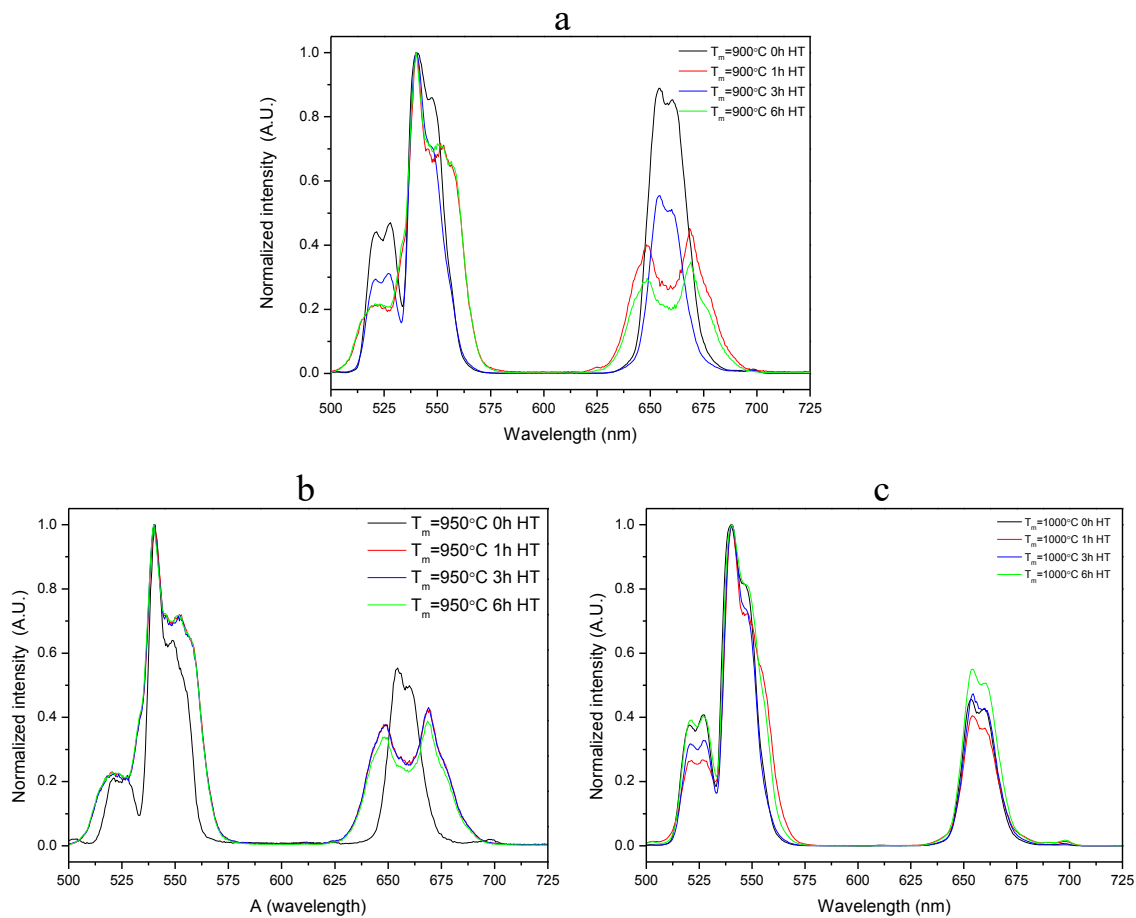
Figure 47.   Normalized upconversion spectra of the $T_m=900°C$ glass a), $T_m=950°C$ glass b) and $T_m=1000°C$ glass c) prior to and after heat treatment. Spectra were obtained using $\lambda_{exc}=975nm$

All the spectra exhibit the same green and red emissions seen in Figure 38. For all glasses, the green emission is more significant than the red emission. A decrease in the intensity of the red emission as compared to the green one can be seen after heat treatment time in the glasses prepared using $T_m= 900°C$ and $T_m=950°C$. The intensity of red emission in the glass with $T_m=1000°C$ first decreases after 1h of HT and then increases after 3 and 6h of HT. It is possible that the distances between pairs of Er^{3+} ions increase after heat treatment reducing the probability of energy transfer between Er^{3+} ions and thus reducing the intensity of the upconversion as seen in (Li,14). Changes in the shape of the band at 550 nm can be seen after heat treatment. As explained in the previous paragraph, this band can be associated to a hypersensitive transition and therefore, from the changes in the shape and position of this band, the site of the Er^{3+} ions is suspected to be modified after heat treatment.

As discussed in the previous section, the shape of some upcconversion spectra is weird most probably due to the low intensity of the visible. New measurement should be performed to confirm the data.

In summary, the increase in T_m (and so a decrease in the CaF_2 content) increases the crystallization tendency of the glass. The heat treatment, independently of T_m, leads to bulk crystallization of CaF_2 crystals which are thought to contain Er^{3+} ions.

3.2.2 Glass-ceramic from heat treatment

Glasses with the composition $(75NaPO_3-25CaF_2)_{100-x-0.25}-(TiO_2/ZnO/MgO)_x$ (in mol%) were heat treated for 17h at $T_g + 20°C$ and then at T_p for 1,3 or 6h . The reference glass is the glass melted at $900°C$. The pictures of the glasses prior to and after heat treatment are presented in the Figure 48.
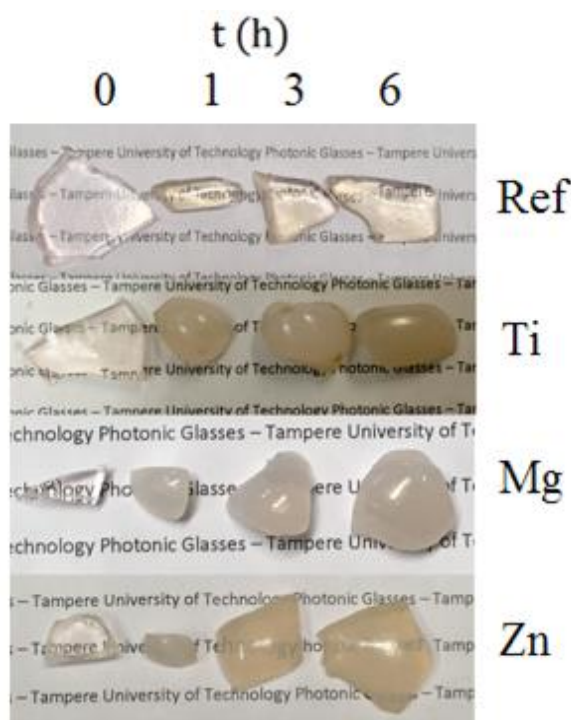

Figure 48.   Picture of the as-prepared glasses prior to and after 17h at $T_g + 20°C$ and then at T_p for 1,3 or 6 hours.

From the changes in the transparency of the glasses after heat treatment, the heat treatment leads to bulk crystallization of the glasses. Moreover, one can notice that the changes in the glass composition increases the tendency of the glass to crystallization, the Zn glass being the least prone to crystallization as compared to Ti and Mg glasses. This difference can be

related to Zn ions acting as modifiers which leads to depolymerization of the network (Lo,17). This in turn reduces the amount of nucleation sites and therefore decreases the crystallization tendency of the glass.

The XRD of heat treated glasses are presented in the Figure 49.
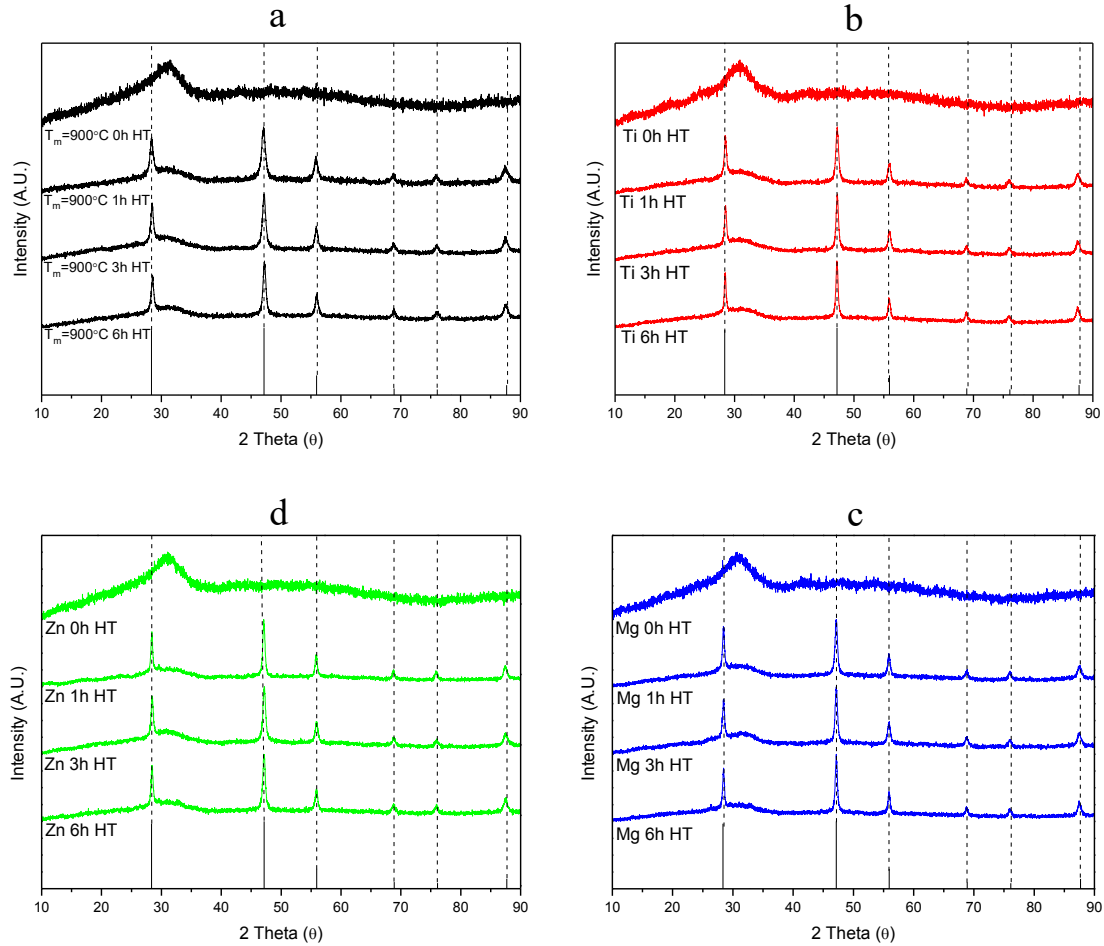

Figure 49.   XRD patterns of the Ref a), Ti glass b), Mg glass c) and Zn glass d) prior to and after heat treatment.

The presence of only one broad band in the XRD pattern for all as-prepared glasses confirm that the glasses are amorphous prior to the heat treatment. The XRD patterns for all heat treated glasses show sharp peaks which correspond to the precipitation of CaF_2 (ICDD PDF #00-035-0816) indicating that the change in the glass composition has no impact on the crystal phase precipitating in the glass.

To check if the Er^{3+} ions are incorporated into crystals, the emission spectra were measured using λ_{exc}=975nm. The emission spectra were obtained using λ_{exc}=975nm and are shown in the Figure 50.
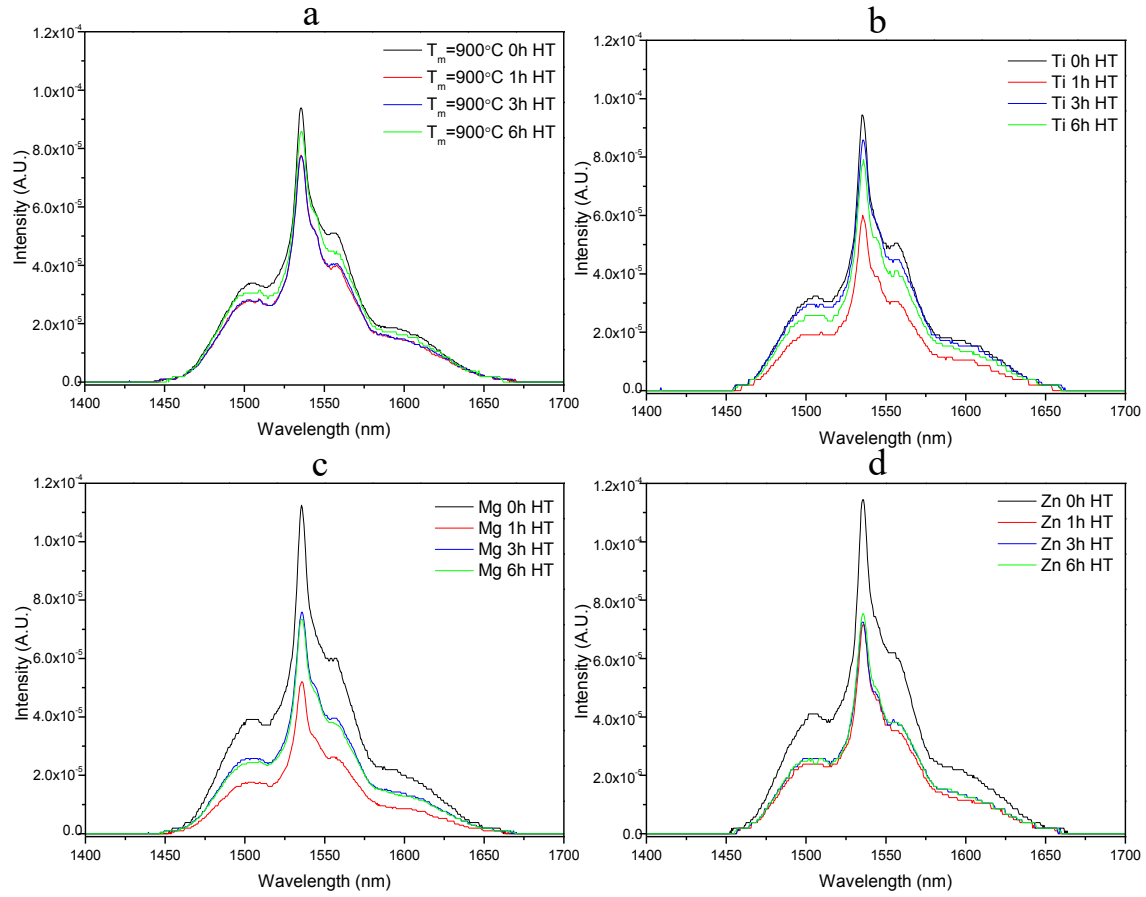
Figure 50.   Emission spectra of the Ref a), Ti glass b), Mg glass c) and Zn glass d) prior to and after heat treatment. Spectra were obtained using λ_{exc}=975nm

As seen for the reference glass, a decrease in intensity of the emission at 1.5µm can be seen after heat treatment indicating that the CaF_2 precipitating in all the glasses contain Er^{3+} ions. A stronger reduction in intensity can be noticed after 1h of heat treatment especially for Ti and Mg containing glasses (Figure 50b and c). As illustrated in Figure 51, the shape of the emission band does not change upon heat treatment indicating that some of the Er^{3+} remain also in the glasses.
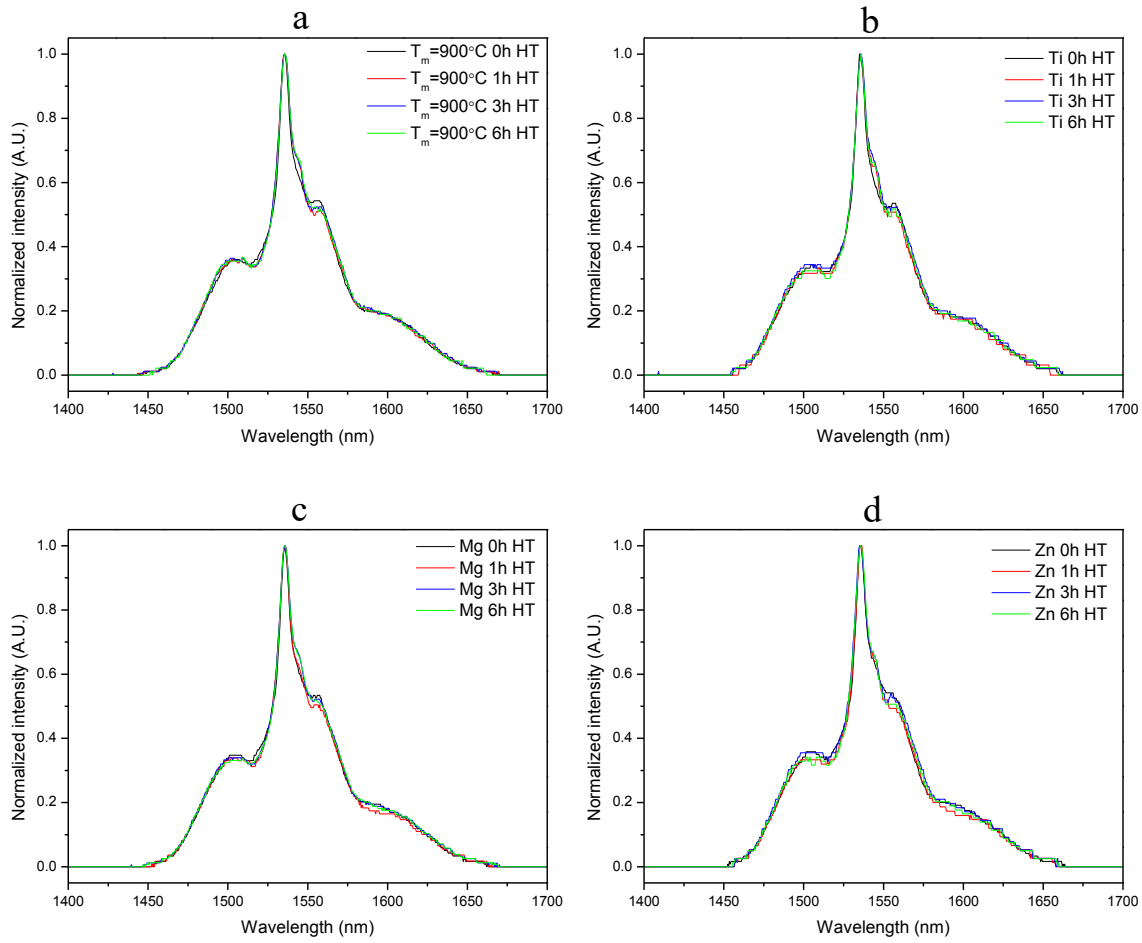
Figure 51.   Normalized emission spectra of the Ref a), Ti glass b), Mg glass c) and Zn glass d) prior to and after heat treatment. Spectra were obtained using λexc=975nm

The lifetime values of Er^{3+}:$^4I_{13/2}$ level for all the glass and glass-ceramic are presented in the Table 10.

Table 10. Excited state $^4I_{13/2}$ lifetime values of the glasses prior to and after heat treatment at (T_g + 20°C) for 17h and then for 15, 30 and 60min at T_P. Measurements were performed using laser excitation at 976 nm.

Lifetime ± 0.2 (ms)				
Glass label	**no HT**	**1h**	**3h**	**6h**
Ref	8.2	8.9	8.9	8.8
Ti	8.4	8.7	8.6	8.9
Mg	8.2	8.7	8.6	8.7
Zn	8.3	8.6	8.8	8.7

Within the accuracy of the measurement, the heat treatment for 1h at T_p increases the lifetime value for all the glasses. However, the lifetime remains almost constant when the glasses are heat treated for longer times at T_p.

As the shape of the emission band remains similar after the heat treatment, it is possible to think that the Er^{3+} ions remain in the amorphous part of the glass-ceramic. The small reduction in the intensity of the emission at 1.5µm after heat treatment of the glass-ceramic could be then due to changes in the Er-Er distance after heat treatment and also of the Er^{3+} being incorporated in the CaF_2 crystals. The small increase in the emission intensity when the heat treatment is longer than 1 hour is not fully understood and needs further investigation.

The normalized upconversion spectra presented in the Figure 52 were obtained using 975 nm pumping.
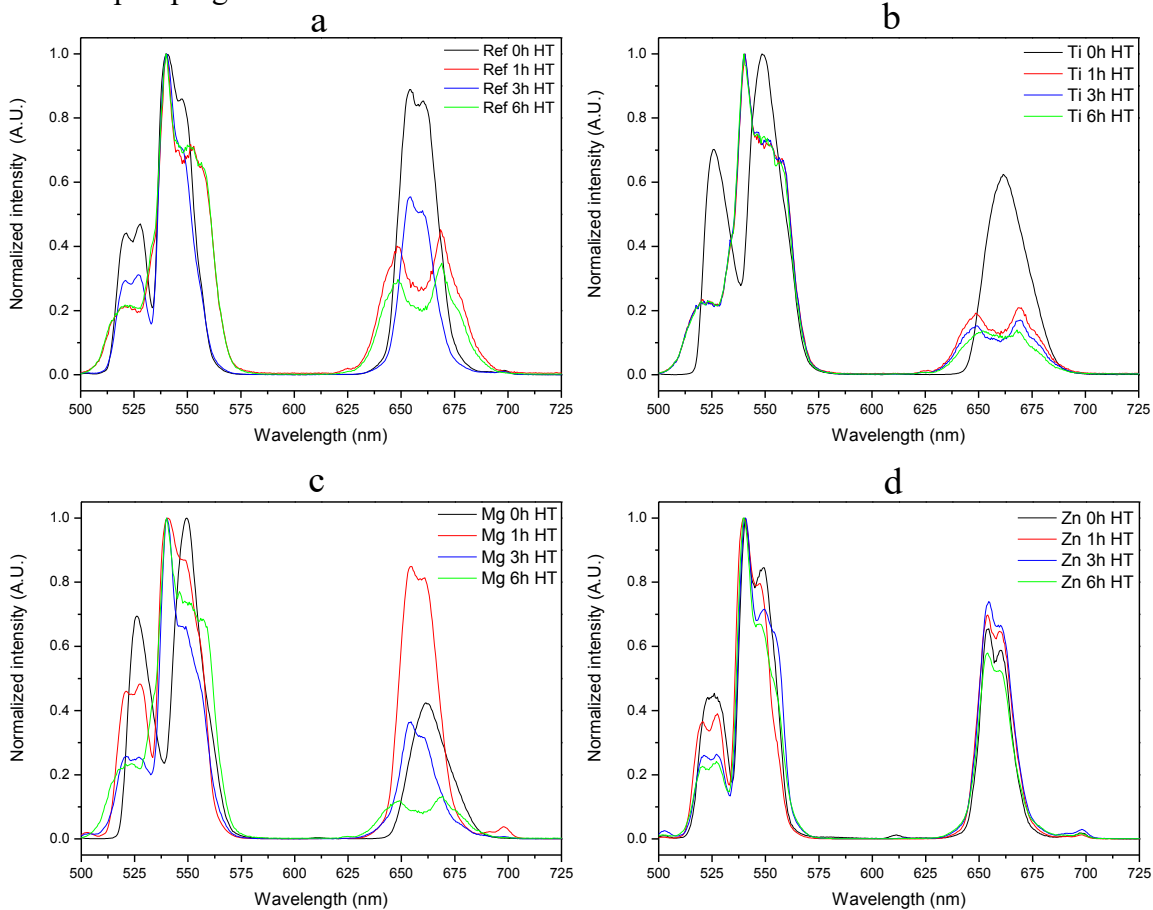

Figure 52.   Normalized upconversion spectra of the Ref a), Ti glass b), Mg glass c), and Zn glass d) prior to and after heat treatment. Spectra were obtained using λexc=975nm

As shown in Figure 46, the heat treatment also reduces the intensity of the red emission compared to the green. It is possible that the distances between pairs of Er^{3+} ions increase after

heat treatment reducing the probability of energy transfer between Er^{3+} ions and thus reducing the intensity of the upconversion as seen in (Li,14). From the changes in the shape and position of this band, the site of the Er^{3+} ions is suspected to be modified after heat treatment.

In summary, although the addition of Ti, Zn and Mg leads to small changes in the physical, thermal, optical and spectroscopic properties of the glasses, the same bulk crystallization of CaF_2 occurs in these glasses upon heat treatment. From the spectroscopic properties of the glass-ceramics, the CaF_2 are suspected to be doped with Er^{3+}. The change of the glass composition can be used to control the speed of the crystallization process.

3.3 PeL glass-ceramic using direct particles doping method

PeL glasses were prepared by adding persistent luminescent microparticles (MPs) $SrAl_2O_4:Eu^{2+},Dy^{3+}$ (Realglow®) in powder form in the melt of the glass with the composition (75 $NaPO_3$-25 CaF_2) (in mol%). Firstly, the glasses were melted for 5 min at 925°C. The particles were added at different temperatures (T_{doping}). x min after adding the particles (dwell time), the glasses were cast and annealed at 200°C for 4h.

3.3.1 Optimizing of the direct doping process

The glasses were prepared by adding 0.5wgt% of the MPs. The T_{doping} was 875 and 900°C and the dwell time 3 and 5 min. The pictures of the as prepared glasses are presented in the Figure 53.
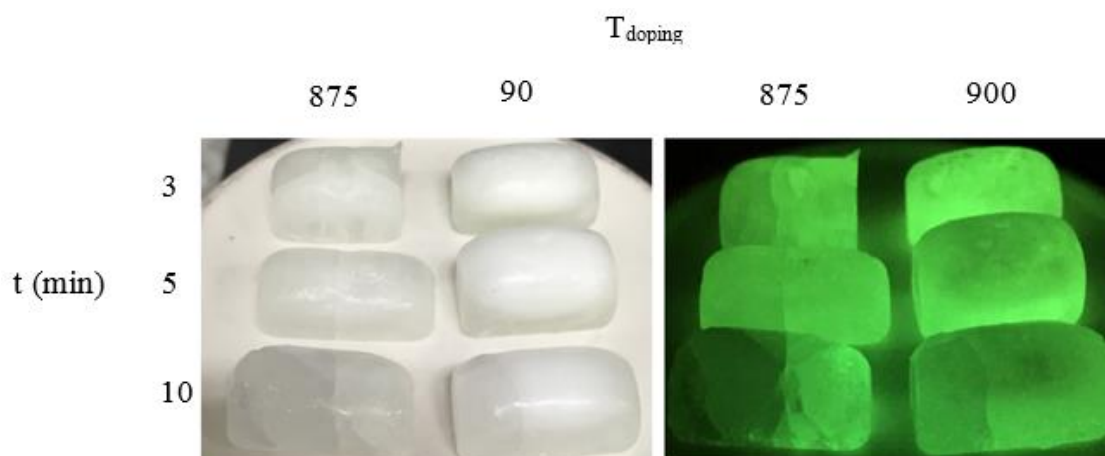

Figure 53.   Picture of the glasses in day light and after stopping the UV irradiation (afterglow)

All the glasses are crystallized after adding the particles which is in agreement with the low ΔT of the base-glass (see section 4.1). The glasses are bad glass formers and so crystallize when adding the MPs at the T_{doping}.

After stopping the UV irradiation, all the glasses exhibit green persistent luminescence, which confirms the survival of the MPs in the glasses. The PeL is more uniform when the glasses are prepared using a 900°C T_{doping} than when using a 875°C T_{doping}. The viscosity of the glass melt at 875°C is probably too high for a homogeneous dispersion of the MPs.

The persistent luminescence (PeL) spectra of the glasses are shown in Figure 54.
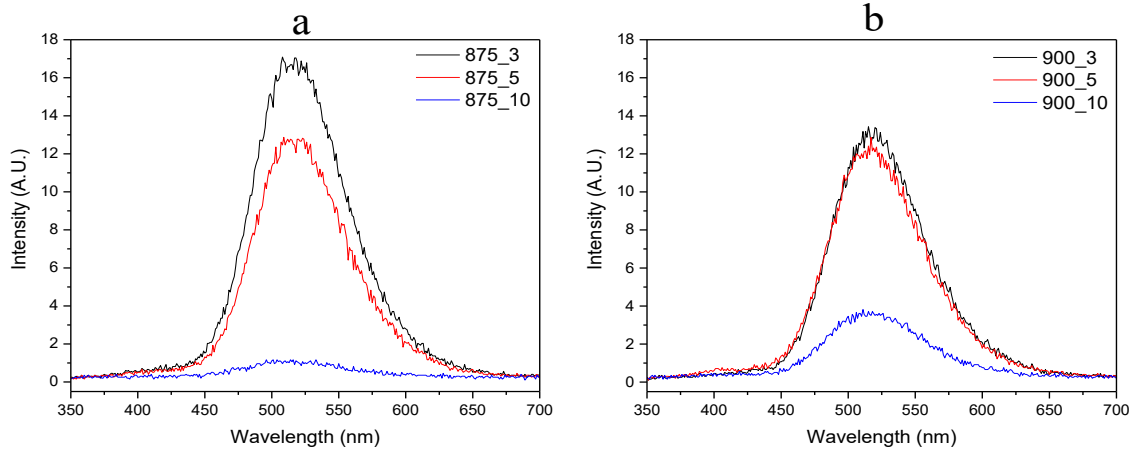

Figure 54.   Persistent Luminescence spectra of T_{doping}=875°C glass a) and T_{doping}=900°C glass b) with different dwell times

The PeL spectra of the glasses exhibit a broad band with a maximum at 520 nm which is attributed to the $4f^65d^1 \rightarrow 4f^7$ transition in Eu^{2+} located in one site in the monoclinic $SrAl_2O_4$ structure (Ai,04). As suspected from the Figure 53, an increase in T_{doping} and dwell time decreases the intensity of the emission band at 520 nm. In agreement with (Ma,96; Oj,18b; Oj,18c), an increase in the T_{doping} and dwell time is expected to lead to the decomposition of the MPs, which is associated with the loss in the PeL.

The normalized persistent luminescence (PeL) spectra of the glasses are shown in Figure 55.
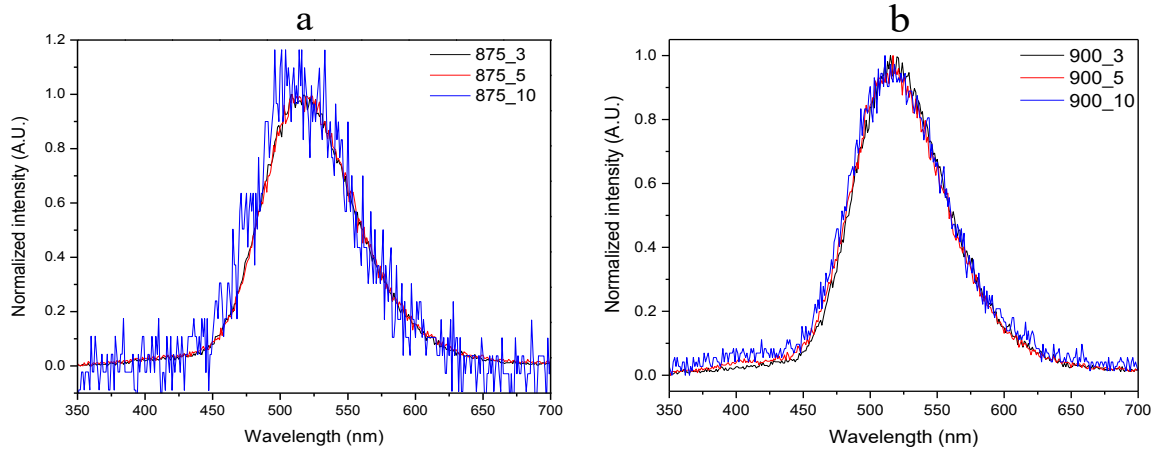
Figure 55.   Normalized Persistent Luminescence spectra of T_{doping}=875°C glass a) and T_{doping}=900°C glass b) with different dwell times

The shape of emission band is not changing indicating that the site of the Eu^{2+} ions is not modified when the MPs are embedded in the glass indicating that the decomposition of the MPs is congruent.

The normalized conventional luminescence (PL) spectra of the glasses are shown in Figure 56.
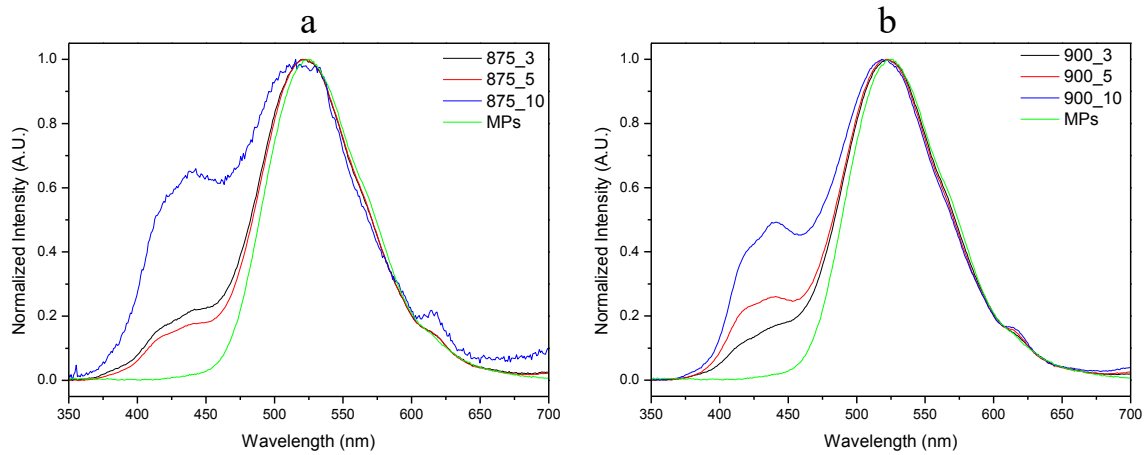
Figure 56.   Normalized conventional luminescence spectra of T_{doping}=875°C glass a) and T_{doping}=900°C glass b) with different dwell times

The PL spectra of the glasses exhibit a band at ~425 and ~525 nm which can be associated to the $4f^6 5d^1 \rightarrow 4f^7$ emission from Eu^{2+} located in two different cation sites in the $SrAl_2O_4$ structure (Ai,04). One should point out that the PL spectrum of the MPs alone exhibits

only the emission band at 525nm. An increase in the dwell time increases the intensity of emission band at 425 nm compared to the main band indicating that the site of Eu^{2+} is modified after embedding the MPs in the glass. The spectra exhibit also emission band at located ~ 615 nm which can be related to the emission from Eu^{3+} ions indicating that oxidation of Eu^{2+} into Eu^{3+} occurs during the glass preparation in agreement with (Ma,16). An increase in the dwell time increases the intensity of the Eu^{3+} emission.

From the PeL and PL spectra, the MPs are expected to decompose in the glass with the diffusion of Eu^{2+}. Some of the Eu^{2+} are suspected to be oxidized to Eu^{3+}. The decomposition already occurs when the glass is prepared using a T_{doping} of 875°C and a dwell time of 3 min. The decomposition is increased when the T_{doping} and dwell time increase.

In order to confirm the survival of the MPs in the glasses, SEM coupled with EDS was used to image the morphology and to analyze the composition of the MPs. The SEM images and EDS line profiles showing the elemental distribution across the MPs diameter and interface with the 875_3, 900_3, 875_10 and 900_10 glass-ceramics with MPs concentration 0.5wgt% are depicted in Figure 57.
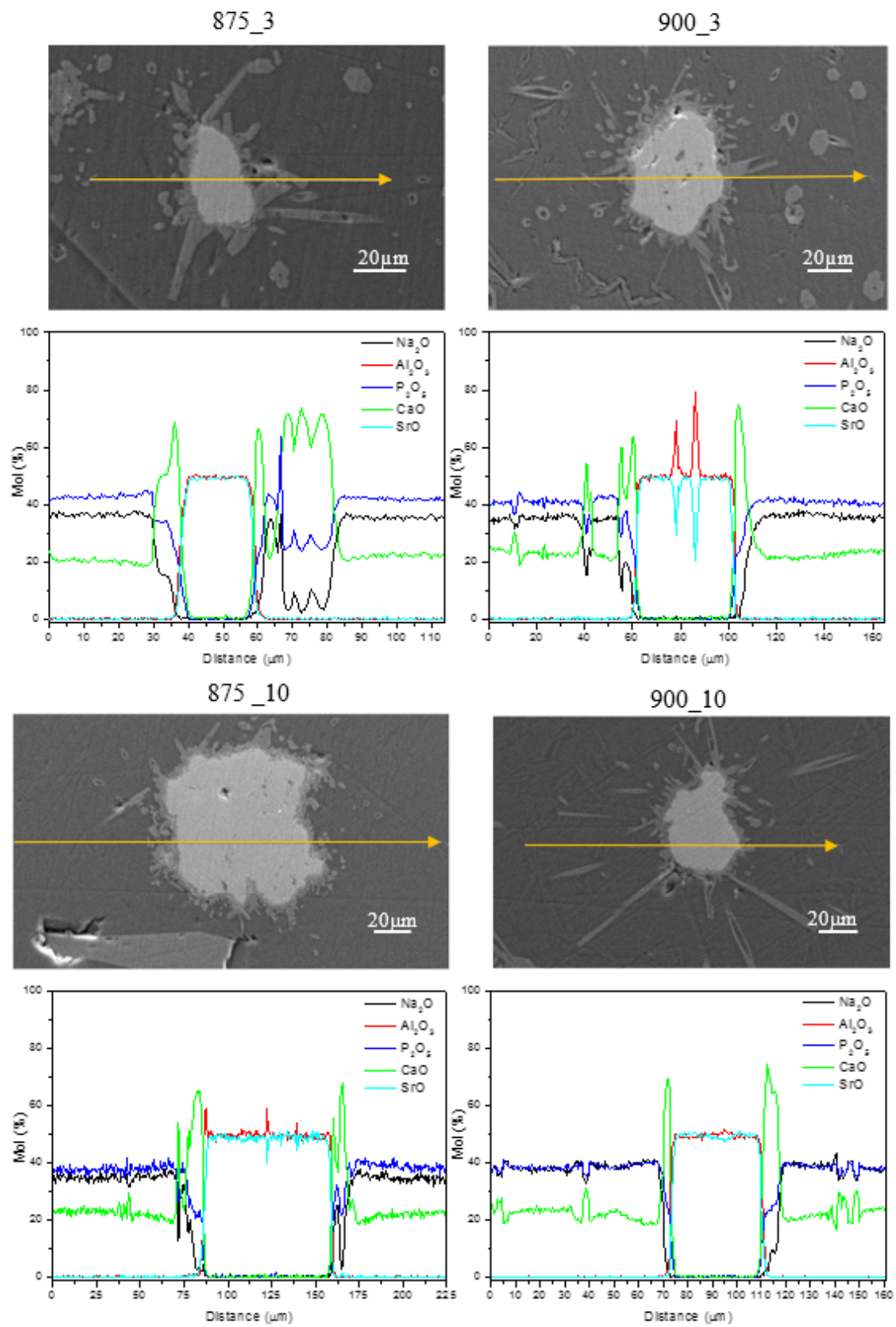
Figure 57.   SEM/Composition analysis of the glass at different T_{doping} and different doping time with MPs concentration of 0.5 wgt%

Particles with an average size of 20−80 μm can be seen in the SEM images. The compositions of the glass matrices are in accordance with the theoretical one within the accuracy of the measurements (±1.5mol%) considering that F content can not be quantified using this technique. According to (Oj,18a), the size and number of these crystals are suspected to decrease with the increase in the T_{doping} and the dwell time. However, no such relation can be observed here. The composition of all the MPs is $SrAl_2O_4$, indicating that all the MPs maintain their compositional integrity in their center independently of the doping parameters. Crystals can be seen around the MPs. Based on the EDS analysis, these crystals are Ca-rich crystals. Their composition seems to be ~$60CaO-30P_2O_5-10Na_2O$ (mol%). As seen in the Figure 58, other crystals can be seen in the glasses.
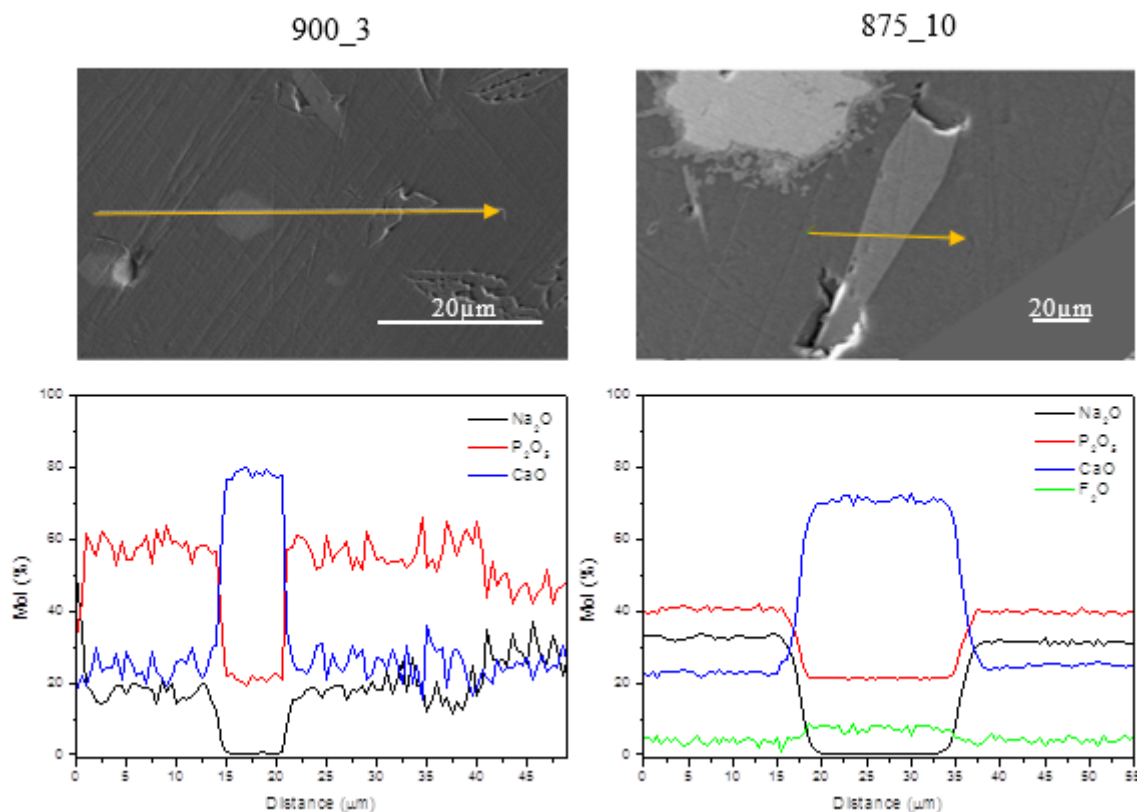

Figure 58. SEM/Composition analysis of the glass at different T_{doping} and different doping time with MPs concentration of 0.5 wgt%

Some of these crystals are suspected to contain F. To further analyze the composition of the crystals, XRD pattern of the glasses were measured. The spectra are presented in the Figure 59.
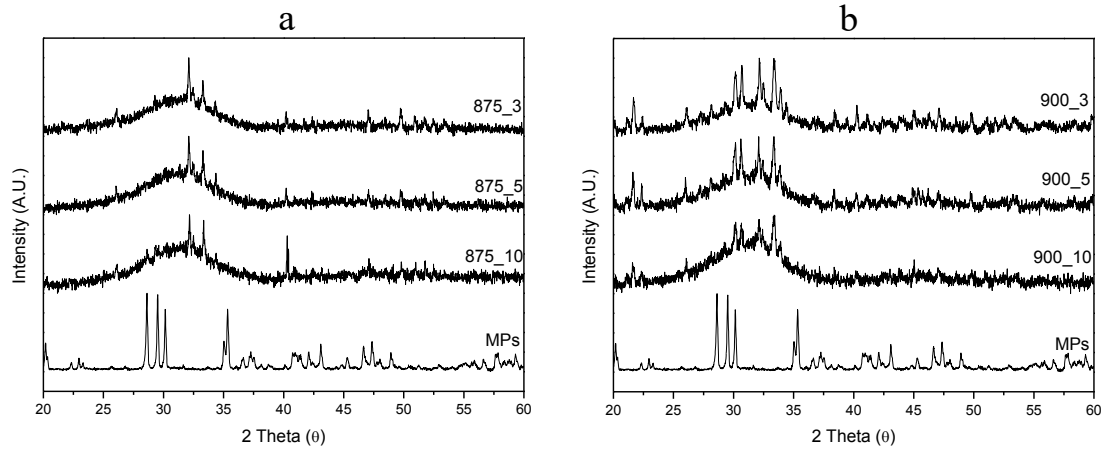
Figure 59.   XRD patterns of $T_{doping}=875°C$ glass a) and $T_{doping}=900°C$ glass b) with different dwell times

Crystallization peaks can be observed in the XRD pattern of the all as prepared glass-ceramic confirming presence of crystalline structure. Also shown is the XRD pattern of the MPs alone. It is clear that the peaks cannot be related to those of the MPs but to other crystals. The peaks could be attributed to a mixture of different phases presents the XRD diffraction pattern. However, it wasn't possible to identify crystals.

No relation between the intensity of the peaks and the doping parameters can be seen indicating that the crystals in the glass do not precipitate using the elements from the decomposition of the MPs.

Below in the Figure 60 are the XRD patterns of glass powder in which we added 1 and 2wg% of MPs in order to check the detection limit of MPs in amorphous glass using XRD.
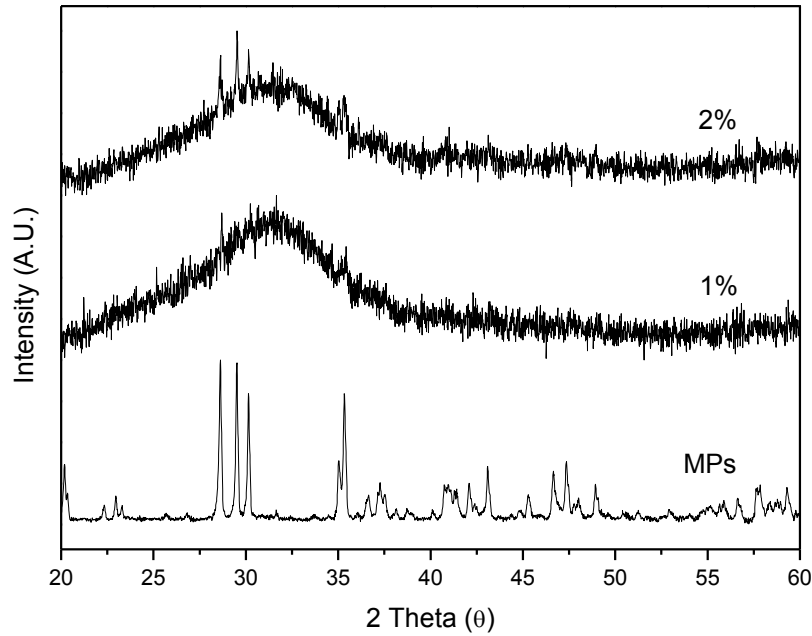
Figure 60.   XRD patterns of the glass with MPs concentration 1wgt% and 2wgt% to evaluate the detection limit

MPs can be seen in the XRD pattern if their concentration >1wgt% confirming that the peaks seen in the XRD patterns of the investigated glasses are from other crystal phases than the MPs.

In summary, in order to prepare a glass with homogeneous PeL, the T_{doping} should be 900°C. To limit the decomposition of the MPs, the dwell time should be 3min.

3.3.2   Optimization of the MPs amount in the PeL

New glasses were prepared with different amounts of MPs in order to check if it is possible to prepare clear PeL amorphous PeL glass within the investigated glass system. The doping parameters were 900°C for the T_{doping} and 3min for the dwell time. The pictures of the as prepared glasses in daylight and after stopping the UV irradiation are presented in the Figure 61.
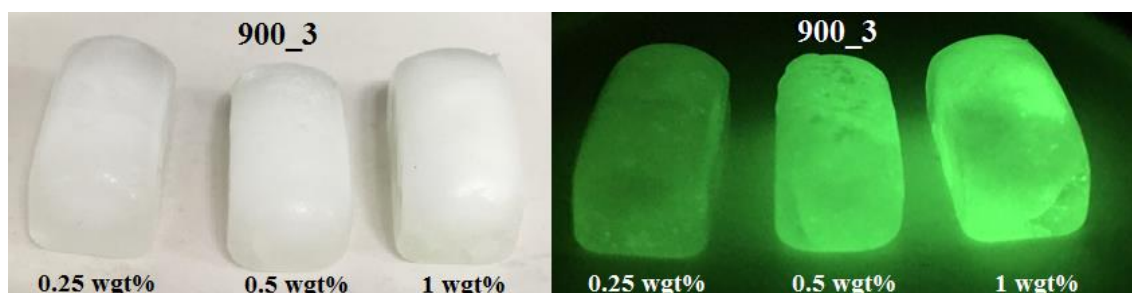
Figure 61.   *Picture of the glasses in day light and after stopping the UV irradiation (afterglow).The wgt% of the MPs was varied from 0.25 to 1 wgt%*

All glasses are crystallized independently of the MPs wgt%. After stopping the UV irradiation, all the glasses exhibit green persistent luminescence, the intensity of which depends on the MPs wgt%. Some afterglow could be seen from the glass which contains 0.25wgt% of MPs. The MPs are distributed homogenously confirming that the viscosity of glass melt at 900°C is high enough to disperse evenly the MPs in concentration at least up to 1%.

The persistent luminescence (PeL) spectra of the glasses are shown in Figure 62.
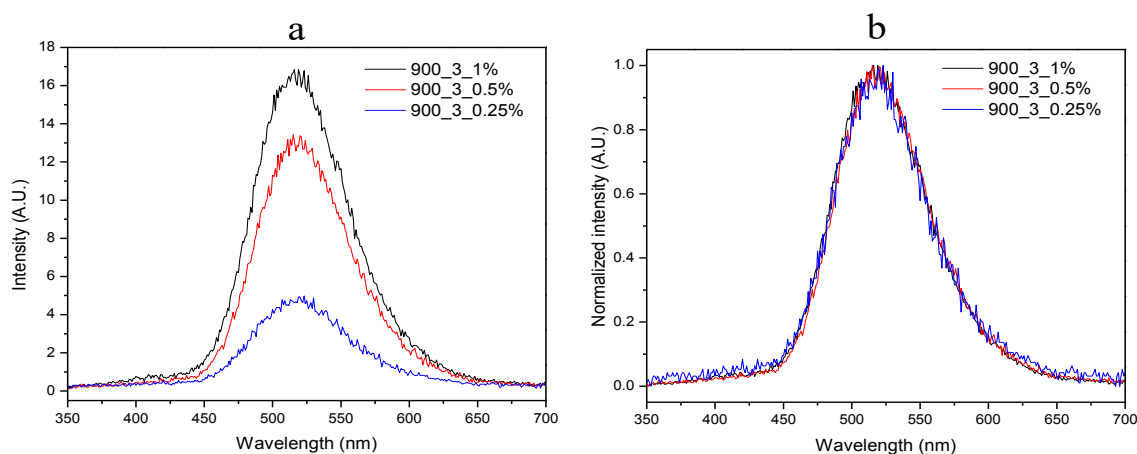
Figure 62.   Persistent Luminescence spectra a) and normalized Persistent Luminescence spectra of the glasses with different MPs concentration at T_{doping}=900°C and doping time 3min

As expected, an increase in the MPs concentration increases the intensity of the emission band at 520 nm. In agreement with the section 4.3.1, the shape of emission band remains the same after embedding the MPs in the glass.

The conventional luminescence (PeL) spectra of the glasses are shown in Figure 63.
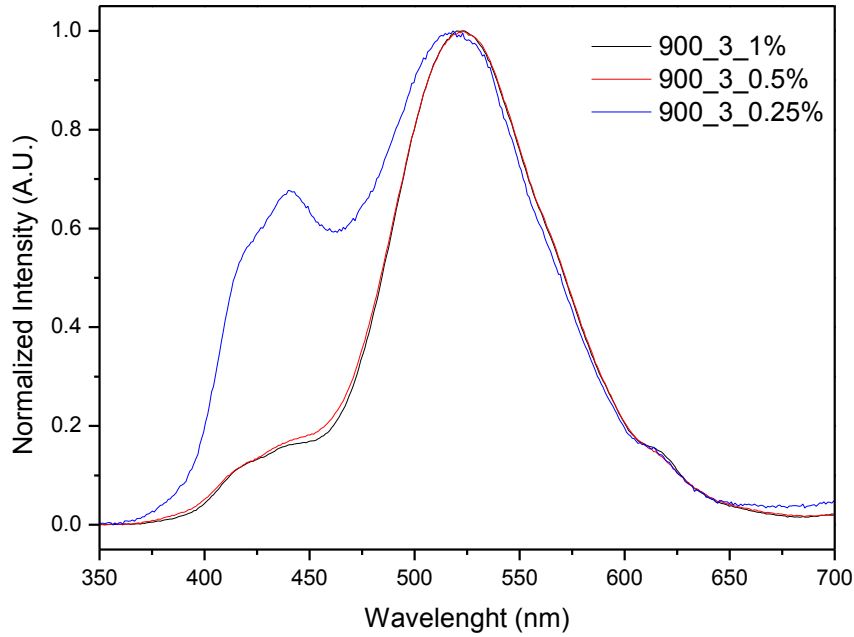
Figure 63.   Normalized conventional luminescence spectra of the glasses with different MPs concentration at
T_{doping}=900°C and doping time 3min

Surprisingly, the shape of the emission is different from the glass which contains 0.25wgt% of MPs. It is possible that 1) the 0.25wgt% glass was prepared using a slightly longer dwell time than 3min and/or 2) the emission of the MPs is not uniform.

The SEM images and EDS line profiles showing the elemental distribution across the MP diameter and interface with the glass-ceramics with different MPs concentrations are shown in the Figure 64.
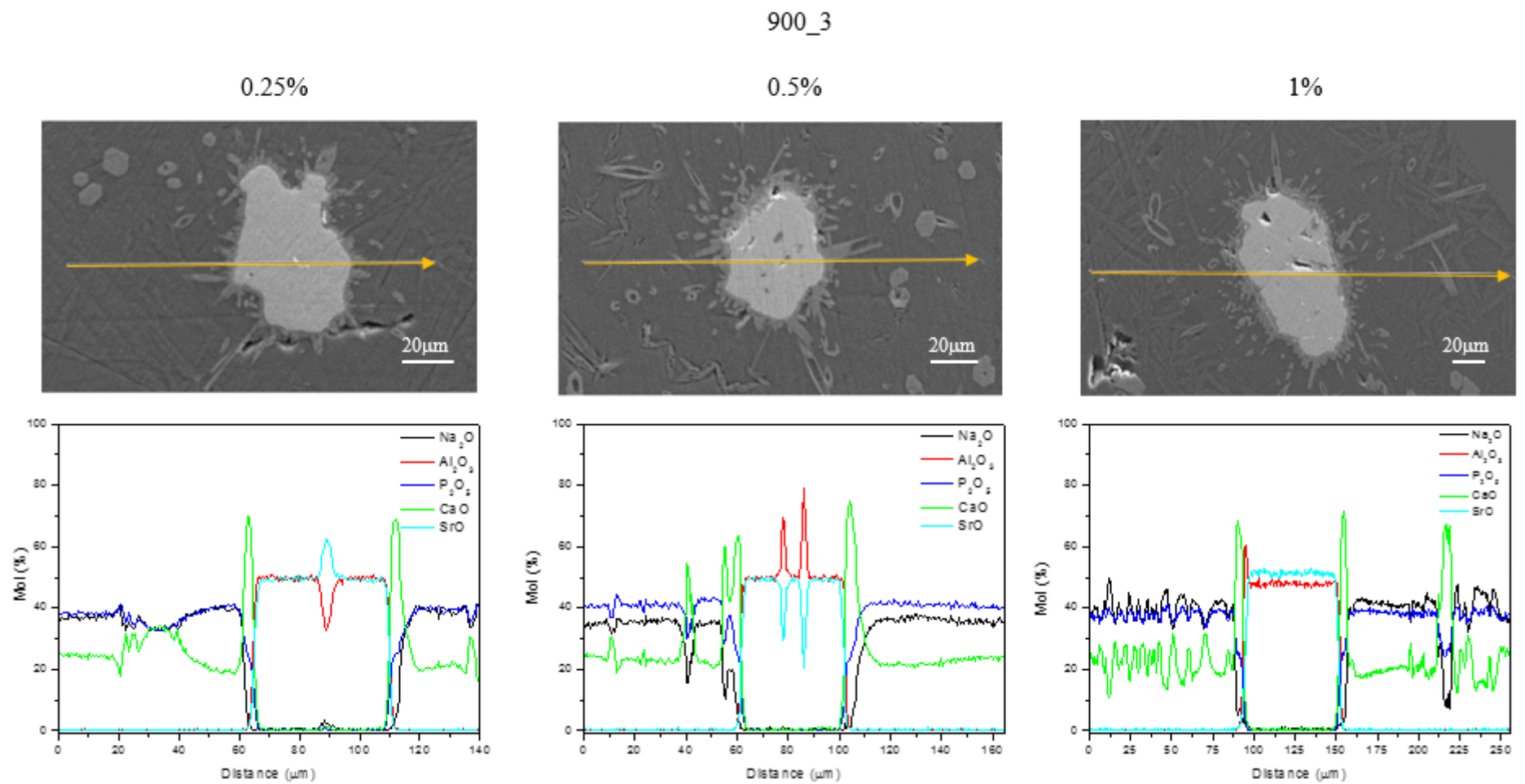
Figure 64.   *SEM/Composition analysis of the glasses at different MPs concentrations at $T_{doping}=900°C$ and doping time 3min*

Particles with an average size of 40-60 μm can be seen in the SEM images. The compositions of the glass matrices are in accordance with the theoretical one within the accuracy of the measurements (±1.5mol%). From the SEM images, there is no obvious relation between the size and number of crystals and the MPs concentrations. However, as seen in the XRD pattern of the glasses depicted in the Figure 65, no peaks can be seen in the 0.25wgt% glass indicating that the MPs act as a nucleating agents.
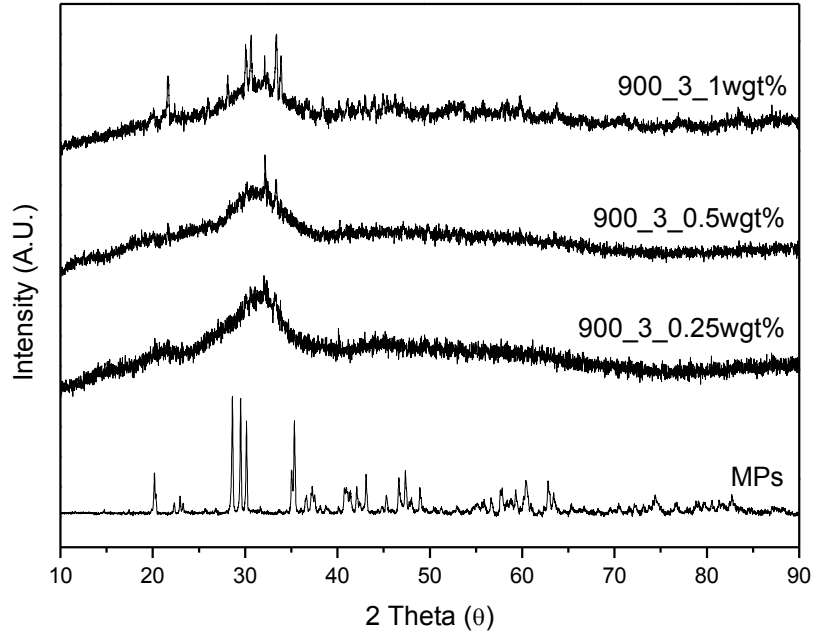
Figure 65.　　　XRD pattern of the glasses with different MPs concentration, at T_{doping}=900°C and doping time 3min

An increase in the MPs concentration increases the intensity of the peaks in the XRD patterns. Because crystals are clearly visible in the SEM image of the 0.25wgt%, these crystals are probably too small in size and/or too low in concentration to be detected in the XRD pattern of the glass.

3.3.3   Surface patterning

As mentioned in section 2.9, in order to check the feasibility of producing the micropattern consisted of 2D square gratings the more stable phosphate glasses with the composition 49.3P_2O_5-39.4 SrO-0.9Na_2O-1.5TiO_2 (in mol%) were used. Figure 66 shows a photograph of a micropatterned phosphate glass sample. The dimensions of the glass sample are 1.5cm x 1cm x 0.3cm. 2D surface relief gratings patterned on the glass surface are clearly observed with the naked eye.

Figure 66.   Photograph of a micropatterned phosphate glass sample. Micropatterns consist of surface relief 2D gratings. Each grating has an area of 4 mm x 4 mm, and grating periods are 6 µm and 12 µm.

Figure 67 shows surface profilometer measurements after different patterning steps. As presented in the Figure 67a the chromium thickness after deposition and lift off was around 140nm. In the Figure 67b it is shown that after ICP etching the depth of the pattern was around 348nm. The Figure 67c shows that the depth of final pattern after removing the Cr mask was around 265nm. Assuming no glass etching during chromium removal, the Cr layer was around 83nm thick after the ICP etching. This means an ICP etching selectivity (= glass etching rate / Cr etching rate) of ~4.2. This value supports the use of Cr as a mask. It should be noted that the ICP etching recipe is not optimized. Further experiments could be directed towards improving the etching selectivity by optimizing the ICP etching parameters, such as the CHF_3/Ar gas flow ratio. A higher etching selectivity would allow the production of higher aspect ratio microfeatures.
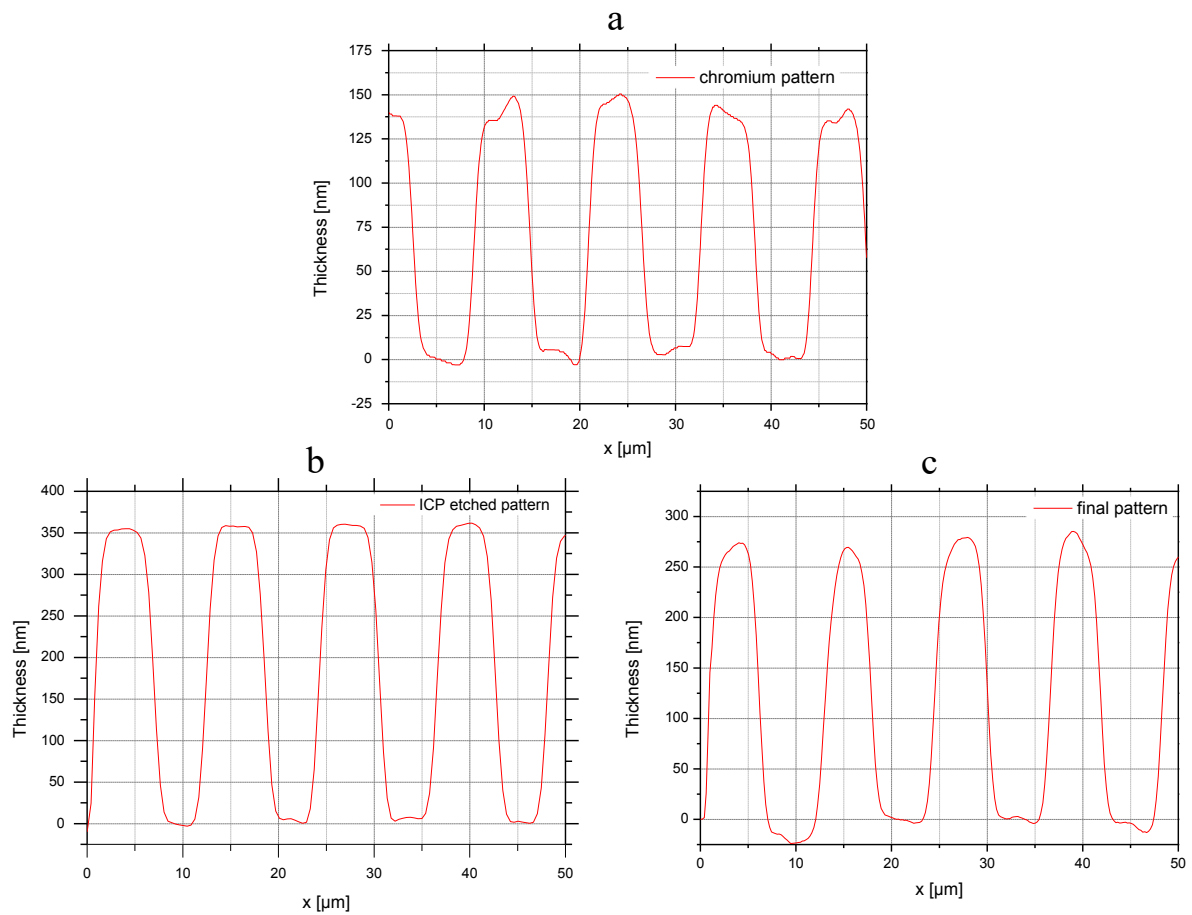
Figure 67. Profilometer profiles of pattern at the glass surface a) after thermal evaporation and deposition of chromium, b) after ICP etching, c) after chromium removal

Moroever, it can be seen in Figure 67 that the squares that made the pattern have side of around 6μm. This proves that presented surface structuring process is succesful at producing micron-sized patterns on the surface of the phosphate glass.

In the Figure 68 optical microscope photos taken during chromium removal are presented.

MAGNIFICATION

Figure 68. Optical microscope photos showing pattern at different stages of Cr removal The grating period equals 12 μm.
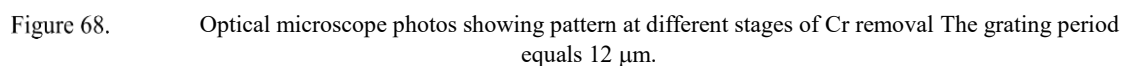
It can be seen that the pattern after 20s in chromium removal is not fully free of Cr residues. After 25s there are still some little chromium areas on the pattern surface. After 35s the chromium is succesfully removed from the pattern.

3.3.4 *Diffraction grating optical characterization*

The fabricated micropatterns on the phosphate glass samples were transparent 2D surface relief gratings. Thus they exhibited clear diffraction patterns in transmission when illuminated by a 635-nm-wavelength laser beam, as shown in Figure 69.

Grating period = 12 μm   Grating period = 6 μm
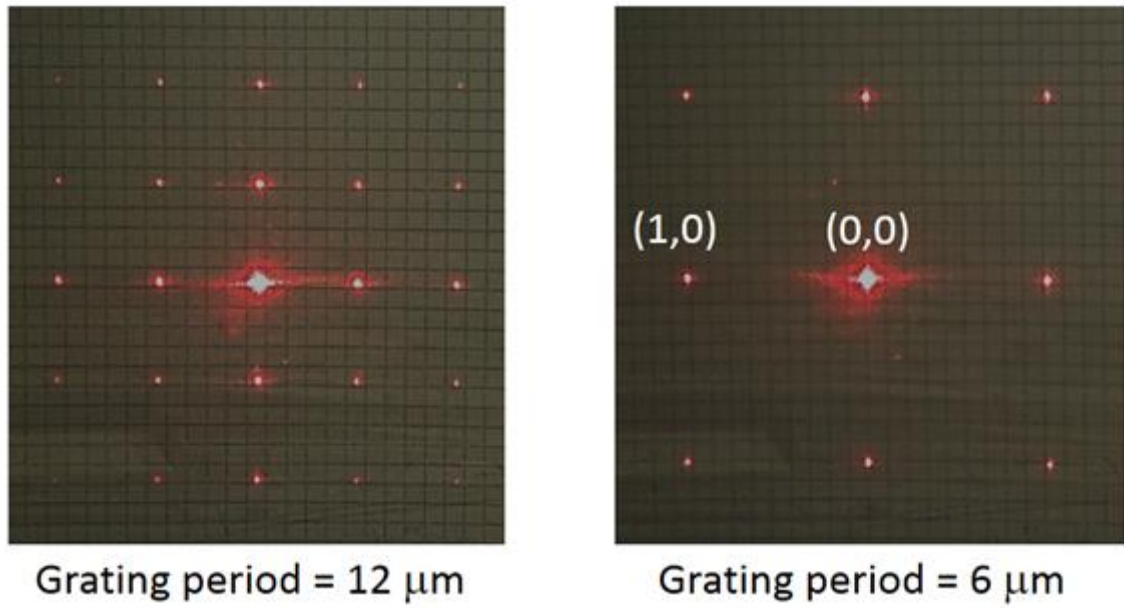
Figure 69.   Transmission diffraction patterns of the fabricated phosphate glass 2D square gratings. Left: grating period = 12 μm. Right: grating period = 6 μm. Both gratings were normally illuminated by a 635-nm-wavelength laser beam. Diffraction orders can be clearly observed; zero order (0,0) and first order (1,0) diffraction modes are indicated (Right).

The distribution of the incident optical power into the different diffraction orders depends on dimensional (thickness and lateral dimensions of the squares) and material optical parameters (refractive index contrast between the grating material and the surrounding medium) (Ga,85). Therefore, a potential degradation of the phosphate glass material when exposed to a given fluid could be monitored by measuring the diffraction efficiency (diffraction order power / total incident power) of one or several diffractions orders.

In particular, we decided to investigate the effect of deionized (DI) water on the phosphate glass material by inmersing a micropatterned glass sample in this liquid. Then, we measured the diffraction efficiencies of the zero-order (0,0) diffraction mode -defined as (zero-order mode power / total incident power)-, and the first-order (1,0) diffraction mode -defined as (first-order mode power / total incident power)-, over a period of 65 days.

Figures 70a and 70b show the diffraction efficiencies for the zero-order diffraction mode and the first-order diffraction mode, respectively, as a function of time. It is seen that both diffraction efficiencies decrease over time. However, whereas the (1,0) diffraction efficiency decreases at an approximately constant rate, that for the (0,0) mode exhibits a

remarkable abrupt decay during the first 5 days. As mentioned before, both diffraction efficiencies are dependent on the grating dimensional and material parameters. Thus, our measurements indicate that one or several of these grating paramenters change over time due to water exposure. It is well known that phosphate glass gets dissolved in aqueous media (Ga,04); therefore, the observed diffraction efficiency variations could be attributed to phosphate glass dissolution since this effect would modify the the geometry and dimensions of the grating.

In addition, glass dissolution in water may alter the refractive index of the liquid in which the grating is inmersed. Such an index variation could also affect the grating diffraction efficiencies. In order to determine the precise reasons for the measured decreasing trend in diffraction efficiency and the abrupt decay observed for the zeroth-order during the first days, further experiments and detailed theoretical and numerical analyses of the diffraction grating operation are required, which is beyond the purpose of this work.
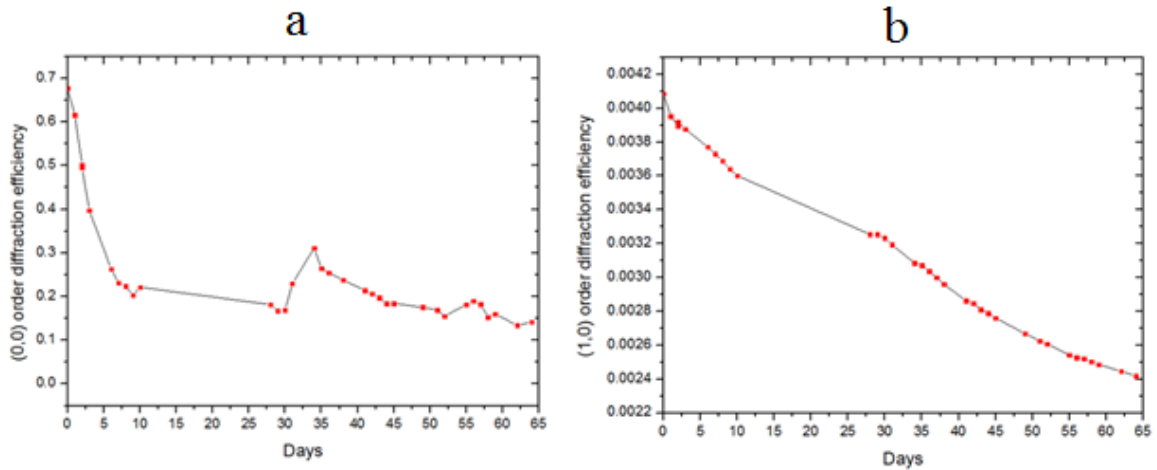

Figure 70.   Experimental diffraction efficiencies for (a) zero (0,0) and (b) first (1,0) diffracted orders of the fabricated 6-μm-period phosphate glass square grating over a 65 day time period.

4 Conclusions

New Er^{3+} doped oxyfluorophosphate glasses with the composition (75 $NaPO_3$-25 CaF_2)$_{100-x-0.25}$-(TiO_2/ZnO/MgO)$_x$, doped with 0.25mol% Er_2O_3, with x=0 and x=1.5 were prepared and characterized. An increase in the melting temperature leads to a decrease in the CaF_2 content. Based on absorption, emission, upconversion and lifetime measurements, an increase in the melting temperature has no noticeable impact on the sites of Er^{3+} ions. However, losses in F occurring during the glass melting process can lead to small changes in the thermal properties and also in the spectroscopic properties of the glasses.

The addition of 1.5mol%, of Ti, Zn and Mg to the glass composition leads to small changes in the physical, thermal, optical and spectroscopic properties of the glasses. The site of the Er^{3+} is suspected not to be strongly impacted by the changes in the glass composition. Zn and Mg seem to act as a modifier, leading to a depolymerization of the phosphate network and to a less cross-linked network. TiO_2 doping, leads to creation of 3D networks of P-O-Ti linkages causing distortion of the glass network.

Secondly, glass-ceramics were produced from the as-prepared glasses using controlled heat-treatment and characterized. The glasses become milky and bulk crystallization occurs during the heat treatment. An increase in T_m, which leads to losses in F content, increases the tendency of the glass to crystallization as only the glass melted at 1000°C becomes opaque after heat treatment. In this study, we show that it is possible to prepare transparent glass-ceramics from the investigated glasses.

The same bulk crystallization of CaF_2 occurs in ZnO, MgO and TiO_2 doped glasses upon heat treatment. The changes in the glass composition impact the tendency of the glass to crystallization, the Zn glass being the least prone to crystallization as compared to the Ti and Mg glasses. This difference can be related to Zn ions acting as modifiers which leads to depolymerization of the network. This in turn reduces the amount of nucleation sites and therefore decreases the crystallization tendency of the glass. The peaks related to the CaF_2 crystals start to be visible in the XRD patterns of all the glass-ceramics after 1h of heat treatment and are thought contain Er^{3+} ions. As the shape of the emission band remains similar after the heat treatment, it is possible to think that some Er^{3+} ions remain in the amorphous part of the glass-ceramic. Changes in glass composition and melting temperature could be used to control the crystallization tendency of glasses.

Subsequently, the PeL glass-ceramics were prepared by adding 0.25-1.0wgt% of luminescent microparticles (MPs) $SrAl_2O_4:Eu^{2+},Dy^{3+}$ in the melt of the glass with the composition (75 $NaPO_3$-25 CaF_2) (mol%). After stopping the UV irradiation, all the glasses exhibit green persistent luminescence, the intensity of which depends on the MPs wgt%, confirming the survival of the MPs. An increase in the PeL microparticles concentration leads to an increase in luminescence properties. No relation between the intensity of the peaks and the doping parameters (dwell time, doping temperature) can be seen indicating that the crystals in the glass do not precipitate using the elements from the decomposition of the MPs. Ca rich crystals can be seen around the MPs.The PeL glass-ceramic was fully crystallized with at least three different types of crystals. In the XRD diffraction pattern the peaks could be attributed to a mixture of different phases which were impossible to identify.

Finally, a recipe allowing patterning of 2D micron-sized gratings onto phosphate glass surface has been developed. The micropatterning procedure is based on conventional micro/nano fabrication proccesses, which should facilitate mass production. The fabricated surface relief glass gratings showed clear diffraction patterns. This has been taken advantage for monitoring possible phosphate glass degradation due to DI-water exposure by measuring the optical efficiencies of zero and first diffraction orders of a fabricated glass grating immersed in DI-water.

The Er^{3+} doped and the PeL glass-ceramic properties should be further investigated for utilization as biomaterial which could be tracked in vivo. Moreover, 2D grating could be used to investigate the stability and degradation rate of the produced glasses using diffraction measurements.

References

(Ac,10) Achatz, D.E., Ali, R. & Wolfbeis, O.S. (2010). Luminescent chemical sensing, biosensing, and screening using upconverting nanoparticles, in: Anonymous (ed.), Luminescence applied in sensor science, Springer, pp. 29-50.

(Ai,03) Aitasalo, T., Dereń, P., Hölsä, J., Jungner, H., Krupa, J., Lastusaari, M., Legendziewicz, J., Niittykoski, J. & Stręk, W. (2003). Persistent luminescence phenomena in materials doped with rare earth ions, Journal of Solid State Chemistry, Vol. 171(1-2), pp. 114-122.

(Ai,04) Aitasalo, T., Holsa, J., Jungner, H., Krupa, J., Lastusaari, M., Legendziewicz, J. & Niittykoski, J. (2004). Effect of temperature on the luminescence processes of SrAl2O4: Eu2, Radiation Measurements, Vol. 38(4-6), pp. 727-730.

(An,95) Anderson, D.L. (1995). Through the glass lightly, Science, Vol. 267(5204), pp. 1618.

(Ar,19) AR Coating Techniques: Thin Film Deposition Methods
https://www.findlight.net/blog/2017/12/15/ar-coating-techniques/ Retrieved 18.05.19

(Ba,06) Barrere, F., van Blitterswijk, C.A. & de Groot, K. (2006). Bone regeneration: molecular and cellular interactions with calcium phosphate ceramics, International journal of nanomedicine, Vol. 1(3), pp. 317.

(Ba,94) Barriere, A.S., Raoux, S., Garcia, A., L'haridon, H., Lambert, B. & Moutonnet, D. (1994). Intra-4 f-shell transitions at room temperature of Er3 ions in Ca1− x Er x F2 x thin films grown on Si (100), Journal of Applied Physics, Vol. 75(2), pp. 1133-1137.

(Be,14) Belostotsky, V. (2014). Multicomponent solution solidification with arrested phase separation model for liquid-to-glass transition.

(Be,69) Beall, G.H. & Duke, D.A. (1969). Transparent glass-ceramics, Journal of Materials Science, Vol. 4(4), pp. 340-352.

(Bi,04) Birnie, D. P. (2004). Spin coating technique. In Sol-Gel Technologies for Glass Producers and Users (pp. 49-55). Springer, Boston, MA.

(Br,11) Brito, H.F., Hassinen, J., Holsa, J., Jungner, H., Laamanen, T., Lastusaari, M., Malkamaki, M., Niittykoski, J., Novak, P. & Rodrigues, L.C. (2011). Optical energy storage properties of Sr2MgSi2O7: Eu2 , R3 persistent luminescence materials, Journal of thermal analysis and calorimetry, Vol. 105(2), pp. 657-662.

(Br,12a) Brauer, D.S., Anjum, M.N., Mneimne, M., Wilson, R.M., Doweidar, H. & Hill, R.G. (2012a). Fluoride-containing bioactive glass-ceramics, Journal of Non-Crystalline Solids, Vol. 358(12-13), pp. 1438-1442.

(Br,12b) Brauer, D.S., Anjum, M.N., Mneimne, M., Wilson, R.M., Doweidar, H. & Hill, R.G. (2012b). Fluoride-containing bioactive glass-ceramics, Journal of Non-Crystalline Solids, Vol. 358(12-13), pp. 1438-1442.

(Br,00) Brow, R.K. (2000). The structure of simple phosphate glasses, Journal of Non-Crystalline Solids, Vol. 263 pp. 1-28.

(Br,12) Brito, H.F., Holsa, J., Laamanen, T., Lastusaari, M., Malkamaki, M. & Rodrigues, L.C. (2012). Persistent luminescence mechanisms: human imagination at work, Optical Materials Express, Vol. 2(4), pp. 371-381.

(Bu,84) Bunker, B.C., Arnold, G.W. & Wilder, J.A. (1984). Phosphate glass dissolution in aqueous solutions, Journal of Non-Crystalline Solids, Vol. 64(3), pp. 291-316.

(Ca,00) Callister, W.D. (2000). Fundamentals of materials science and engineering, Wiley London.

(Ca,96) Cao, W. & Hench, L.L. (1996). Bioactive materials, Ceramics International, Vol. 22(6), pp. 493-507.

(Ch,90) Cheong, W., Prahl, S.A. & Welch, A.J. (1990). A review of the optical properties of biological tissues, IEEE Journal of Quantum Electronics, Vol. 26(12), pp. 2166-2185.

(Cl,99) Cle, J., Planell, J.A., Avila, G. & Marti, S. (1999). Analysis of the structural changes of a phosphate glass during its dissolution in simulated body fluid, Journal of Materials Science: Materials in Medicine, Vol. 10(12), pp. 729-732.

(Cr,61) Cruickshank, D. (1961). 1077. The role of 3 d-orbitals in p-bonds between (a) silicon, phosphorus, sulphur, or chlorine and (b) oxygen or nitrogen, Journal of the Chemical Society (Resumed), pp. 5486-5504.

(Cu,16) Cui, S., Massera, J., Lastusaari, M., Hupa, L. & Petit, L. (2016). Novel oxyfluorophosphate glasses and glass-ceramics, Journal of Non-Crystalline Solids, Vol. 445 pp. 40-44.

(De,07) de Chermont, Quentin le Masne, Chaneac, C., Seguin, J., Pelle, F., Maitrejean, S., Jolivet, J., Gourier, D., Bessodes, M. & Scherman, D. (2007). Nanoprobes with near-infrared persistent luminescence for in vivo imaging, Proceedings of the National Academy of Sciences, Vol. 104(22), pp. 9266-9271.

(De,98) Dejneka, M.J. (1998). Transparent oxyfluoride glass ceramics, MRS Bulletin, Vol. 23(11), pp. 57-62.

(Di,01) Digonnet, M.J. (2001). Rare-earth-doped fiber lasers and amplifiers, revised and expanded, CRC press,

(Di,18) Diffraction of x-rays by crystals, http://www.kshitij-iitjee.com/diffraction-of-x-rays-by-crystals/. Retrieved 06.06.18.

(Do,15) Dousti, M.R., Amjad, R.J., Sahar, M.R., Zabidi, Z.M., Alias, A.N. & de Camargo, A. (2015). Er3 -doped zinc tellurite glasses revisited: concentration dependent chemical durability, thermal stability and spectroscopic properties, Journal of Non-Crystalline Solids, Vol. 429 pp. 70-78.

(Eb,19) E-Beam & thermal evaporation http://www.kenosistec.com/en/product_card.php?id=8&categoria=1 Retrieved 18.05.19

(Fe,00) Featherstone, J.D. (2000). The science and practice of caries prevention, The Journal of the American Dental Association, Vol. 131(7), pp. 887-899.

(Fo,18) Fourier-transform infrared spectroscopy https://en.wikipedia.org/wiki/Fourier-transform_infrared_spectroscopy. Retrieved 06.06.18.

(Fr,03a) Frangioni, J.V. (2003). In vivo near-infrared fluorescence imaging, Current opinion in chemical biology, Vol. 7(5), pp. 626-634.

(Fr,03b) Freeman, C.O., Brook, I.M., Johnson, A., Hatton, P.V., Hill, R.G. & Stanton, K.T. (2003). Crystallization modifies osteoconductivity in an apatite–mullite glass–ceramic, Journal of Materials Science: Materials in Medicine, Vol. 14(11), pp. 985-990.

(Ga,04) Gao, H., Tan, T., & Wang, D. (2004). Dissolution mechanism and release kinetics of phosphate controlled release glasses in aqueous medium. Journal of controlled release, 96(1), 29-36.

(Ga,85) Gaylord, T. K., & Moharam, M. G. (1985). Analysis and applications of optical diffraction by gratings. Proceedings of the IEEE, 73(5), 894-937

(Gi,17) Gilabert-Chirivella, E., Pérez-Feito, R., Ribeiro, C., Ribeiro, S., Correia, D. M., González-Martín, M. L.,& Gómez-Ribelles, J. L. (2017). Chitosan patterning on titanium implants. Progress in organic coatings, 111, 23-28.

(Go,02) Goncalves, M.C., Santos, L.F. & Almeida, R.M. (2002). Rare-earth-doped transparent glass ceramics, Comptes Rendus Chimie, Vol. 5(12), pp. 845-854.

(Go,17) Goldstein, J.I., Newbury, D.E., Michael, J.R., Ritchie, N.W., Scott, J.H.J. & Joy, D.C. (2017). Scanning electron microscopy and X-ray microanalysis, Springer.

(Ha,10) Hahn, R., Berger, S. & Schmuki, P. (2010). Bright visible luminescence of self-organized ZrO 2 nanotubes, Journal of Solid State Electrochemistry, Vol. 14(2), pp. 285.

(Ha,16) Haus, J. W. (Ed.). (2016). Fundamentals and applications of nanophotonics. Woodhead Publishing.

(Ho,09) Holsa, J. (2009). Persistent luminescence beats the afterglow: 400 years of persistent luminescence, Electrochem.Soc.Interface, Vol. 18(4), pp. 42-45.

(Ho,12) Holand, W. & Beall, G.H. (2012). Glass ceramic technology, John Wiley & Sons,

(Hö,18) Hönl, S., Hahn, H., Baumgartner, Y., Czornomaz, L., & Seidler, P. (2018). Highly selective dry etching of GaP in the presence of AlxGa1−xP with a SiCl4/SF6 plasma. Journal of Physics D: Applied Physics, 51(18), 185203.

(Hr,13) Hraiech, S., Ferid, M., Guyot, Y. & Boulon, G. (2013). Structural and optical studies of Yb3 , Er3 and Er3 /Yb3 co-doped phosphate glasses, Journal of Rare Earths, Vol. 31(7), pp. 685-693.

(Il,01) Ilieva, D., Jivov, B., Bogachev, G., Petkov, C., Penkov, I. & Dimitriev, Y. (2001). Infrared and Raman spectra of Ga2O3–P2O5 glasses, Journal of Non-Crystalline Solids, Vol. 283(1-3), pp. 195-202.

(In,19a) Inductively Coupled Plasma Etching (ICP) https://plasma.oxinst.com/campaigns/technology/icp-etching Retrieved 18.05.19.

(In,19b) Inductively Coupled Plasma – Reactive Ion Etching (ICP-RIE) https://www.corial.com/en/technologies/icp-rie-inductively-coupled-plasma-reactive-ion-etching/ Retrieved 18.05.19

(In,19c) Inductively coupled plasma http://hiq.linde-gas.com/en/analytical_methods/inductively_coupled_plasma.html Retrieved 18.05.19

(Ka,12) Kalogeras, I.M. & Hagg Lobland, H.E. (2012). The nature of the glassy state: structure and glass transitions, Journal of Materials Education, Vol. 34(3), pp. 69.

(Ka,14) Karpukhina, N., Hill, R.G. & Law, R.V. (2014). Crystallisation in oxide glasses–a tutorial review, Chemical Society Reviews, Vol. 43(7), pp. 2174-2186.

(Ki,12) Kiani, A., Hanna, J.V., King, S.P., Rees, G.J., Smith, M.E., Roohpour, N., Salih, V. & Knowles, J.C. (2012). Structural characterization and physical properties of P2O5–CaO–Na2O–TiO2 glasses by Fourier transform infrared, Raman and solid-state magic angle spinning nuclear magnetic resonance spectroscopies, Acta biomaterialia, Vol. 8(1), pp. 333-340.

(Ko,10) Konidakis, I., Varsamis, C.E., Kamitsos, E.I., Möncke, D. & Ehrt, D. (2010). Structure and properties of mixed strontium− manganese metaphosphate glasses, The Journal of Physical Chemistry C, Vol. 114(19), pp. 9125-9138.

(Ku,01) Kukkonen, L.L., Reaney, I.M., Furniss, D., Pellatt, M.G. & Seddon, A.B. (2001). Nucleation and crystallisation of transparent, erbium III-doped, oxyfluoride glass-ceramics, Journal of Non-Crystalline Solids, Vol. 290(1), pp. 25-31.

(La,06) Lakowicz, J.R. (2006). Principles of Fluorescence Spectroscopy, Springer, Boston,

(Le,13) Le Parlouer, P. (2013). Thermal Analysis and Calorimetry Techniques for Catalytic Investigations, in: Anonymous (ed.), Calorimetry and Thermal Methods in Catalysis, Springer, pp. 51-101.

(Li,12) Li, C. W., & Wang, G. J. (2012). MEMS manufacturing techniques for tissue scaffolding devices. In Mems for Biomedical Applications (pp. 192-217). Woodhead Publishing.

(Li,13) Liu, Q., Feng, W., Yang, T., Yi, T. & Li, F. (2013). Upconversion luminescence imaging of cells and small animals, Nature protocols, Vol. 8(10), pp. 2033.

(Li,14) Liu, S.J., Fu, G.Z., Shan, Z.T., Ren, X.R., Zhang, Y.F., Zhu, C.F., He, W. & Yue, Y.Z. (2014). Nanocrystal formation and photoluminescence in the Yb3 /Er3 codoped phosphosilicate glasses, Journal of Non-Crystalline Solids, Vol. 383 pp. 141-145.

(Li,15) Li, T., Guo, C., Zhou, S., Duan, C. & Yin, M. (2015). Highly Sensitive Optical Thermometry of Yb3 -Er3 Codoped AgLa (MoO4) 2 Green Upconversion Phosphor, Journal of the American Ceramic Society, Vol. 98(9), pp. 2812-2816.

(Lo,17) Lopez-Iscoa, P., Petit, L., Massera, J., Janner, D., Boetti, N.G., Pugliese, D., Fiorilli, S., Novara, C., Giorgis, F. & Milanese, D. (2017). Effect of the addition of Al2O3, TiO2 and ZnO on the thermal, structural and luminescence properties of Er3 -doped phosphate glasses, Journal of Non-Crystalline Solids, Vol. 460 pp. 161-168.

(Ma,11) Makhlouf, A. S. H., & Tiginyanu, I. (Eds.). (2011). Nanocoatings and ultra-thin films: Technologies and applications. Elsevier.

(Ma,14) Maldiney, T., Bessiere, A., Seguin, J., Teston, E., Sharma, S.K., Viana, B., Bos, A.J., Dorenbos, P., Bessodes, M. & Gourier, D. (2014). The in vivo activation of persistent nanophosphors for optical imaging of vascularization, tumours and grafted cells, Nature materials, Vol. 13(4), pp. 418.

(Ma,16) Massera, J., Gaussiran, M., Głuchowski, P., Lastusaari, M., Petit, L., Hölsä, J. & Hupa, L. (2016). Effect of the glass melting condition on the processing of phosphate-based glass–ceramics with persistent luminescence properties, Optical Materials, Vol. 52 pp. 56-61.

(Ma,96) Matsuzawa, T., Aoki, Y., Takeuchi, N. & Murayama, Y. (1996). A New Long Phosphorescent Phosphor with High Brightness, SrAl2 O 4: Eu2 , Dy3, Journal of the Electrochemical Society, Vol. 143(8), pp. 2670-2673.

(Me,97) Meyer, K. (1997). Characterization of the structure of binary zinc ultraphosphate glasses by infrared and Raman spectroscopy, Journal of Non-Crystalline Solids, Vol. 209(3), pp. 227-239.

(Mi,91) Miniscalco, W.J. (1991). Erbium-doped glasses for fiber amplifiers at 1500 nm, Journal of Lightwave Technology, Vol. 9(2), pp. 234-250.

(Mo,12) Mohd Zaid, M.H., Matori, K.A., Abdul Aziz, S.H., Zakaria, A. & Mohd Ghazali, M.S. (2012). Effect of ZnO on the physical properties and optical band gap of soda lime silicate glass, International journal of molecular sciences, Vol. 13(6), pp. 7550-7558.

(Mu,13) Mura, E., Lousteau, J., Milanese, D., Abrate, S. & Sglavo, V.M. (2013). Phosphate glasses for optical fibers: Synthesis, characterization and mechanical properties, Journal of Non-Crystalline Solids, Vol. 362 pp. 147-151.

(Mu,63) Murthy, M.K. (1963). Phosphate-Halide Systems: II, Infrared Spectra of Glasses in the System NaPO3-NaF, Journal of the American Ceramic Society, Vol. 46(11), pp. 558-559.

(Na,19) Nasrollahzadeh M., Sajadi S. M., Sajjadi M., Issaabadi Z., Atarod M. (2019). An Introduction to Green Nanotechnology. Interface Science and Technology.

(Ne,08) Neel, E.A. & Knowles, J.C. (2008). Physical and biocompatibility studies of novel titanium dioxide doped phosphate-based glasses for bone tissue engineering applications, Journal of Materials Science: Materials in Medicine, Vol. 19(1), pp. 377-386.

(Ng,11) Nguyen, N. T. (2011). Micromixers: fundamentals, design and fabrication. William Andrew.

(No,18) Nommeots-Nomm, A., Boetti, N.G., Salminen, T., Massera, J., Hokka, M. & Petit, L. (2018). Luminescence of Er 3 doped oxyfluoride phosphate glasses and glass-ceramics, Journal of Alloys and Compounds,

(Ob,98) Obaton, A., Bernard, J., Parent, C., Le Flem, G., Labbé, C., Le Boulanger, P. & Boulon, G. (1998). Spectroscopic investigations of Yb 3 –Er 3 –codoped LaLiP 4 O 12 glasses relevant for laser applications, The European Physical Journal-Applied Physics, Vol. 4(3), pp. 315-321.

(Oj,18a) Ojha, N., Laihinen, T., Salminen, T., Lastusaari, M. & Petit, L. (2018). Influence of the phosphate glass melt on the corrosion of functional particles occurring during the preparation of glass-ceramics, Ceramics International, Vol. 44(10), pp. 11807-11811.

(Oj,18b) Ojha, N., Nguyen, H., Laihinen, T., Salminen, T., Lastusaari, M. & Petit, L. (2018). Decomposition of persistent luminescent microparticles in corrosive phosphate glass melt, Corrosion Science, Vol. 135 pp. 207-214.

(Oj,18c) Ojha, N., Tuomisto, M., Lastusaari, M. & Petit, L. (2018). Phosphate glasses with blue persistent luminescence prepared using the direct doping method, Optical Materials.

(Op,19) Optical Profilometry https://www.nanoscience.com/techniques/optical-profilometry/#how Retrieved 18.05.19.

(Ov,18) Overview of Spectroscopy https://www.gamry.com/Framework%20Help/HTML5%20-%20Tripane%20-%20Audience%20A/Content/SE/Introduction/Overview%20of%20Spectroscopy.htm. Retrieved 06.06.18.

(Pa,07) Pan, Z., Ueda, A., Mu, R. & Morgan, S.H. (2007). Upconversion luminescence in Er3 -doped germanate-oxyfluoride and tellurium-germanate-oxyfluoride transparent glass-ceramics, Journal of Luminescence, Vol. 126(1), pp. 251-256.

(Pa,18) Parts of the machine
http://www.ammrf.org.au/myscope/xrd/background/whatisxrd/. Retrieved 06.06.18.

(Pe,12) Pekkan, G., Aktas, A. & Pekkan, K. (2012). Comparative radiopacity of bone graft materials, Journal of Cranio-Maxillo-Facial Surgery, Vol. 40(1), pp. e4. Available (accessed pmid:21353579):

(Ph,19) Photoresist https://en.wikipedia.org/wiki/Photoresist Retrieved 18.05.19.

(Po,06) Pospíšil, J., Mošner, P. & Koudelka, L. (2006). Thermal behaviour and crystallization of titanium–zinc borophosphate glasses, Journal of thermal analysis and calorimetry, Vol. 84(2), pp. 479-482.

(Pr,08) Praveena, R., Venkatramu, V., Babu, P., Jayasankar, C.K., Tröster, T., Sievers, W. & Wortmann, G. (2008). Luminescence properties of Sm3 -doped P2O5–PbO–Nb2O5 glass under high pressure, Journal of Physics: Condensed Matter, Vol. 21(3), pp. 035108.

(Pu,17) Puthankovilakam, K. (2017). Limitations of Proximity Lithography Printing (No. THESIS). EPFL

(Ra,18) Rare-earth-doped Gain Media https://www.rp-photonics.com/rare_earth_doped_gain_media.html. Retrieved 06.06.18.

(Sa,00) Salih, V., Franks, K., James, M., Hastings, G.W., Knowles, J.C. & Olsen, I. (2000). Development of soluble glasses for biomedical use Part II: The biological response of human osteoblast cell lines to phosphate-based soluble glasses, Journal of Materials Science: Materials in Medicine, Vol. 11(10), pp. 615-620.

(Sa,18) Saarinen, M., Nommeots-Nomm, A., Hokka, M., Laurila, J., Norrbo, I., Lastusaari, M., Massera, J. & Petit, L. (2018). Persistent luminescent particles containing bioactive glasses: Prospect toward tracking in-vivo implant mineralization using biophotonic ceramics, Journal of the European Ceramic Society, Vol. 38(1), pp. 287-295.

(Sc,18) Scodary, A. Shattering a Wine Glass with Sound
http://large.stanford.edu/courses/2007/ph210/scodary2/. Retrieved 06.06.18.

(Se,10) Segawa, H., Akagi, N., Yano, T. & Shibata, S. (2010). Properties and structures of TiO2–ZnO–P2O5 glasses, Journal of the Ceramic Society of Japan, Vol. 118(1376), pp. 278-282.

(Sh,05) Shelby, J.E. (2005). Introduction to glass science and technology, Royal Society of Chemistry,

(Sh,16) Shaharuddin, S., Ahmed, I., Furniss, D., Parsons, A.J. & Rudd, C.D. (2016). Investigation on the thermal properties, density and degradation of quaternary iron and titanium phosphate based glasses, IOP Publishing, pp. 012124.

(Sm,13) Smith, R., Inomata, H., & Peters, C. (2013). Introduction to supercritical fluids: a spreadsheet-based approach (Vol. 4). Newnes.

(So,18) Soda-lime glass https://www.britannica.com/technology/soda-lime-glass. Retrieved 06.06.18.

(St,59) Stookey, S.D. (1959). Catalyzed crystallization of glass in theory and practice, Industrial & Engineering Chemistry, Vol. 51(7), pp. 805-808.

(Th,08) Thuy, T.T., Nakagaki, H., Kato, K., Hung, P.A., Inukai, J., Tsuboi, S., Nakagaki, H., Hirose, M.N., Igarashi, S. & Robinson, C. (2008). Effect of strontium in combination with fluoride on enamel remineralisation in vitro, Archives of Oral Biology, Vol. 53(11), pp. 1017-1022.

(Th,19) Thermal evaporation in vacuumhttps://www.icmm.csic.es/fis/english/evaporacion_resistencia.html Retrieved 18.05.19

(Ve,00) Veasey, D.L., Funk, D.S., Peters, P.M., Sanford, N.A., Obarski, G.E., Fontaine, N., Young, M., Peskin, A.P., Liu, W. & Houde-Walter, S.N. (2000). Yb/Er-codoped and Yb-doped waveguide lasers in phosphate glass, Journal of Non-Crystalline Solids, Vol. 263 pp. 369-381.

(Wa,03) Wang, J., Song, H., Kong, X., Peng, H., Sun, B., Chen, B., Zhang, J., Xu, W. & Xia, H. (2003). Fluorescence properties of trivalent europium doped in various niobate codoped glasses, Journal of Applied Physics, Vol. 93(3), pp. 1482-1486.

(Wa,93) Wang, Y. & Ohwaki, J. (1993). New transparent vitroceramics codoped with Er3 and Yb3 for efficient frequency upconversion, Applied Physics Letters, Vol. 63(24), pp. 3268-3270.

(Wi,84) Wilder, J.A. & Shelby, J.E. (1984). Property Variation in Alkali Alkaline-Earth Metaphosphate Glasses, Journal of the American Ceramic Society, Vol. 67(6), pp. 438-444.

(Xr,18) X-Radiation https://www.nde-ed.org/EducationResources/CommunityCollege/Radiography/Physics/xrays.htm. Retrieved 06.06.18.

(Ya,97) Yamamoto, H. & Matsuzawa, T. (1997). Mechanism of long phosphorescence of SrAl2O4: Eu2 , Dy3 and CaAl2O4: Eu2 , Nd3, Journal of Luminescence, Vol. 72 pp. 287-289.

(Zh,16) Zhao, J., Zheng, X., Schartner, E.P., Ionescu, P., Zhang, R., Nguyen, T., Jin, D. & Ebendorff-Heidepriem, H. (2016). Upconversion Nanocrystal-Doped Glass: A New Paradigm for Photonic Materials, Advanced Optical Materials, Vol. 4(10), pp. 1507-1517.

(Zh,18) Zhang, J. X., & Hoshino, K. (2018). Molecular Sensors and Nanodevices: Principles, Designs and Applications in Biomedical Engineering. Academic Press.

(Zh,00) Zhao, Y., Wang, G. C., & Lu, T. M. (2000). Characterization of Amorphous and Crystalline Rough Surface--Principles and Applications (Vol. 37). Elsevier.

(Zi,69) Zikmund, M. & Štepničková, Ľ (1969). Spectral study of chloro (tetrahydrofuran) titanium (III) complexes, Chemical Papers, Vol. 23(11-12), pp. 850-855.